University of Oxford

D.Phil. Thesis

Formation and Collapse of Non-Wetting Cavities in Soft Porous Media

Oliver W. Paulin

Supervisor: Prof. C. W. MacMinn

A thesis submitted for the degree of Doctor of Philosophy

Department of Engineering Science

Wolfson College

Trinity Term 2023

Declaration of Authorship

I, Oliver W. Paulin, declare that this project, titled 'Formation and Collapse of Non-Wetting Cavities in Soft Porous Media' and the work presented in it are my own. I hereby certify that the work presented in this project is all my own unaided work and that all material obtained from published or unpublished sources of any type, including the internet, have been fully acknowledged at the proper point in the text and included in the list of references.

Signed: *Oliver Paulin*

Date: 05/10/2023

Abstract

Various biological and chemical processes lead to the nucleation and growth of non-wetting fluid 'bubbles' within the pore space of a soft porous medium. The non-wetting nature of these bubbles makes it energetically costly for them to invade the narrow pore throats between solid. If the solid skeleton is sufficiently soft and/or the confining stress is sufficiently low, non-wetting bubbles can instead displace the solid to form macroscopic cavities that are much larger than the pore size. An increase in the confining stress can suppress the formation of cavities and even drive the collapse of existing cavities, forcing the non-wetting fluid into the pore space. A quantitative understanding of the total volume of non-wetting cavities, their size distribution, and their formation and collapse are important for the macroscopic mechanics of this three-phase system and its interactions with the surrounding environment. Here, we consider this process through the lens of phase separation, where thermomechanics govern the separation of the non-wetting phase from a fluid–fluid–solid mixture. We construct a novel phase-field model informed by large-deformation poromechanics, in which two immiscible fluids interact with a poroelastic solid skeleton. To develop physical insight, we focus on two test problems: (1) the spontaneous formation of multiple cavities from an initial distribution of non-wetting fluid in the pore space and (2) the deformation-driven collapse of cavities due to compression via a fluid-permeable piston. We study these problems in 1D using numerical simulation, linear stability analysis, and analytical solutions of a reduced model. We identify the key parameters that control cavity formation and the characteristic size of resulting cavities. We also investigate the confining stress required to trigger cavity collapse, and explore the reversibility of cavity formation and collapse under fluctuating confining stress. We complement our theory with a series of simple experiments, using a packing of hydrogel beads as an example soft porous medium.

Acknowledgements

I am extremely grateful to Chris MacMinn for all of his support, supervision and assistance throughout this project. I have thoroughly enjoyed my time as a D. Phil. student, thanks in no small part to Chris' optimistic outlook and inspiring enthusiasm for science. I owe significant gratitude to Matt Hennessy and Liam Morrow for all of the time that they have invested in my project, and for the valuable advice that they have provided throughout. Thanks must also go to Matilde Fiori, Callum Cuttle, and the rest of the Poromechanics Lab for many interesting discussions over the past four years, as well as the camaraderie and friendship that they have provided. Additionally, I thank the European Research Council for providing the funding that supported this project.

Thank you to all of my friends in OUCCC, OUOC, and the wider Oxford running community for the many distractions that they have provided during my time in Oxford, and for the countless memories without which the past eight years would have been significantly poorer. I am incredibly grateful to my family for all of the support that they have provided me with over many years, both before and during my time as a student, without which I would not have been able to pursue these studies.

Finally, thank you to Tilly — for everything.

Contents

List of Figures

List of Symbols

A list of symbols used in this thesis, grouped by the chapter in which they first appear.

Subscripts

$\alpha,\ \beta$	Letter subscripts
$i,\ j$	Numeric subscripts
f	Fluid
g	Gas
l	Liquid
nw	Non-wetting fluid
s	Solid
w	Wetting fluid

Chapter 1

$\gamma_{\alpha\beta}$	Interfacial coefficient for phases α and β
ϖ	Cahn–Hilliard bulk energy
ϑ_c	Contact angle
$\mathcal{F}$	Total Cahn–Hilliard free energy

$\mathcal{K}$ Cahn–Hilliard interfacial parameter

$\mathcal{P}$ External variable in Cahn–Hilliard free energy

c Component concentration

p_α Pressure of phase α

p_c Capillary pressure

p_c^e Capillary entry pressure

r_p Characteristic radius of pore throat

Chapter 2

$\dot{\square}$ Partial derivative with respect to time

$\frac{\delta}{\delta\varphi_\alpha}$ Variational derivative with respect to φ_α

∇ Spatial gradient with respect to Eulerian coordinates

∇_0 Spatial gradient with respect to Lagrangian coordinates

$\boldsymbol{\sigma}'$ Effective (elastic) stress

$\boldsymbol{\xi}_\alpha$ Vector microstress associated with phase α

$\mathbf{A}$ General vector field

$\mathbf{q}$ Total mixture flux

$\mathbf{U}_s$ Lagrangian solid displacement

$\mathbf{u}_s$ Eulerian solid displacement

$\mathbf{v}_\alpha$ Local velocity of phase α

$\mathbf{W}_\alpha$ Lagrangian volume flux relative to solid skeleton

$\mathbf{w}_\alpha$ Eulerian volume flux relative to solid skeleton

$\mathbf{X}$	Lagrangian coordinate
$\mathbf{x}$	Eulerian coodinate
$\hat{\mathbf{e}}_i$	Cartesian unit vector
$\hat{\mathbf{n}}$	Unit normal vector
$\mathbb{B}$	General tensor field
$\mathbb{F}$	Deformation gradient tensor
$\mathbb{I}$	Identity tensor
$\mathbb{K}$	Korteweg stress tensor
$\mathbb{M}_\alpha$	Mobility tensor for phase α
$\mathbb{P}$	First Piola-Kirchoff stress tensor
$\mathbb{T}$	Cauchy stress tensor
$\chi_{\alpha\beta}$	Rescaled strength of interaction between phases α and β
χ_{gsl}	Characteristic strength of ternary interactions
δ	Position of left edge of porous medium
η_α	Dynamic viscosity of fluid α
Γ_i	Rescaled interfacial coefficients
κ_c	Strength of cohesion between solid grains
Λ	Lamé's first parameter
μ_α	Chemical potential of phase α
μ_α^0	Reference chemical potential of phase α
Ω_α	Inverse volume of particle α

ϕ True porosity (current configuration)

ϕ_0 Relaxed porosity (current configuration)

ϕ_s^0 Undeformed solid fraction

ϕ_α True volume fraction of phase α (current configuration)

Π_α Interaction potential of phase α

ψ Helmholtz free energy per unit reference volume

Ψ_α Capillary potential of phase α

ψ_{bulk} Bulk free energy density per unit reference volume

ψ_{damage} Damage free energy density per unit reference volume

ψ_{elastic} Elastic free energy density per unit reference volume

ψ_{FH} Flory–Huggins free energy density per unit reference volume

$\psi_{\text{interface}}$ Interfacial free energy density per unit reference volume

ψ_{mix} Mixing (interaction) free energy density per unit reference volume

ρ_α Density of phase α

σ_0' Undamaged neo-Hookean stress

σ_{xx}' xx-component of elastic stress

Θ Numerical smoothing parameter

Υ_{int} General interfacial energy density per unit reference volume

φ_α Nominal volume fraction of phase α (reference configuration)

ς Ratio of Lamé's first parameter to bulk modulus

$\hat{\chi}_{\alpha\beta}$ Strength of interaction between phases α and β

$\mathcal{D}$	Characteristic deformability
$\mathcal{E}_{\text{mix}}$	Characteristic mixing energy density
$\mathcal{G}_c$	Critical fracture energy density
$\mathcal{L}_d$	Rescaled width of damage transition
$\mathcal{M}_r$	Ratio of gas to liquid mobilities
$\mathcal{M}_\alpha$	Scalar mobility of phase α
$\mathcal{M}_\alpha^0$	Characteristic mobility of phase α
$\mathcal{T}_{\text{cap}}$	Capillary timescale
$\mathcal{V}_0$	Volume of material element
$\mathcal{W}^+$	Tensile strain-energy density
$\mathcal{W}^-$	Compressive strain-energy density
$\mathcal{W}_{\text{el}}$	Neo-Hookean strain-energy density
$\mathcal{W}_{\text{el}}^0$	Undamaged neo-Hookean strain-energy density
$\partial\mathcal{V}_0$	Boundary of material element
d	Damage parameter
$f(x)$	Analytical solution to sharp-interface poroelasticity
G	Shear modulus
$g(d)$	Degradation function
J	Jacobian determinant
k_B	Boltzmann constant
K_{xx}	xx-component of Korteweg stress

L Characteristic length scale

l_d Width of damage transition

p Thermodynamic mixture pressure

P_0 Absolute permeability

$P_{\alpha r}$ Relative permeability of phase α

q x-component of mixture flux

Q_0 Characteristic background flow

q_0 Boundary mixture flux

S_α True saturation of phase α (current configuration)

T Temperature

t Time

u_s x-component of solid displacement

v_α x-component of local velocity of phase α

w_α x-component of the flux of phase α relative to solid

$\tilde{P}_0$ Characteristic absolute permeability

$\tilde{P}_{\alpha r}$ Characteristic relative permeability of phase α

$\tilde{q}$ Dimensionless mixture flux

$\tilde{t}$ Dimensionless time

$\tilde{x}$ Dimensionless coordinate

$\bar{\mathrm{e}}_{\mathrm{rms}}$ Root-mean-square error

Chapter 3

Δ_g Size of gas cavity

ϵ Small parameter

ν Field of random fluctuations

ϕ_0' Precompressed base porosity

ϕ^* Strength of precompression

ϕ_α^b Volume fraction of phase α in bubble region (reduced model)

ϕ_α^w Volume fraction of phase α in wet region (reduced model)

ζ_i Dispersion relation coefficients

$\hat{\phi}_\alpha$ Leading order contributions of ϕ_α to linear stability analysis

$\overline{\phi}_\alpha$ Average volume fraction of phase α (reduced model)

$\mathcal{H}_{\alpha\beta}$ Homogeneous contributions to linear stability analysis

$\mathcal{H}_\alpha$ Homogeneous part of chemical potential of phase α

$\mathcal{N}_{\alpha\beta}$ Interfacial contributions to linear stability analysis

$\mathcal{R}$ Size of phase-separated bubble (reduced model)

$\mathcal{R}_{\text{eq}}$ Equilibrium size of phase-separated bubble (reduced model)

$\mathfrak{F}_E$ Elastic energy (reduced model)

$\mathfrak{F}_M$ Mixing energy (reduced model)

$\mathfrak{F}_T$ Total free energy (reduced model)

a_i Coefficients in ζ_1

b_i Coefficients in ζ_2

J_w Value of J in wet region (reduced model)

k Wavenumber of normal mode

k^* Most unstable wavenumber

k_a Smallest unstable wavenumber

k_c Largest unstable wavenumber

s Growth rate of normal mode

S_0 Initial gas saturation

Chapter 4

δ^* Maximum piston displacement

δ_0 Initial piston position

δ_1 Piston position at initial pore invasion

δ_2 Piston position at cavity collapse

Δ_g^0 Initial size of gas cavity

ϕ^i Porosity in invaded region (toy model)

ϕ^u Porosity in uninvaded region (toy model)

$\overline{\sigma}$ Confining stress

$\overline{\sigma}_{\text{plat}}$ Plateau stress

$\mathcal{A}$ Size of uninvaded region (toy model)

$\mathcal{A}_0$ Initial size of uninvaded region (toy model)

$\mathcal{A}_2$ Size of uninvaded region at cavity collapse (toy model)

$\mathcal{B}$ Size of invaded region (toy model)

$\mathcal{S}$ xx-component of Eulerian strain (toy model)

$\mathcal{T}_{\mathrm{pe}}$ Poroelastic timescale

h General variable

L^* Rescaled domain length

M P-wave modulus

S_g^i Gas saturation in invaded region (toy model)

t_f Final time

x_* Rescaled coordinate

$\tilde{p}_c$ Dimensionless capillary pressure

$\overline{S}_g$ Gas saturation during plateau region

Chapter 5

ω_c Clogging number

$\sigma'_{\varrho\varrho}$ Effective normal stress in radial direction

σ_F Frictional drag

τ Pore-closure parameter

ϱ Eulerian radial coordinate

$\mathcal{C}$ Compressibility

$\mathcal{J}$ Dimensionless friction coefficient

C_F Coulomb friction coefficient

K_J Jansenn coefficient

p_{atm} Atmospheric pressure

r_b Radius of hydrogel bead

r_p^0 Initial radius of pore throat

r_t Tube radius

V_g Volume of gas

Appendices

λ_i Principal stretch

$\lambda_i^{\pm}$ Tensile and compressive components of principal stretch

$\psi_{\alpha\beta}$ Interfacial energy density between phases α and β

$\sigma'_{x\varrho}$ Effective shear stress

$\mathcal{I}_i$ Integrals in analytical solution of poroelasticity

$\mathcal{U}_i$ Linearised mobility coefficients

F_{ij} Components of $\mathbb{F}$

$J^{\pm}$ Tensile and compressive components of J

Chapter 1

Introduction

Multiphase fluid flow through deformable porous media occurs in a wide range of biological and geophysical systems. Examples include methane venting from seabed sediments [Skarke et al., 2014], the formation of liquid-like condensates in biological cells [Hyman et al., 2014], meltwater flow through compacting snow [Meyer and Hewitt, 2017], transport processes within plants [Jensen and Forterre, 2022], the trapping of insulating air pockets in animal fur [Nasto et al., 2016], and degassing-driven eruptions of volcanic systems [Suckale et al., 2016]. Understanding such flows is important for quantifying the rate of greenhouse gas emissions to the atmosphere, predicting sea level rise resulting from glacier melt, and answering fundamental questions about how vital intracellular functions occur within living organisms.

Although flows through porous media that are rigid or stiff (*i.e.*, weakly deformable) have been studied extensively [Coussy, 2004, Blunt, 2017], multiphase flow through soft (*i.e.*, highly deformable) porous media remains poorly understood [Juanes et al., 2020]. A key reason for this lack of understanding is the strong two-way coupling between flow and deformation in a highly deformable system: flow can deform the pore structure, which in turn affects the flow. The physical and conceptual complexity of such systems makes them challenging to investigate, both theoretically and experimentally. Recent experimental works have

explored the coupling between deformation and multiphase flow from a variety of different perspectives, including pattern formation in frictional flows [Sandnes et al., 2011, Dumazer et al., 2016], fracturing processes in cohesive porous media [Meng et al., 2023], droplet formation in synthetic gels [Style et al., 2018, Rosowski et al., 2020a,b], and gas migration through soft granular packings [Lee et al., 2020]. There remains, however, a need for a systematic investigation of multiphase flow in highly deformable porous systems, and for the development of comprehensive theories to describe experimental and field-based observations.

Theories of *single-phase* flow through *weakly deformable* porous media are well established [Wang, 2001]. Linear poroelasticity, as developed by Biot [1941, 1956, 1962, 1972], describes the response of an elastic porous medium to flow and *infinitesimal* deformation. This theory combines Terzaghi's principle of overall stress balance [von Terzaghi, 1936] with Darcy's law for fluid flow [Darcy, 1856] and the theory of linear elasticity, within a linearised kinematic framework. *Large* deformations, which are characterised by substantial changes in the pore structure, occur when driving forces (*e.g.*, viscous pressure gradients or capillary interactions) become comparable to the strength of the solid skeleton. While a linearised description is clearly inappropriate in the presence of large deformations, the theory of large-deformation poroelasticity [Coussy, 2004, MacMinn et al., 2016] allows for such deformations by considering both non-linear kinematics and fully non-linear constitutive relations [*e.g.,* Auton and MacMinn, 2017, 2018, Fiori et al., 2023]. Other poromechanical responses, such as plastic deformations of the solid skeleton, can be captured in a similar framework via appropriate constitutive laws [*e.g.,* Auton and MacMinn, 2019, Paterson et al., 2022]. The generalisation of *linear* poroelasticity to account for multiple fluid phases remains the subject of ongoing study, but the general principles are by now relatively well established [Coussy, 2004]. In contrast, the generalisation of *large-deformation* poroelasticity for multiphase flow has attracted much less attention and remains at the frontier of modelling capabilities.

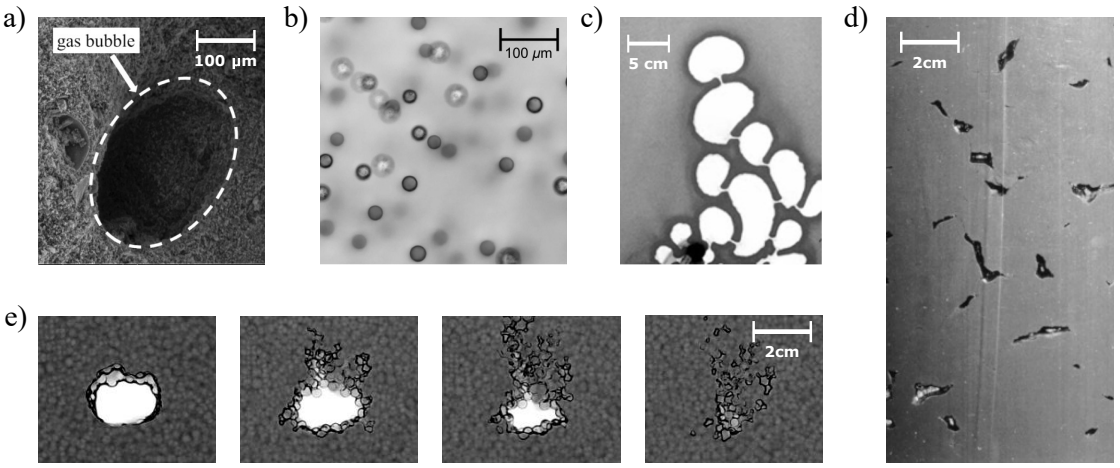

Figure 1.1: Examples of non-wetting cavities in deformable porous media. (a) SEM image of a gas cavity in marine clay [Hong et al., 2017]. (b) Fluorinated oil droplets in a silicone gel [Style et al., 2018]. (c) 'Stick-slip' bubbles in a confined, frictional packing [Sandnes et al., 2011]. (d) Gas bubbles in an estuarine sediment [Gonzalez and Sills, 2001]. (e) Compression-driven collapse of a gas cavity in a soft, granular packing (image courtesy of Jian Hui Guan). Images reproduced with permission where required.

One major challenge in modelling multiphase flow in highly deformable systems is that deformation enables the emergence of completely new flow phenomena that do not have an analogue in the rigid case, the most striking of which is the ability of the non-wetting fluid to form open (solid-free) pathways and cavities (Figure 1.1). For a porous medium containing two fluids with different wettabilities relative to the solid, these 'non-wetting cavities' may form due to capillary interactions, which make it energetically costly for the non-wetting phase to invade narrow pore throats within the solid skeleton. If the solid skeleton is sufficiently deformable, it may be energetically favourable for the non-wetting phase to instead displace the solid and form macroscopic cavities that are many times larger than the pore size. Cavity formation is resisted by various physical mechanisms, such as elasticity, inter-grain cohesion, and friction — depending on the mechanical properties of the porous medium being considered. Here, we focus on porous media in which the elasticity of the solid skeleton provides the principal resistance to deformation. In these soft porous media, a competition between capillarity and elasticity thus determines whether or not cavities are able to form in any given setting.

Many naturally occurring soft porous media experience spatially and/or temporally varying stresses resulting from, for example, changing atmospheric conditions above marine sediments [Scandella et al., 2011] or active biological processes in cells [Heidemann and Wirtz, 2004, Kothari and Cohen, 2023]. Compressing a particular porous medium can alter the balance between capillary and elastic forces, and can thus trigger the collapse of existing non-wetting cavities, forcing the non-wetting fluid into the pore space. Similarly, reducing the compressive stress may trigger the spontaneous formation of non-wetting cavities from a distribution of non-wetting fluid within the pore space. A quantitative understanding of the continuum-scale physics of cavity formation and collapse has direct application to a variety of natural and industrial problems, including predicting the structural stability of so-called 'gassy soils' [Kaminski et al., 2019, Liu et al., 2022], informing the fabrication of novel micro-structured materials [Bartlett and Style, 2020, Fernández-Rico et al., 2023], and characterising gas transport in peatlands [Chen and Slater, 2015] and nuclear waste repositories [Nuske et al., 2010].

The pore-scale physics of cavity formation are relatively well understood (*see §1.1 below*). However, no satisfactory continuum-scale model for the behaviour of non-wetting cavities currently exists. The framework of large-deformation poromechanics provides a natural starting point for developing such a theory. It is unlikely, however, that a multiphase generalisation of large-deformation poroelasticity in the ad hoc manner of multiphase linear poroelasticity will be appropriate for modelling the behaviour of non-wetting cavities. In particular, cavity formation results in the non-wetting fluid leaving the pore space, and so the traditional formulation of Darcy's law is no longer relevant for describing fluid flow. Further, it is not clear how to define a stress balance which applies generally in both cavities and the rest of the porous medium.

Recent works have attempted to bridge this modelling gap via a variety of different approaches. The work of Carrillo and Bourg [2019, 2021b] uses a Darcy–Brinkmann formulation to couple, and transition smoothly between, Darcy-like

flow within the pore space of a visco-plastic solid skeleton and Stokes flow within open pathways and cavities. This approach has been been used to study the formation of cavities via direct injection of the non-wetting fluid [Carrillo and Bourg, 2021a], but it is unclear how such an approach would generalise to other scenarios. There is a rapidly growing literature concerning the formation of non-wetting cavities within the context of synthetic gels and biological cells (as discussed further in §1.1). Although existing continuum models of this process are able to faithfully describe the formation and growth of non-wetting cavities, they typically ignore fluid flow and focus on specific experimental examples, and so are not applicable to more general flow problems.

In this thesis, we conceptualise the formation of non-wetting cavities as a process of thermodynamic phase separation, with the non-wetting fluid spontaneously separating from a fluid–fluid–solid mixture under appropriate conditions. This conceptualisation allows us to draw on the broad literature that already exists for studying phase-separation problems (*see §1.2 below*). By considering the formation of non-wetting cavities as phase separation within the framework of large-deformation poromechanics, we construct a continuum theory that captures the formation, collapse and dynamical behaviour of cavities. We focus on two test problems: (1) the spontaneous formation of cavities from a distribution of pore fluid and (2) the compression-driven collapse of a single cavity. We complement our continuum theory with a corresponding toy model and the results of table-top experiments.

1.1 Non-Wetting Cavities

Non-wetting fluid can exist in one of three distinct states in a soft porous medium: in micro-bubbles, in the pore space, and in open cavities (Figure 1.2). Micro-bubbles are individual blobs of non-wetting fluid that are smaller than the pore size of the surrounding porous medium (Figure 1.2a). As the size of micro-bubbles

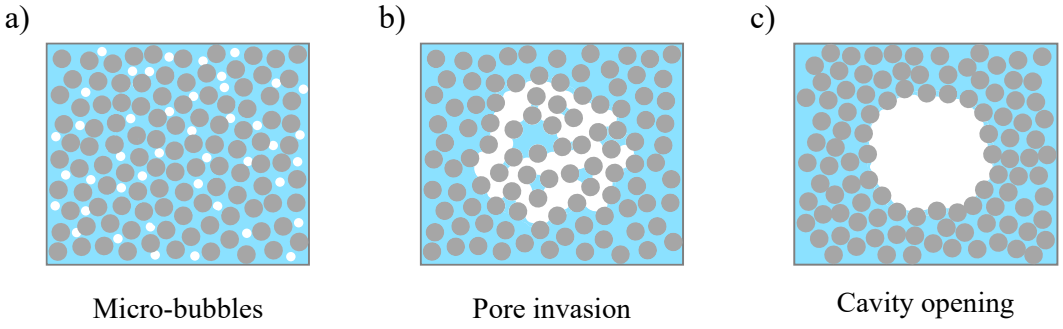

Figure 1.2: The different states of non–wetting-phase occupancy within a soft porous medium with a granular microstructure: (a) the non-wetting phase (white) can form disconnected 'micro-bubbles' smaller than the pore size, (b) the non-wetting phase and the wetting phase (blue) can coexist within the pore space, with the non-wetting phase forming a connected domain over many pores, or (c) the non-wetting phase can displace the solid grains (grey) to form an open cavity.

increases towards the pore size, their growth will necessarily be restricted by the presence of the solid skeleton. For a particular blob of non-wetting fluid to grow larger than a single pore, it must either invade narrow pore throats (Figure 1.2b) or form an open cavity by displacing solid (Figure 1.2c). Which of these two states is most likely depends on the degree to which capillary forces are strong enough to deform the porous medium.

To understand the physical mechanisms that control cavity formation and pore invasion, we consider a pore-scale description of non-wetting fluid advancing into a narrow pore throat (Figure 1.3). When both non-wetting and wetting fluid are in contact with the solid grains, the equilibrium contact angle ϑ_c (*i.e.*, the angle at which the fluid–fluid interface meets the solid surfaces) is set by the associated interfacial energies between each phase, as expressed by the Young equation [Young, 1805],

$$\gamma_{ws} + \gamma_{ns} + \gamma_{wn} \cos \vartheta_c = 0, \tag{1.1}$$

where γ_{ws}, γ_{ns} and γ_{wn} are the interfacial energies of the wetting–solid, non-wetting–solid and wetting–non-wetting interfaces, respectively. These interfacial energies, and thus the contact angle, are fixed material properties of a given fluid–fluid–solid system. As non-wetting fluid advances into a pore throat, the curvature

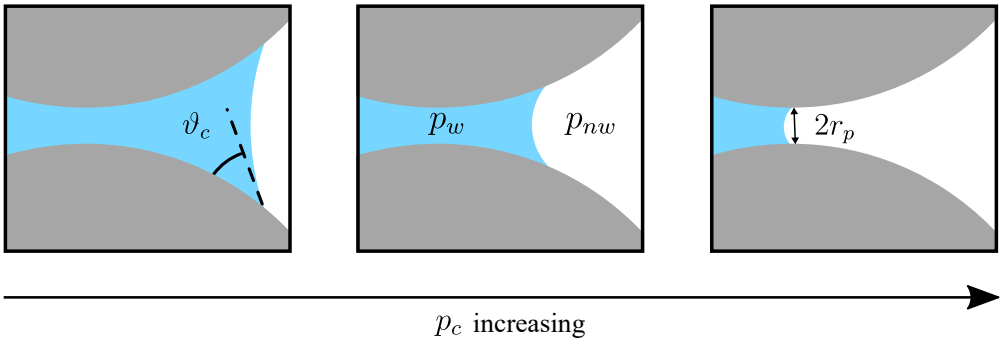

Figure 1.3: The advance of a fluid–fluid interface into a pore throat. As non-wetting fluid advances toward the narrowest point, the curvature of the fluid–fluid interface increases, corresponding to an increase in capillary pressure, p_c. When the interface reaches the narrowest point (rightmost panel), p_c is maximum, and is known as the capillary entry pressure, p_c^e.

of the fluid–fluid meniscus must increase to preserve the contact angle as the pore throat narrows. This increase in curvature leads to an increase in the difference between the pressure in the non-wetting fluid, p_{nw}, and the pressure in the wetting fluid, p_{w}. This pressure difference is known as the capillary pressure, $p_c \equiv p_{\mathrm{nw}} - p_{\mathrm{w}}$, and is determined by the Young-Laplace law [Young, 1805, de Laplace, 1808, Blunt, 2017],

$$p_c = \frac{2\gamma_{wn}\cos\vartheta_c}{r_p}, \tag{1.2}$$

where r_p is the radius of the pore throat at the fluid–fluid interface (taking the throat to be cylindrical). For the non-wetting fluid to fully invade the pore throat and pass into the next pore, p_c must exceed the capillary entry pressure, p_c^e, which is the capillary pressure at the narrowest point in the pore throat. The capillary pressure also leads to a corresponding force on the solid grains. In a soft porous medium, this force is resisted by the elasticity of the solid skeleton. If the solid skeleton is soft enough to admit large deformations before p_c exceeds p_c^e, then cavity formation will occur and the non-wetting fluid will not invade the pore space. Conversely, if p_c reaches p_c^e before substantial deformation of the solid skeleton is possible, then pore invasion will take place.

Non-wetting cavities are found in a wide range of soft porous media (*e.g.*, sediments [Boudreau et al., 2005, Hong et al., 2017], peatlands [Chen and Slater, 2015],

gels [Style et al., 2018, Rosowski et al., 2020a,b, Fernández-Rico et al., 2023], biological tissues [Walsh, 2017, Zhang et al., 2021], and food products [Pugh et al., 2023]). The two most well-studied examples are gas bubbles in soft sediments and liquid droplets in synthetic gels. Many sea-bed sediments contain large amounts of gas (usually methane or carbon dioxide) as a result of biogenic and thermogenic decomposition of organic matter. Unlithified sediments are able to support large deformations, and can display either elastic (muddy sediments; grain size $\lesssim 10\,\mu$m) or plastic (sandy sediments; grain size $\gtrsim 10\,\mu$m) properties [Boudreau et al., 2005]. The presence of gas within such sediments strongly affects these mechanical properties, which are important for assessing the stability of offshore foundations and the likelihood of submarine landslides, which are a widespread geohazard [Liu et al., 2022]. As such, 'gassy sediments' have been studied extensively from the perspective of geotechnical engineering. In addition to conducting traditional geomechanical tests, previous works have studied the conditions under which cavities form, the typical size and shape of cavities, and the effect of grain size on cavity formation [Gonzalez and Sills, 2001, Boudreau, 2012, Terzariol et al., 2021]. As well as affecting the mechanical properties of the sediment, cavities also affect the migration of gas through the sediment itself. The rate and frequency of gas venting depend strongly on the dominant migration mechanism within the sediment (*i.e.*, whether gas migrates through the pore space or via open cavities and pathways) [Lee et al., 2020]. In turn, the nature of venting events and the typical size of vented bubbles have important consequences for marine ecosystems, as well as affecting the amount of (typically greenhouse) gas that eventually rises through the overlying ocean into the atmosphere [McGinnis et al., 2006]. Kaminski et al. [2019] and Liu et al. [2022] provide recent and comprehensive overviews on previous research into gassy sediments.

The work of Sills and Wheeler in the 1980s and 90s provided early mathematical models for cavity formation in soft sediments [Wheeler, 1986, 1988a,b, 1990, Sills et al., 1991, Sills and Wheeler, 1992]. These authors conceptualise cavities as large

spherical voids embedded within an otherwise liquid-saturated medium, referred to as the 'large bubble model'. In the large bubble model, cavities are fixed in position, but can change in size due to diffusion of dissolved gases through the pore liquid. The dissolution or exsolution of gas is determined by the pressure of the gas phase, which is in turn coupled to the pore pressure via surface tension at the gas–liquid interface. The rest of the porous medium is considered to be a fully saturated soil surrounding, but not including, the cavities. This model is used to predict elastic moduli and consolidation behaviour of gassy sediments to compare to geomechanical testing. This model accounts for cavity collapse via 'bubble flooding' when gas pressure is no longer large enough to prevent liquid from entering the cavity, but the possibility of cavity collapse via pore invasion (with gas pressure large enough for the gas to invade the pore space) is not considered.

The formation of liquid droplets in synthetic gels (commonly referred to as liquid–liquid phase separation) has attracted significant recent attention, driven by applications to the self-organisation of biomolecular condensates [Hyman et al., 2014]. A series of recent experiments [Style et al., 2018, Rosowski et al., 2020a,b, Fernández-Rico et al., 2023] demonstrate how fluorinated oil droplets can separate from a polymer gel to form 'network-excluding' cavities and channels throughout the experimental medium (see Figure 1.1b). Results of these experiments have focused on investigating the rate of cavity formation following a change in external conditions (in this case, a sudden change in temperature), characterising typical cavity sizes, and studying the localisation of cavities due to gradients in material properties. Modelling attempts to explain such phenomena have typically utilised an energy-based approach [Kothari and Cohen, 2020, 2023, Wei et al., 2020, Vidal-Henriquez and Zwicker, 2020, 2021, Ronceray et al., 2022, Qiang et al., 2023], with particular emphasis on the chemical interactions between different phases and the specific form of the elasticity law required to reproduce experimental results. Models of liquid–liquid phase separation in polymer gels typically neglect the poromechanical response of the elastic network, and so are unlikely to capture the effects of

fluid flow or elastic interactions through the solid matrix. Unlike work on gassy sediments, they also typically ignore any impact of cavities on the macroscopic mechanical properties of the composite material. Whilst this is a reasonable approximation for studying the parameter regime relevant to synthetic gels, such an approximation is inappropriate for studying non-wetting cavities in other physical settings. Further, gels have a fibrillar, rather than granular, microstructure. As such, studies of liquid–liquid phase separation in gels typically utilise mechanical models that do not readily generalise to broader classes of material microstructure.

Studies of liquid–liquid phase separation in elastic networks have focused almost exclusively on the formation of droplets that completely exclude the elastic network from the separated phase. The recent work of Ronceray et al. [2022] is (to the best of our knowledge) the first to hypothesise the possibility of other phase-separated states occurring in these systems. The authors refer to three possible outcomes of liquid–liquid phase separation: microdroplets, network permeation, and cavitation. These possibilities are directly analogous to the micro-bubble, pore-invasive and cavity-forming regimes previously identified in geotechnical studies of gassy sediments, as highlighted in the work of Wheeler [1988a] and illustrated above in Figure 1.2. Until very recently, cavity formation has been the only state observed in experiments in either synthetic gels or biological organisms, primarily due to the extremely small pore size which is typical of these systems ($\sim 10\,\mathrm{nm}$). The recent work of Liu et al. [2023], however, has demonstrated the formation of pore-invasive liquid droplets in biopolymer networks, and investigated their possible transition to the network-excluding state.

1.2 Phase Separation

Phase separation is the separation of a homogeneous, but out of equilibrium, mixture into various distinct phases, each rich in one of the components of the original

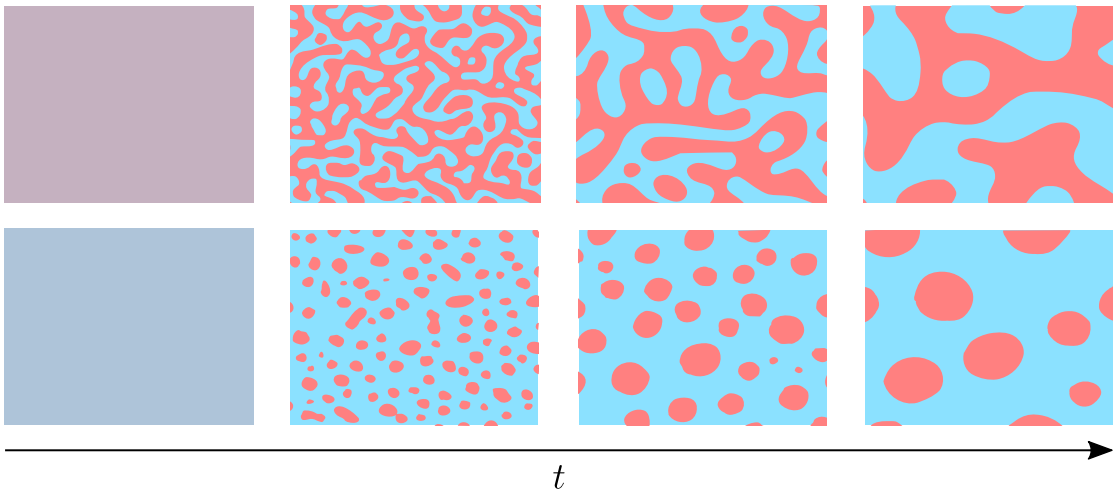

Figure 1.4: A schematic showing the separation and coarsening of a two-component mixture via spinodal decomposition (top panels) and via nucleation and growth (bottom panels). Blue and red colours indicate the two different components of the mixture as it separates from an initially homogeneous state.

mixture. The separation of immiscible fluids, such as water and oil, into segregated oil-rich and water-rich domains is an everyday example of such a process. Phase separation is fundamentally a thermodynamic process, in which the system is driven towards an equilibrium state of minimum energy. There are two distinct modes by which the phase separation of a binary (two-component) mixture can occur: spinodal decomposition, and nucleation and growth. Spinodal decomposition occurs when there is no energy barrier to the formation of each phase, and is characterised by spontaneous separation throughout the mixture (Figure 1.4, top). Nucleation and growth occurs when spontaneous separation is inhibited by an energy barrier. In this case, phase-separated domains will form at particular nucleation sites of large concentration, and then grow from these (Figure 1.4, bottom). In both cases, it is energetically favourable for different domains of the same phase to merge over time to form larger regions, until, eventually, each phase exists within a single, connected region of space. This process of thermodynamic coarsening is known as Ostwald ripening [Ostwald, 1897, Voorhees, 1992].

Theories of phase separation were first developed in the 1950s and 60s to describe the solidification of metal alloys. The pioneering work of Cahn and coworkers [Cahn and Hilliard, 1958, 1959, Cahn, 1959, 1961, Allen and Cahn, 1979, Larché

and Cahn, 1992] borrows ideas from the theory of phase transitions in ferromagnetic systems to introduce a free energy functional that governs the separation of binary mixtures. Cahn's approach relies on the use of an 'order parameter', which can be any continuous property of the mixture that has a distinct value in each of the phase-separated states; the concentration of one of the components is a common choice. For a binary fluid mixture such as oil and water, for example, the concentration of oil molecules would be very close to one in oil droplets, and very close to zero in water.

The free energy functional of Cahn and Hilliard [1958] for a binary system depends on both the order parameter and its spatial gradients. A typical Cahn–Hilliard-style free energy for an order parameter c is

$$\mathcal{F} = \int \varpi\left(c\right) + \mathcal{K}|\nabla c|^2 \mathrm{d}V. \tag{1.3}$$

Here, $\varpi(c)$ is the energy of a state of uniform concentration c, $\mathcal{K}$ represents the strength of interfacial tension, and the integral is taken over the whole volume of the system. The form of $\varpi(c)$ depends on the specific details of the problem being considered, but is often taken to be a double-well with minima centred on the equilibrium concentration of each phase. Whether or not phase separation occurs depends on the particular shape of $\varpi(c)$. The shape of $\varpi(c)$ may also depend on an external parameter, such as temperature or pressure. As this parameter varies, $\varpi(c)$ may change such that it no longer takes the form of a double-well. Figure 1.5a illustrates such behaviour for an arbitrary external parameter $\mathcal{P}$. For the example of oil and water, $\mathcal{P}$ could represent the amount of surfactant present. For small $\mathcal{P}$ (light orange line), $\varpi(c)$ is a symmetric double-well with minima at $c \sim 0.1$ and $c \sim 0.9$. In this case, an initially mixed state ($c = 0.5$) will reduce its total energy by separating into distinct regions corresponding to concentrations of $c \sim 0.1$ and $c \sim 0.9$. As $\mathcal{P}$ increases, $\varpi(c)$ transitions from a double-well to a single well with a minimum at $c = 0.5$. An initially homogeneous mixture will therefore not phase

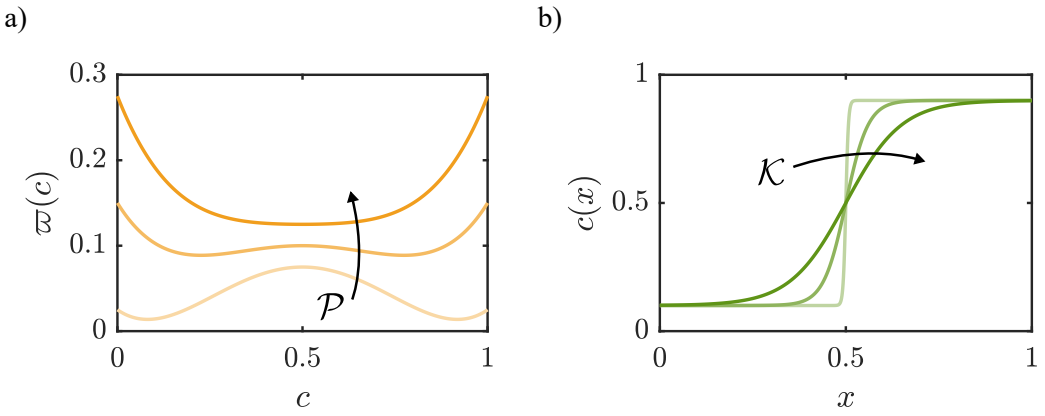

Figure 1.5: (a) A plot of $\varpi(c)$ for a typical Cahn–Hilliard free energy for an oil–water emulsion. As the parameter $\mathcal{P}$ increases (light to dark orange), $\varpi(c)$ transitions from a double-well to a single, central minimum. In this example, we have taken $\varpi(c) = 2\left(c - \frac{1}{2}\right)^2 \left(c^2 - c + \frac{1-\mathcal{P}^{-1}}{2}\right) + \frac{12-5\mathcal{P}^{-1}}{80}$. (b) Typical shape of an interface between phases for a Cahn–Hilliard free energy. Concentration smoothly interpolates from $c \sim 0.1$ to $c \sim 0.9$ across a diffuse interface. As $\mathcal{K}$ increases (light to dark green), the interface becomes less steep.

separate in this case; it is energetically favourable for the system to remain mixed.

The interface between two phase-separated regions manifests as a steep, but smooth, change in the value of the order parameter over a finite spatial width. Figure 1.5b shows representative interfaces for several values of $\mathcal{K}$. We see that in the bulk of each phase (away from the interface), c is uniform and equal to the values of c at which $\varpi(c)$ is minimum. Across the interface between the two phases, c interpolates smoothly from $c \sim 0.1$ to $c \sim 0.9$. For the standard Cahn–Hilliard free energy (Equation 1.3), the shape of the interface is given by a hyperbolic tangent. The value of $\mathcal{K}$ controls the width of this diffuse interface. As $\mathcal{K}$ decreases, the interface becomes steeper; in the asymptotic limit $\mathcal{K} \to 0$, we recover a classical sharp interface.

The dynamical behaviour of a binary mixture as it undergoes phase separation is governed by either the Cahn–Hilliard or Allen–Cahn equation. The Cahn–Hilliard equation is used when the order parameter corresponds to a conserved physical quantity, such as component concentration for immiscible fluids. The Allen–Cahn equation is used when the order parameter corresponds to an unconserved quantity,

such as when chemical reactions allow one component to transform into another. Generalisations of the Cahn–Hilliard and Allen–Cahn equations have been used to describe a wide range of problems in fluid dynamics and soft matter [Anderson et al., 1998, Doi, 2013], including viscous fingering instabilities [Cueto-Felgueroso and Juanes, 2014, Fu et al., 2016, 2017], pattern formation in active nematics [Mueller and Doostmohammadi, 2021], crust formation in methane-hydrate systems [Fu et al., 2018, 2020], bubble nucleation in magma [Gardner et al., 2023], and multiphase flow in rigid porous media [Cueto-Felgueroso and Juanes, 2008, Schreyer and Hilliard, 2021]. Although many Cahn–Hilliard-style models focus on two phases, these models can be generalised to an arbitrary number of phases [Kim and Lowengrub, 2005].

Historically, most Cahn–Hilliard-style models are derived via a relatively ad hoc variational approach. Gurtin and Fried [Gurtin, 1989, 1996, Fried and Gurtin, 1993, 1994, Gurtin et al., 1995] later developed a thermodynamically consistent framework for these models by introducing the concept of subscale 'microforces' associated with changes in local composition. This framework also allows for the natural inclusion of a deformable solid phase via conservative (elastic) and/or dissipative (plastic) contributions to the free energy [Gurtin, 1996], which are otherwise challenging to capture consistently in a traditional Cahn–Hilliard model.

In this thesis, we study the formation of non-wetting cavities in a poroelastic medium, which we conceptualise as a phase separation process. The effect of an elastically deformable solid phase on phase-separation processes has been studied from several different perspectives. In particular (and as discussed in §1.1), the problem of liquid–liquid phase separation within an elastic network has attracted substantial recent attention due to extensive applications in biology and materials science. Similarly, elastically modulated phase separation has been well studied within the context of hydrogel systems [Onuki and Puri, 1999, Zhou et al., 2010, Hennessy et al., 2020, Celora et al., 2022, 2023]. It is by now well understood that the presence of an elastic network fundamentally alters the phase-separation

process by introducing an energetic cost to the rearrangements that are needed for phase separation to occur. This energetic cost limits the final size of phase-separated domains [Wei et al., 2020], decreases the rate of post-separation coarsening [Onuki and Puri, 1999], and in some cases can suppress phase separation entirely [Wei et al., 2020, Kothari and Cohen, 2020].

1.3 Thesis Outline

In this thesis, we investigate the formation and collapse of non-wetting cavities in soft (elastic) porous media. We focus on non-cohesive, frictionless granular media, but generalisation to other similar systems would be relatively straightforward and would not change the core physical processes investigated here. The primary achievement of this thesis is the development and analysis of a novel continuum model that captures the dynamics of non-wetting cavities in a thermodynamically consistent manner. We analyse the predictions of our model for two relevant test problems. We also develop a simple toy model that complements our continuum approach and informs some of our modelling choices. Finally, we test the predictions of these theories via a series of representative experiments.

The structure of the thesis is as follows. In Chapter 2, we develop our continuum model and benchmark it against a series of well-studied limiting cases. In Chapter 3, we apply our model to the first test problem: the spontaneous formation of non-wetting cavities from a distribution of fluids in the pore space. We consider the parameter regimes under which cavity formation occurs, and investigate the characteristic size of cavities that result, via both numerical simulations and linear stability analysis. Further, we construct a reduced, equilibrium formulation of our full model that elucidates the different physical effects that control cavity formation. In Chapter 4, we study our second test problem: the deformation-driven collapse of cavities under increasing compression. We conduct numerical simulations to investigate the compressive stress at which a cavity begins to collapse, and

the parameters that control this process. We couple this analysis with a simple toy model that provides a link between the phenomenological parameters of our continuum model and concrete physical quantities. In Chapter 5, we investigate compression-driven cavity collapse experimentally by compressing a packing of hydrogel beads with a permeable piston. We study the phenomenology of cavity collapse and compare to the predictions of our theory. We also investigate the reversibility of cavity collapse under fluctuating confinement, as well as the impact of additional physical effects not considered in our full model. Finally, in Chapter 6, we summarise our findings and highlight promising directions for future work.

The model development, numerical simulation, and linear stability analysis presented in Chapters 2 and 3 are published in a recent journal article:

> *Fluid–fluid phase separation in a soft porous medium,* **O. W. Paulin,** *L. C. Morrow, M. G. Hennessy, and C. W. MacMinn; Journal of the Mechanics and Physics of Solids 164:104892 (2022)*

The rest of this thesis is as yet unpublished.

Chapter 2

Model Development

The model derivation and benchmarking presented in this chapter constitute a minor extension to the work published in Paulin et al. [2022].

Cahn–Hilliard-style models (commonly referred to as phase-field models) provide a powerful framework for modelling phase-separation processes [*e.g.*, Provatas and Elder, 2010]. Phase-field modelling is a diffuse-interface method, in which classical free boundaries and associated interfacial jump conditions are replaced by an auxiliary field known as an order parameter that interpolates smoothly between different phases across the diffuse interface, and indicates phase identity. Phase-field models reduce to an associated sharp-interface model in the limit of zero interfacial width [Caginalp, 1989, Elder et al., 2001], although this reduction is not always straightforward. The physical meaning of a sharp-interface limit is unclear in porous media, which are naturally represented as diffuse-interface systems at the continuum (Darcy) scale.

Phase-field models for single-phase flow through deformable porous media have previously been developed within the context of hydraulic fracturing [Santillán et al., 2018]. In such models, the phase-field is primarily used to facilitate the numerical representation of a moving boundary, rather than as a means of capturing transitions between different phases. Similarly, the very recent work of Guével

et al. [2023] utilises a phase-field approach to describe the multiphase fracturing of cohesive poroelastic media, neglecting the effect of capillary interactions. Sciarra and coworkers recently developed a phase-field theory of multiphase flow in deformable porous media [Sciarra, 2016, Ommi et al., 2022a,b], including capillary effects, to study drainage and imbibition in soils, however this model does not incorporate the ability of the non-wetting fluid to separate from the pore space and form cavities.

In this chapter, we develop a continuum model for the formation of non-wetting cavities within a soft porous medium. By conceptualising the transition between pore invasion and cavity formation as a phase-separation process, our phase-field model captures the competing physical processes in a thermodynamically consistent manner. In §2.1, we derive our model by extending the work of Hennessy et al. [2020] to include an additional fluid phase and to allow for elastic degradation of the solid skeleton via a damage model [Miehe et al., 2010b, Tang et al., 2019]. Our derivation follows the approach of Gurtin [1996], using balance laws to set out an energy inequality that imposes restrictions on the allowable constitutive behaviours. In §2.2, we study the predictions of our model in various limiting cases, benchmarking against previous results.

2.1 Model Derivation

We begin by considering a mixture of three phases, of which two are fluids and one is a solid. At the pore scale, these phases exist within separate domains separated by sharp interfaces. At the continuum (Darcy) scale, however, these phases are mixed and the proportion of each at a particular point in space and time is measured by its volume fraction. The volume fractions thus serve as natural phase-field order parameters that can be used to distinguish the physical characteristics of different regions, and to smoothly interpolate between them. The interactions of these phases are governed by balance laws, and by a thermodynamic framework

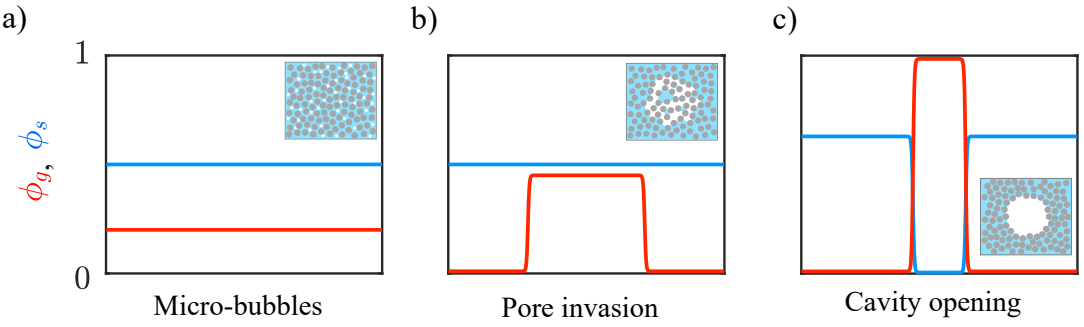

Figure 2.1: An illustration of the expected phase-field representations of (a) micro-bubbles, (b) pore invasion, and (c) cavity formation, showing how gas volume fraction ϕ_g (red) and solid volume fraction ϕ_s (blue) vary across the centre-line of each inset schematic.

that drives the system toward minima of its total free energy, as described in detail below.

We take the solid phase to be a porous skeleton comprising non-cohesive, incompressible solid 'grains'. The pore space between the grains is occupied by two immiscible, incompressible fluid phases. For clarity and without loss of generality, we refer to these fluids as 'liquid' and 'gas', where the gas is the non-wetting phase. The key feature of our model is that, under certain conditions, it is energetically favourable for the gas to separate from the other two phases by forming open cavities. The phase-field representation corresponding to each possible state of gas occupancy (micro-bubbles, pore invasion and cavity formation) is illustrated in Figure 2.1.

To formulate our model, we begin with the kinematics of the mixture (§2.1.1). We then formulate balance laws for mass and momentum (§2.1.2) and consider the thermodynamics of the mixture (§2.1.3). We formulate a free energy that captures the energetic characteristics of our system (elasticity, damage, and gas–liquid–solid interactions; §2.1.4). We close the model by using thermodynamic arguments to determine constitutive relationships that link the free energy to the various quantities in our balance laws (§2.1.5). Finally, we simplify our model to the case of a one-dimensional (1D) system (§2.1.6).

2.1.1 Kinematics

Fluid-flow problems are typically posed in an Eulerian reference frame (fixed in space), whereas solid-mechanics problems are typically posed in a Lagrangian reference frame (fixed to the solid material). For a poromechanical system, however, the fluids and the solid co-exist and must be considered in the same reference frame. To do so, it is convenient to begin by defining both frames and the relationship between them.

The deformation of the solid skeleton is defined by comparing its current (deformed) state to an undeformed (relaxed) reference state. The Lagrangian coordinate $\mathbf{X}$ refers to the reference state and the Eulerian coordinate $\mathbf{x}$ refers to the current state. We denote spatial gradients with respect to the Lagrangian and Eulerian coordinates by ∇_0 and ∇, respectively. The Lagrangian displacement of the solid is then $\mathbf{U}_s(\mathbf{X},t) = \mathbf{x}(\mathbf{X},t) - \mathbf{X}$ and the Eulerian displacement is $\mathbf{u}_s(\mathbf{x},t) = \mathbf{x} - \mathbf{X}(\mathbf{x},t)$. The deformation gradient tensor, $\mathbb{F}$, describes the deformation of the solid skeleton relative to its reference state,

$$\mathbb{F} = \nabla_0 \mathbf{x}. \tag{2.1}$$

Note that we use the convention $(\nabla \mathbf{A})_{ij} = \frac{\partial A_i}{\partial x_j}$ for a general vector field $\mathbf{A} = A_i \hat{\mathbf{e}}_i$ and $(\nabla \cdot \mathbb{B})_i = \frac{\partial B_{ij}}{\partial x_j}$ for a general tensor field $\mathbb{B} = B_{ij}\hat{\mathbf{e}}_i\hat{\mathbf{e}}_j$, where $\hat{\mathbf{e}}_i$ and $\hat{\mathbf{e}}_j$ are Cartesian unit vectors and where we have adopted the Einstein summation convention. Using the definitions above, $\mathbb{F}$ is related to $\mathbf{U}_s$ and $\mathbf{u}_s$ via

$$\mathbb{F} = \mathbb{I} + \nabla_0 \mathbf{U}_s = \left[\mathbb{I} - \nabla \mathbf{u}_s\right]^{-1}, \tag{2.2}$$

where $\mathbb{I}$ is the identity tensor.

The volume fraction of each phase can be measured relative to either the relaxed or deformed configurations. The nominal volume fractions, φ_α, measure the volume of phase α per unit reference bulk volume, whereas the true volume fractions, ϕ_α,

measure the volume of phase α per unit current bulk volume, where $\alpha = s,\ l,\ g$ indicates the solid, liquid, and gas phases, respectively. These volume fractions are related by $\varphi_\alpha = \phi_\alpha J$, where the Jacobian determinant, $J = \det(\mathbb{F})$, measures the ratio of current (deformed) bulk volume to reference (relaxed) bulk volume and is thus equal to one in the reference state. The no-void condition can thus be expressed in two ways,

$$\sum_\alpha \varphi_\alpha = J \quad \text{and} \quad \sum_\alpha \phi_\alpha = 1. \tag{2.3}$$

A result of the no-void condition is that any two of the three volume fractions fully determine the local composition.

The incompressibility of the solid grains requires that the nominal volume fraction of solid must remain unchanged during deformation, such that $\varphi_s \equiv \varphi_s^0 \equiv \phi_s^0$, where $\varphi_s^0 \equiv \phi_s^0$ is the solid fraction in the reference state, which we take to be uniform for simplicity. As a result,

$$J = \frac{\phi_s^0}{\phi_s}. \tag{2.4}$$

It is also convenient to define the true porosity, $\phi = \phi_g + \phi_l = 1 - \phi_s$, and the relaxed porosity, $\phi_0 = 1 - \phi_s^0$. Below, we develop evolution equations for ϕ_g and ϕ and then evaluate $\phi_l = \phi - \phi_g$ and $\phi_s = 1 - \phi$ as needed.

2.1.2 Balance Laws

We formulate evolution equations for ϕ_g and ϕ by first considering conservation of mass for each phase. In the Eulerian frame, conservation of mass can be written

$$\frac{\partial}{\partial t}\left(\rho_\alpha \phi_\alpha\right) + \nabla \cdot \left(\rho_\alpha \phi_\alpha \mathbf{v}_\alpha\right) = 0, \tag{2.5}$$

where ρ_α and $\mathbf{v}_\alpha$ are the density and local velocity of phase α, respectively. We assume for simplicity that all three phases are incompressible, meaning that ρ_α is a constant. The true volume flux, $\mathbf{w}_\alpha$, of phase α relative to the solid skeleton is

$$\mathbf{w}_\alpha = \phi_\alpha \left(\mathbf{v}_\alpha - \mathbf{v}_s\right). \tag{2.6}$$

Note that $\mathbf{w}_\alpha$ is commonly referred to as the Darcy flux in hydrological literature. We reduce Equations (2.5) to two evolution equations, one each for ϕ_g and ϕ, and an elliptic equation for the total mixture flux, $\mathbf{q} \equiv \sum_\alpha \phi_\alpha \mathbf{v}_\alpha = \mathbf{v}_s + \mathbf{w}_g + \mathbf{w}_l$, by eliminating the phase velocities in favour of the relative fluxes. The result of these manipulations is

$$\frac{\partial \phi_g}{\partial t} + \nabla \cdot (\phi_g \mathbf{q}) + \nabla \cdot \left[(1-\phi_g)\,\mathbf{w}_g - \phi_g \mathbf{w}_l\right] = 0, \tag{2.7a}$$

$$\frac{\partial \phi}{\partial t} + \nabla \cdot (\phi \mathbf{q}) + \nabla \cdot \left[(1-\phi)\,(\mathbf{w}_g + \mathbf{w}_l)\right] = 0, \tag{2.7b}$$

$$\nabla \cdot \mathbf{q} = 0. \tag{2.7c}$$

We derive thermodynamically consistent constitutive expressions for the fluxes $\mathbf{w}_\alpha$ in §2.1.5. We express mass conservation in Lagrangian form by using the Reynolds transport theorem to rewrite Equation (2.5) as

$$\frac{\partial}{\partial t}\left(\rho_\alpha \varphi_\alpha\right) + \nabla_0 \cdot \left(\rho_\alpha \mathbf{W}_\alpha\right) = 0, \tag{2.8}$$

where the nominal volume flux, $\mathbf{W}_\alpha$, is related to the true flux via $\mathbf{W}_\alpha = J\mathbb{F}^{-1} \cdot \mathbf{w}_\alpha$ (Nanson's formula).

Further restrictions can be imposed on our system by considering conservation of momentum. The true (Cauchy) total stress, $\mathbb{T}$, measures the total internal force per unit current area within the mixture. In the absence of body forces and neglecting inertia, mechanical equilibrium requires that $\mathbb{T}$ must be divergence free,

$$\nabla \cdot \mathbb{T} = 0. \tag{2.9}$$

In the Lagrangian frame, momentum balance is most naturally expressed in terms of the first Piola-Kirchhoff stress, $\mathbb{P}$,

$$\nabla_0 \cdot \mathbb{P} = 0, \tag{2.10}$$

where $\mathbb{P} = J\mathbb{T} \cdot \mathbb{F}^{-\intercal}$ measures the total internal force per unit reference area within the mixture.

2.1.3 Thermodynamics

The first law of thermodynamics requires that the rate of change of free energy in a particular control volume, via mass flux into the volume or working due to internal compositional changes, cannot exceed the rate of work done by external forces. Following Gurtin [1996], we formalise this restriction by considering the change in the total Helmholtz free energy of a bulk material element $\mathcal{V}_0$ in the Lagrangian frame. We denote the local Helmholtz free energy per unit reference volume by ψ. The rate of change of free energy per unit mass of phase α due to a net flux of phase α is measured by the chemical potential, μ_α. The key ingredient in Gurtin's approach is that changes in energy resulting from changes in composition, as measured by changes in φ_α, can be represented by the action of a nominal vector 'microstress', $\boldsymbol{\xi}_\alpha$, acting on the boundary of the material element. This microstress is intended to capture the net work done by subscale physical mechanisms such as capillary forces that would otherwise not be resolved at the continuum scale. Mechanical damage to the solid skeleton can be captured in the same way by introducing a damage parameter, d, and an associated microstress, $\boldsymbol{\xi}_d$ (see §2.1.4 below). The working of external forces is represented by the action of the total stress, $\mathbb{P}$, on the boundary $\partial\mathcal{V}_0$ of the material element. Summing these different contributions leads to a dissipation inequality,

$$\frac{\mathrm{d}}{\mathrm{d}t}\int_{\mathcal{V}_0}\psi \mathrm{d}V \leq -\int_{\partial\mathcal{V}_0}\rho_g\mu_g\mathbf{W}_g\cdot\hat{\mathbf{n}}\mathrm{d}A - \int_{\partial\mathcal{V}_0}\rho_l\mu_l\mathbf{W}_l\cdot\hat{\mathbf{n}}\mathrm{d}A + \int_{\partial\mathcal{V}_0}\left(\boldsymbol{\xi}_g\cdot\hat{\mathbf{n}}\right)\dot{\varphi}_g\mathrm{d}A$$
$$+\int_{\partial\mathcal{V}_0}\left(\boldsymbol{\xi}_l\cdot\hat{\mathbf{n}}\right)\dot{\varphi}_l\mathrm{d}A + \int_{\partial\mathcal{V}_0}\left(\boldsymbol{\xi}_s\cdot\hat{\mathbf{n}}\right)\dot{J}\mathrm{d}A + \int_{\partial\mathcal{V}_0}\left(\boldsymbol{\xi}_d\cdot\hat{\mathbf{n}}\right)\dot{d}\mathrm{d}A + \int_{\partial\mathcal{V}_0}\left(\mathbb{P}\cdot\hat{\mathbf{n}}\right)\cdot\dot{\mathbf{u}}_s\mathrm{d}A, \tag{2.11}$$

where $\hat{\mathbf{n}}$ is the unit vector normal to $\partial\mathcal{V}_0$, and $\dot{\square}$ is a partial derivative with respect to time in the Lagrangian frame. Grouping the surface integrals in Equation (2.11) and then using the divergence theorem leads to a local form of this inequality,

$$\dot{\psi} + \nabla_0\cdot\left(\rho_g\mu_g\mathbf{W}_g + \rho_l\mu_l\mathbf{W}_l - \dot{\varphi}_g\boldsymbol{\xi}_g - \dot{\varphi}_l\boldsymbol{\xi}_l - \dot{J}\boldsymbol{\xi}_s - \dot{d}\boldsymbol{\xi}_d - \mathbb{P}\cdot\dot{\mathbf{u}}_s\right) \leq 0. \tag{2.12}$$

We must also ensure that the no-void condition (Equation 2.3) is satisfied. This constraint can be incorporated into the above thermodynamic restriction through the use of a Lagrange multiplier, p, which is the thermodynamic mixture pressure. To make this constraint compatible with the dimensions of the dissipation inequality, we differentiate Equation (2.3) with respect to time and use Jacobi's formula to evaluate the derivative of J, arriving at

$$\dot{J} = J\mathbb{F}^{-\intercal}\colon\dot{\mathbb{F}} = \dot{\varphi}_g + \dot{\varphi}_l. \tag{2.13}$$

We combine the dissipation inequality (Equation 2.12) with the incompressibility constraint (Equation 2.13) by multiplying the latter by p and summing the two.

Finally, we elucidate the consequences of this inequality by asserting that ψ can, in general, be a function of composition via φ_g, φ_l, d, and their gradients, and of deformation via $\mathbb{F}$ and $\nabla_0 J$, so that $\psi = \psi\left(\varphi_g, \varphi_l, d, \mathbb{F}, \nabla_0\varphi_g, \nabla_0\varphi_l, \nabla_0 d, \nabla_0 J\right)$. Note that we could equivalently write ψ as a function of true volume fractions and their Eulerian gradients, but it is convenient to use nominal quantities as the independent variables here. We then use the chain rule as well as conservation of

mass (Equation 2.8) and conservation of momentum (Equation 2.10) to arrive at

$$\begin{aligned}
&\left(\frac{\partial\psi}{\partial\varphi_g} - \rho_g\mu_g + p - \nabla_0\cdot\boldsymbol{\xi}_g\right)\dot{\varphi}_g + \left(\frac{\partial\psi}{\partial\varphi_l} - \rho_l\mu_l + p - \nabla_0\cdot\boldsymbol{\xi}_l\right)\dot{\varphi}_l \\
&+ \left(\frac{\partial\psi}{\partial\nabla_0\varphi_g} - \boldsymbol{\xi}_g\right)\cdot\nabla_0\dot{\varphi}_g + \left(\frac{\partial\psi}{\partial\nabla_0\varphi_l} - \boldsymbol{\xi}_l\right)\cdot\nabla_0\dot{\varphi}_l + \left(\frac{\partial\psi}{\partial d} - \nabla_0\cdot\boldsymbol{\xi}_d\right)\dot{d} \\
&+ \left(\frac{\partial\psi}{\partial\nabla_0 d} - \boldsymbol{\xi}_d\right)\cdot\nabla_0\dot{d} + \left(\frac{\partial\psi}{\partial\mathbb{F}} - \mathbb{P} - pJ\mathbb{F}^{-\intercal} - J\left(\nabla_0\cdot\boldsymbol{\xi}_s\right)\mathbb{F}^{-\intercal}\right):\dot{\mathbb{F}} \\
&+ \left(\frac{\partial\psi}{\partial\nabla_0 J} - \boldsymbol{\xi}_s\right)\cdot\nabla_0\dot{J} + \mathbf{W}_g\cdot\nabla_0\left(\rho_g\mu_g\right) + \mathbf{W}_l\cdot\nabla_0\left(\rho_l\mu_l\right) \leq 0.
\end{aligned} \tag{2.14}$$

Due to the mutual independence of the arguments of ψ, this inequality is only satisfied for all possible configurations if each of the bracketed terms vanishes independently (this reasoning is commonly referred to as the Coleman-Noll procedure). This requirement then leads to a set of thermodynamic constraints,

$$\rho_g\mu_g = p + \frac{\partial\psi}{\partial\varphi_g} - \nabla_0\cdot\frac{\partial\psi}{\partial\nabla_0\varphi_g}, \tag{2.15a}$$

$$\rho_l\mu_l = p + \frac{\partial\psi}{\partial\varphi_l} - \nabla_0\cdot\frac{\partial\psi}{\partial\nabla_0\varphi_l}, \tag{2.15b}$$

$$\frac{\partial\psi}{\partial d} - \nabla_0\cdot\frac{\partial\psi}{\partial\nabla_0 d} = 0, \tag{2.15c}$$

$$\mathbb{P} = -pJ\mathbb{F}^{-\intercal} + \frac{\partial\psi}{\partial\mathbb{F}} - J\left(\nabla_0\cdot\frac{\partial\psi}{\partial\nabla_0 J}\right)\mathbb{F}^{-\intercal}, \tag{2.15d}$$

and the additional requirement that

$$\mathbf{W}_g\cdot\nabla_0\left(\rho_g\mu_g\right) + \mathbf{W}_l\cdot\nabla_0\left(\rho_l\mu_l\right) \leq 0. \tag{2.16}$$

The latter expression can be satisfied by choosing an appropriate form for the fluxes $\mathbf{W}_g$ and $\mathbf{W}_l$, as discussed in §2.1.5 below. Note that Equations (2.15) do not represent a unique choice of constraints that satisfy Equation (2.14). Here, we choose the simplest possible set of constraints that are compatible with the assumption of a local thermodynamic equilibrium.

2.1.4 Free Energy

The evolution equations derived in §2.1.2 drive the system toward an equilibrium state defined by the minima of ψ. We must next construct a function ψ that captures the different physical processes at play in our system. We assume that ψ is, in general, an additive function of each physical contribution,

$$\psi = \psi_{\text{bulk}} + \psi_{\text{mix}} + \psi_{\text{elastic}} + \psi_{\text{damage}} + \psi_{\text{interface}}, \tag{2.17}$$

where ψ_{bulk}, ψ_{mix}, ψ_{elastic}, ψ_{damage} and $\psi_{\text{interface}}$ are the energetic contributions from changing the mass of gas or liquid in the material element, gas–liquid–solid interactions within the material element, elasticity of the solid skeleton, mechanical damage to the solid skeleton, and interfacial effects, respectively. We write these contributions in terms of the true volume fractions and their Eulerian gradients in order to provide greater physical insight; conversion to nominal quantities is straightforward. Recall that ψ has units of energy per reference volume; as such, the free energy functions below are weighted by J where appropriate.

The bulk free energy, ψ_{bulk}, is the free energy associated with the amount of gas and liquid in the material element and is given by

$$\psi_{\text{bulk}}\left(\phi_\alpha, J\right) = \left(\mu_l^0 \rho_l \phi_l + \mu_g^0 \rho_g \phi_g\right) J, \tag{2.18}$$

where the reference chemical potential μ_α^0 is the energy associated with adding one unit mass of fluid α to the material element, neglecting interactions between phases, and is constant with respect to composition. Note that for partially miscible and/or compressible systems, the form of ψ_{bulk} is much more complex [*e.g.*, Fu et al., 2017].

The mixing (interaction) energy, ψ_{mix}, depends on the pore-scale arrangement of the phases and on the wetting characteristics of the fluid–fluid–solid system. To construct a free energy that gives the desired phenomenological behaviour for our

system, we draw inspiration from Flory–Huggins theory used in polymer physics [Flory and Rehner, 1943]. In a polymer solution, the Flory–Huggins energy, ψ_{FH}, for a multiphase mixture is

$$\psi_{\mathrm{FH}} = k_B T J \left[\sum_{\alpha \neq s} \Omega_\alpha \phi_\alpha \log \phi_\alpha + \sum_{\alpha \neq \beta} \hat{\chi}_{\alpha\beta} \phi_\alpha \phi_\beta \right], \tag{2.19}$$

where k_B is the Boltzmann constant, T is temperature, Ω_α is inversely proportional to the characteristic volume of particles of phase α, and $\hat{\chi}_{\alpha\beta}$ characterises the strength of unfavourable interactions between phases α and β. The first sum in Equation (2.19) represents the entropy of mixing of the different phases. Due to the large size of solid grains compared to fluid molecules, it is assumed that $\Omega_s \ll \Omega_f$, where the subscript s indicates a general solid phase and f a general fluid phase, and so the contribution of solid to the entropy term is neglected. The entropy term promotes the mixing of different phases, and also constrains the relevant volume fractions to remain between zero and one. The second sum in Equation (2.19) represents the enthalpy of interactions between different phases, and results in the formation of the double-well potentials that promote phase separation. The Flory–Huggins free energy thus captures the key features we expect from gas–liquid–solid interactions in a granular system, namely a double-well structure in which volume fractions are constrained to remain between zero and one. As such, we use ψ_{FH} as motivation for constructing an appropriate form for ψ_{mix}.

In our system, the most important interaction is that the gas is non-wetting to the solid relative to the liquid. We enforce this requirement by assuming that gas–liquid and gas–solid interactions are much more energetically expensive than liquid–solid interactions, meaning that $\hat{\chi}_{ls} \ll \hat{\chi}_{gs,gl}$. We therefore neglect the liquid–solid interaction. In general, the remaining coefficients, $\hat{\chi}_{gs}$ and $\hat{\chi}_{gl}$, depend on physical quantities such as surface energies and pore structure; we take them to be constant material properties here. For simplicity, we further assume that $\Omega_g = \Omega_l = \Omega$. For reasons that will become clear later (*see §4.1*), we additionally

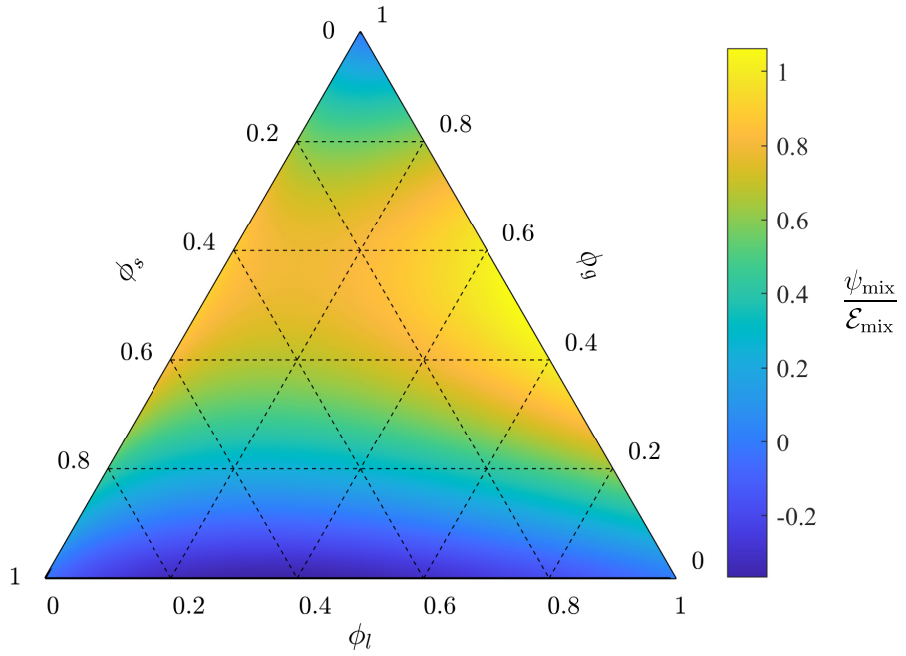

Figure 2.2: An example ternary plot of $\frac{\psi_{\text{mix}}}{\mathcal{E}_{\text{mix}}}$ (Equation 2.20) with local minima at $\phi_g = 1$ (gas cavities) and along $\phi_g = 0$ (liquid-saturated porous medium). For this figure, we set $\chi_{gs} = 5$, $\chi_{gl} = 7$ and $\chi_{gsl} = 6$.

include a ternary interaction term that represents the energetic cost of all three phases interacting with each other. The mixing energy is then given by

$$\psi_{\text{mix}}\left(\phi_\alpha, J\right) = \mathcal{E}_{\text{mix}}\left(\phi_g \log \phi_g + \phi_l \log \phi_l + \chi_{gs}\phi_g\phi_s + \chi_{gl}\phi_g\phi_l + \chi_{gsl}\phi_g\phi_s\phi_l\right) J, \tag{2.20}$$

where $\chi_{\alpha\beta} = \frac{\hat{\chi}_{\alpha\beta}}{\Omega}$, χ_{gsl} is the strength of the three-phase interaction, and $\mathcal{E}_{\text{mix}}$ is a characteristic energy density associated with mixing, which we treat as a material property, and into which we have absorbed Ω. Figure 2.2 shows a ternary plot of this interaction energy. The key feature of the energetic landscape is the presence of local minima near $\phi_g = 1$ and along $\phi_g = 0$, corresponding to open gas cavities and to a liquid-saturated porous matrix, respectively. The specific values of χ_{gs}, χ_{gl} and χ_{gsl} control the relative depths of these two minima, but not the overall structure of the energy landscape.

The elastic energy of the solid matrix due to deformation is given by ψ_{elastic}, and can be expressed in terms of a traditional strain-energy density function, $\mathcal{W}_{\text{el}}\left(\mathbb{F}\right)$.

For simplicity, we use a standard neo-Hookean strain-energy density,

$$\mathcal{W}_{\text{el}} = \frac{1}{2}G\left[\text{tr}\left(\mathbb{F}^{\intercal}\cdot\mathbb{F}\right) - 3 - 2\log J\right] + \frac{1}{2}\Lambda\left(\log J\right)^2, \tag{2.21}$$

where G and Λ are the 'drained' shear modulus and first Lamé parameter of the solid skeleton, respectively. Note that the derivation that follows is valid for any choice of $\mathcal{W}_{\text{el}}$.

A notable characteristic of a solid skeleton with a non-cohseive granular microstructure is that tension does not result in the storage of elastic energy, since grains only interact when in contact. To incorporate this feature of the mechanics, we define an additional order parameter, $d\left(\mathbf{x}, t\right)$, which we identify as a Bourdin-style damage parameter [Bourdin et al., 2008]. The damage parameter represents a phase-field approximation of the fractures to the solid skeleton that are caused by the opening of gas cavities. Locally, a value of $d = 0$ corresponds to an undamaged solid skeleton, in which the solid grains are in contact and hence provide a standard elastic response to compression. In contrast, a value of $d = 1$ corresponds to a fully damaged solid skeleton that provides no elastic resistance to further deformation. The use of a phase-field damage parameter ensures a smooth transition between open cavities and the rest of the porous medium

To implement damage, we assume that the strain-energy density can be decomposed into distinct tensile and compressive parts, denoted $\mathcal{W}^{+}$ and $\mathcal{W}^{-}$, respectively [Miehe et al., 2010b, Tang et al., 2019]. We demonstrate a suitable decomposition of $\mathcal{W}_{\text{el}}$ into tensile and compressive parts for a non-linear material in Appendix A.1, following the approach of Tang et al. [2019]. We can then assume that the tensile part of the elastic energy is degraded by d [Miehe et al., 2010b], such that,

$$\psi_{\text{elastic}}\left(d, \mathbb{F}, J\right) = g\left(d\right)\mathcal{W}^{+} + \mathcal{W}^{-}, \tag{2.22a}$$

$$g\left(d\right) = \left(1 - \Theta\right)\left(1 - d\right)^2 + \Theta, \tag{2.22b}$$

where $\Theta \ll 1$ is a numerical smoothing parameter. In the undamaged limit ($d = 0$), this formulation reduces to $\psi_{\text{elastic}} = \mathcal{W}^+ + \mathcal{W}^- = \mathcal{W}_{\text{el}}$, as expected.

According to Griffith's theory of fracture, the energy required to create a fracture in a material is given by the critical fracture energy, $\mathcal{G}_c$, integrated over the area of the fracture [Griffith, 1921], in the reference frame. In a granular medium, the 'fracture' energy is associated with the energy required to cause the decohesion of neighbouring solid grains. We approximate the energy required to form such fractures by a bulk energy, ψ_{damage}, of the form [Bourdin et al., 2008, Miehe et al., 2010b],

$$\psi_{\text{damage}}\left(d, \nabla_0 d\right) = \mathcal{G}_c \left(\frac{d^2}{4 l_d} + l_d |\nabla_0 d|^2 \right), \tag{2.23}$$

where l_d controls the width of the transition between damaged and undamaged material. We expect $\mathcal{G}_c$ to be very small for a non-cohesive solid skeleton, where the only resistance to fracture comes from wetting liquid bridges between solid grains. Note also that damage of a non-cohesive solid skeleton is reversible: if a cavity closes, d will return to zero and the skeleton will return to standard elastic behaviour.

Finally, $\psi_{\text{interface}}$ measures the energy of diffuse interfaces between different phases. In a phase-field formulation, interfaces are represented implicitly as regions with large gradients in composition or density. The interfacial energy for our system thus depends on gradients in volume fraction [Cahn and Hilliard, 1958, Hong and Wang, 2013] and the total interfacial energy is the sum of the energy of each of the possible types of interface [Kim and Lowengrub, 2005]. The simplest such dependence can be written

$$\Upsilon_{\text{int}} = \sum_{\alpha} \frac{\gamma_\alpha}{2} |\nabla \phi_\alpha|^2 J, \tag{2.24}$$

where γ_α are the associated interfacial coefficients. For a two-phase system (say, liquid and gas), the no-void condition allows elimination of one of the volume fractions (say, ϕ_g) such that $\Upsilon_{\text{int}} = \frac{\gamma}{2} |\nabla \phi_l|^2 J$, where $\gamma = \gamma_l + \gamma_g$, and γ can

be directly related to the surface energy of the sharp interface formed between these two phases [Caginalp, 1989]. For our three-phase system, we use the no-void condition to eliminate ϕ_s and write the total interfacial energy solely in terms of the gas and liquid fractions,

$$\psi_{\text{interface}}\left(J, \nabla\phi_\alpha\right) = \frac{\gamma_1}{2}|\nabla\phi_g|^2 J + \frac{\gamma_2}{2}|\nabla\phi_l|^2 J + \frac{\gamma_3}{2}\left(\nabla\phi_g \cdot \nabla\phi_l\right) J, \tag{2.25}$$

where $\gamma_1 = \gamma_g + \gamma_s$, $\gamma_2 = \gamma_l + \gamma_s$ and $\gamma_3 = 2\gamma_s$. Unlike for a two-phase system, the relationship between these quantities and the associated surface energies is not clear.

2.1.5 Constitutive Behaviour

The free energy constructed in §2.1.4 can now be combined with the thermodynamic constraints resulting from the energy inequality (Equations 2.15) to find expressions for the constitutive behaviour of the system in terms of the different driving mechanisms. We use Equations (2.15a) and (2.15b) to decompose the chemical potential for the gas and liquid phases into the sum of the pressure and a capillary potential, Ψ_α,

$$\rho_\alpha \mu_\alpha = p + \Psi_\alpha, \tag{2.26a}$$

$$\Psi_\alpha = \frac{\partial\psi}{\partial\varphi_\alpha} - \nabla_0 \cdot \left(\frac{\partial\psi}{\partial\nabla_0\varphi_\alpha}\right) \equiv \frac{\delta\psi}{\delta\varphi_\alpha}. \tag{2.26b}$$

The capillary potentials represent the thermodynamic forcing on the gas and liquid phases due to the interactions between them. Note that Ψ_α can be viewed as the variational derivative of ψ with respect to φ_α.

Equation (2.15c) leads to an elliptic equation for d as a function of the tensile elastic energy. For our specified free energy, the result is

$$4l_d\left(1-\Theta\right)\left(1-d\right)\mathcal{W}^+ + 4\mathcal{G}_c l_d^2 \nabla_0^2 d = \mathcal{G}_c d. \tag{2.27}$$

In the limit $\mathcal{G}_c \to 0$ (no energetic resistance to decohesion), Equation (2.27) reduces to $\mathcal{W}^+ (1 - d) = 0$, such that any non-zero tension results in immediate fracture of the solid skeleton. This case essentially reproduces the sharp-interface limit of open cavities within a poroelastic continuum.

Equation (2.15d) allows the total stress to be decomposed into three distinct parts, converting from the first Piola-Kirchhoff stress to the Cauchy stress to arrive at

$$\mathbb{T} = -p\mathbb{I} + \boldsymbol{\sigma}' + \mathbb{K}. \tag{2.28}$$

The effective (elastic) stress, $\boldsymbol{\sigma}'$, is

$$\boldsymbol{\sigma}' = \frac{1}{J}\frac{\partial \psi_{\text{elastic}}}{\partial \mathbb{F}} \cdot \mathbb{F}^{\intercal} = g(d)\,\frac{1}{J}\frac{\partial \mathcal{W}^+}{\partial \mathbb{F}} \cdot \mathbb{F}^{\intercal} + \frac{1}{J}\frac{\partial \mathcal{W}^-}{\partial \mathbb{F}} \cdot \mathbb{F}^{\intercal}, \tag{2.29}$$

where we have used ψ_{elastic} from §2.1.4 and $g(d)$ is the degradation function defined in Equation (2.22b). The Korteweg stress is

$$\mathbb{K} = \frac{1}{J}\frac{\partial \psi_{\text{interface}}}{\partial \mathbb{F}} \cdot \mathbb{F}^{\intercal} - \left(\nabla_0 \cdot \frac{\partial \psi_{\text{interface}}}{\partial \nabla_0 J}\right)\mathbb{I}. \tag{2.30}$$

The Korteweg stress is the bulk representation of interfacial tension at diffuse, internal interfaces and thus resists gradients in composition. The stress balance derived in Equation (2.9) allows us to link the effective and Korteweg stresses with gradients in the chemical potential via the pressure field.

Recall that Equation (2.16) constrains the relationship between fluid chemical potentials and fluxes. The simplest way to satisfy this constraint is for the fluxes to be proportional to gradients in chemical potential, such that,

$$\mathbf{W}_\alpha = -\mathbb{M}_\alpha \nabla_0 (\rho_\alpha \mu_\alpha), \tag{2.31}$$

where $\mathbb{M}_\alpha(\varphi_\alpha, \mathbb{F})$ is a positive-definite mobility tensor. The associated Eulerian volume fluxes are given by

$$\mathbf{w}_\alpha = -\mathcal{M}_\alpha \nabla(\rho_\alpha \mu_\alpha), \tag{2.32}$$

where $\mathcal{M}_\alpha(\phi_\alpha)$ is the Eulerian mobility of fluid α. In the Eulerian frame, the pore space of granular packings is typically fairly isotropic, so we assume a scalar mobility for simplicity. At the least, $\mathcal{M}_\alpha$ must be a linear function of the fluid volume fraction, so that if there is no fluid present, then there will be no associated flux. In the interest of developing a relatively simple model that captures the leading-order behaviour of the system, we choose $\mathcal{M}_\alpha = \phi_\alpha \mathcal{M}_\alpha^0$, where $\mathcal{M}_\alpha^0$ is a constant for fluid α within a particular porous medium; however, more complicated mobility laws could also be used. For example, $\mathcal{M}_\alpha$ could be decomposed into a product of viscosity, absolute permeability, and relative permeability, so as to resemble Darcy's law for multiphase porous media flow neglecting the effect of gravity. These relations between the fluid fluxes and their respective chemical potentials complete our model.

Explicit expressions for the effective stress, the capillary potential and the Korteweg stress for the particular form of the free energy specified in §2.1.4 are given in Appendices A.1, A.2 and A.3, respectively. A full set of governing equations is presented in Appendix A.4.

2.1.6 Reduction to 1D

For uniaxial flow and deformation, the model derived above can be reduced to one dimension. Although uniaxial behaviour is a strong constraint, studying such a system is significantly easier, both conceptually and computationally, and allows us to gain substantial insight into what is ultimately a complex model. Uniaxial

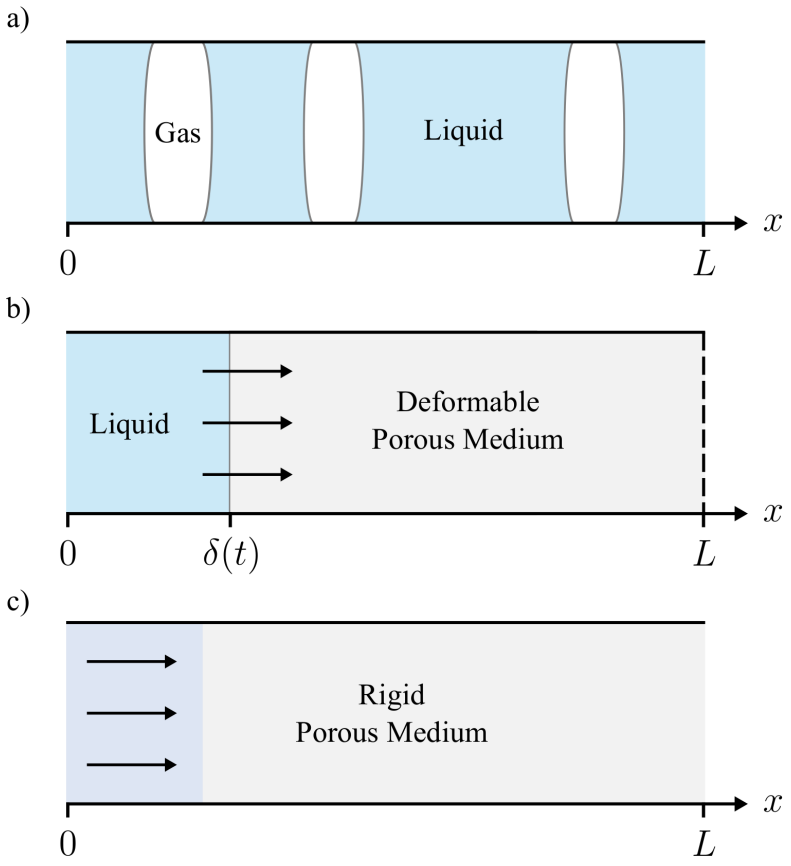

Figure 2.3: A schematic showing the uniaxial (1D) set up for each of the three test problems considered below: (a) the phase separation of gas and liquid in the absence of a solid skeleton in a periodic domain, (b) the deformation of a saturated porous medium via an applied liquid through-flow in the absence of gas, and (c) forced imbibition of liquid into a rigid porous medium, displacing gas. All flow and deformation take place in the x-direction.

behaviour implies that

$$\mathbf{v}_\alpha = v_\alpha\left(x,t\right)\hat{\mathbf{e}}_x, \tag{2.33a}$$

$$\mathbf{u}_s = u_s\left(x,t\right)\hat{\mathbf{e}}_x, \tag{2.33b}$$

$$\phi_\alpha = \phi_\alpha\left(x,t\right), \tag{2.33c}$$

$$d = d\left(x,t\right), \tag{2.33d}$$

as illustrated in Figure 2.3.

At this point, it is convenient to non-dimensionalise our model. We do so using the following scalings: $x = L\tilde{x}$, $q = q_0\tilde{q}$, and $t = \mathcal{T}_{\text{cap}}\tilde{t}$, where L is a characteristic length scale, q_0 is the mixture flux at the boundary, and $\mathcal{T}_{\text{cap}} = \frac{L^2}{\mathcal{M}_l^0\mathcal{E}_{\text{mix}}}$ is the

time scale associated with the transport of liquid across a distance L by capillary effects. This scaling motivates us to introduce the following dimensionless groups, which characterise the relative strengths of the different physical processes at play:

$$Q_0 = \frac{q_0 \mathcal{T}_{\text{cap}}}{L}, \quad \mathcal{M}_r = \frac{\mathcal{M}_g^0}{\mathcal{M}_l^0}, \quad \mathcal{D} = \frac{\mathcal{E}_{\text{mix}}}{G}, \quad \Gamma_i = \frac{\gamma_i}{\mathcal{E}_{\text{mix}} L^2}, \quad \kappa_c = \frac{\mathcal{G}_c}{\mathcal{E}_{\text{mix}} l_d}, \quad \mathcal{L}_d = \frac{l_d^2}{L^2}.$$

The strength of background fluid flow relative to capillary forces is measured by Q_0, while $\mathcal{M}_r$ is the ratio of gas mobility to liquid mobility, $\mathcal{D}$ is the characteristic 'deformability' of the solid, Γ_i $(i = 1, 2, 3)$ are the rescaled interfacial coefficients, κ_c is the strength of cohesion between solid grains, and $\mathcal{L}_d$ characterises the sharpness of the transition between damaged and undamaged material. We work exclusively with dimensionless quantities going forward, dropping the tildes for convenience.

In 1D, Equation (2.7c), which enforces the incompressibility of the mixture, simplifies to

$$\frac{\partial q}{\partial x} = 0. \tag{2.34}$$

For the scalings defined above, the non-dimensional boundary condition for the flux is $q\,(0, t) = Q_0$ and the solution to Equation (2.34) is therefore $q = Q_0$. For uniaxial flow and deformation, the deformation gradient tensor, $\mathbb{F}$, is diagonal, which greatly simplifies the stresses: only the xx-components of $\boldsymbol{\sigma}'$ and $\mathbb{K}$, denoted σ'_{xx} and K_{xx}, respectively, appear explicitly in the 1D model. We use momentum conservation (Equation 2.9) and the stress decomposition (Equation 2.28) to link p with σ'_{xx} and K_{xx}:

$$\frac{\partial p}{\partial x} = \frac{\partial}{\partial x}\left(\sigma'_{xx} + K_{xx}\right). \tag{2.35}$$

We now replace the fluid fluxes in the 1D evolution equation for ϕ_g, given by Equation (2.7a), with the constitutive behaviour outlined above in Equations (2.26)

and (2.32). The gas fraction then evolves according to

$$\begin{aligned}\frac{\partial \phi_g}{\partial t} = -Q_0 \frac{\partial \phi_g}{\partial x} + \mathcal{M}_r \frac{\partial}{\partial x}\left[(1-\phi_g)\,\phi_g \frac{\partial}{\partial x}\left(\Psi_g + \sigma'_{xx} + K_{xx}\right)\right] \\ -\frac{\partial}{\partial x}\left[\phi_g\,(\phi-\phi_g)\,\frac{\partial}{\partial x}\left(\Psi_l + \sigma'_{xx} + K_{xx}\right)\right],\end{aligned} \tag{2.36}$$

where Ψ_α is now the dimensionless capillary potential, which is specified below. Similarly, we combine the 1D evolution equation for ϕ (Equation 2.7b) with the relevant constitutive behaviour to arrive at

$$\begin{aligned}\frac{\partial \phi}{\partial t} = -Q_0 \frac{\partial \phi}{\partial x} + \mathcal{M}_r \frac{\partial}{\partial x}\left[(1-\phi)\,\phi_g \frac{\partial}{\partial x}\left(\Psi_g + \sigma'_{xx} + K_{xx}\right)\right] \\ +\frac{\partial}{\partial x}\left[(1-\phi)\,(\phi-\phi_g)\,\frac{\partial}{\partial x}\left(\Psi_l + \sigma'_{xx} + K_{xx}\right)\right].\end{aligned} \tag{2.37}$$

We close our model with the 1D version of Equation (2.27), which describes the distribution of damage,

$$4\,(1-\Theta)\,(1-d)\,\mathcal{W}^+ + 4\kappa_c \mathcal{L}_d \frac{\partial^2 d}{\partial X^2} = \kappa_c d, \tag{2.38}$$

where $\mathcal{W}^+$ is the dimensionless tensile energy, which in 1D is solely a function of ϕ. The model is thus reduced to two non-linear evolution equations (for ϕ_g and for ϕ) and one elliptic equation (for d).

By non-dimensionalising the capillary potentials (Equation 2.26b) and undertaking the required differentiation (Appendix A.2), we find that

$$\Psi_g = \Pi_g - \Gamma_1 \frac{\partial^2 \phi_g}{\partial x^2} - \frac{\Gamma_3}{2}\frac{\partial^2 \phi_l}{\partial x^2}, \tag{2.39a}$$

$$\Psi_l = \Pi_l - \Gamma_2 \frac{\partial^2 \phi_l}{\partial x^2} - \frac{\Gamma_3}{2}\frac{\partial^2 \phi_g}{\partial x^2}, \tag{2.39b}$$

where the interaction potentials, Π_g and Π_l, are

$$\Pi_g = \log \phi_g + \phi_s + (1-\phi_g)\,(\chi_{gl}\phi_l + \chi_{gs}\phi_s) + \chi_{gsl}\phi_s\phi_l(1-2\phi_g) \tag{2.40a}$$

and

$$\Pi_l = \log \phi_l + \phi_s + \phi_g \left[\chi_{gl}(1-\phi_l) - \chi_{gs}\phi_s\right] + \chi_{gsl}\phi_g\phi_s(1-2\phi_l). \tag{2.40b}$$

The interaction potentials result from the thermodynamic interactions between the phases, as described by ψ_{mix}, and are the drivers for phase separation.

For uniaxial deformation, tension can be defined solely volumetrically: the material is in tension if $J > 1$ and in compression if $J \leq 1$. The non-dimensional effective stress (Equation 2.29) thus reduces to

$$\sigma'_{xx} = \begin{cases} \sigma'_0(\phi) & J \leq 1, \\ \sigma'_0(\phi)\, g(d) & J > 1, \end{cases} \tag{2.41}$$

where σ'_0 is the undamaged neo-Hookean stress given by

$$\sigma'_0 = \frac{1}{\mathcal{D}}\left[J - \frac{1}{J} + \varsigma\frac{\log J}{J}\right], \tag{2.42}$$

and $\varsigma = \frac{\Lambda}{G}$. The derivation of this effective stress is provided in Appendix A.1. Similarly, the tensile energy used in Equation (2.38) is given by,

$$\mathcal{W}^+ = \begin{cases} 0 & \text{for } J \leq 1, \\ \mathcal{W}^0_{el} & \text{for } J > 1, \end{cases} \tag{2.43}$$

where $\mathcal{W}^0_{el} = \frac{1}{2\mathcal{D}}\left[J^2 - 1 - 2\log J + \varsigma(\log J)^2\right]$. The incompressibility condition (Equation 2.4) links J to ϕ:

$$J = \frac{1-\phi_0}{1-\phi}. \tag{2.44}$$

Finally, K_{xx} is derived in Appendix A.3 and is given by

$$K_{xx} = \Gamma_1 \left[\phi_g \frac{\partial^2 \phi_g}{\partial x^2} - \frac{1}{2} \left(\frac{\partial \phi_g}{\partial x} \right)^2 \right] + \Gamma_2 \left[\phi_l \frac{\partial^2 \phi_l}{\partial x^2} - \frac{1}{2} \left(\frac{\partial \phi_l}{\partial x} \right)^2 \right] + \frac{1}{2} \Gamma_3 \left[\phi_g \frac{\partial^2 \phi_l}{\partial x^2} + \phi_l \frac{\partial^2 \phi_g}{\partial x^2} - \frac{\partial \phi_l}{\partial x} \frac{\partial \phi_g}{\partial x} \right]. \tag{2.45}$$

Equations (2.36)–(2.45) comprise a complete model for our system in 1D, and can be solved numerically given appropriate initial and boundary conditions. In the results below, we do so by discretising in space using finite differences on a uniform staggered grid, with fluxes evaluated on cell edges, and order parameters on cell centres. We use central first-order and second-order finite difference schemes for first-order and second-order spatial derivatives, respectively. We typically use $N = 500$ grid points. We integrate in time using MATLAB's in-built solver for stiff differential equations, `ode15s`.

2.2 Model Simplifications

Our full three-phase model captures several different physical effects, and ultimately consists of modelling fluid–fluid phase separation within the framework of large-deformation poroelasticity. To gain insight into the behaviour of our model, we begin by considering two limiting cases involving two-phase mixtures: a gas–liquid system (no solid) and a liquid–solid system (no gas). In addition, we consider the limiting case of a rigid solid skeleton (no deformation). These limiting cases are comparatively well understood, allowing us to benchmark the predictions of our model against previous results.

2.2.1 Gas–Liquid System (no solid)

In the no-solid limit, $\phi \equiv \phi_0 \equiv 1$, our model reduces to a gas–liquid system in which the two phases interact in an unconstrained domain (no porous medium),

as illustrated in Figure 2.3a. This scenario is typically described by the Cahn–Hilliard equation for binary mixtures [Cahn and Hilliard, 1958]. In this limit, the evolution equation for the porosity (Equation 2.37) and the elliptic equation for damage (Equation 2.38) are degenerate. The evolution equation for the gas fraction (Equation 2.36) simplifies greatly, most notably due to disappearance of the elastic terms, becoming

$$\frac{\partial \phi_g}{\partial t} - \mathcal{M}_r \frac{\partial}{\partial x}\left[\phi_g \frac{\partial \mu_g}{\partial x}\right] = 0, \tag{2.46}$$

where the chemical potential of the gas is now given by

$$\mu_g = \log \phi_g + \chi_{gl}\left(1-\phi_g\right)^2 - \Gamma\left[\frac{1}{2}\left(\frac{\partial \phi_g}{\partial x}\right)^2 + \left(1-\phi_g\right)\frac{\partial^2 \phi_g}{\partial x^2}\right], \tag{2.47}$$

with $\Gamma = \Gamma_1 + \Gamma_2 - \Gamma_3 = \Gamma_g + \Gamma_l$ the characteristic interfacial coefficient between the fluid phases. Equations (2.46) and (2.47) resemble the standard Cahn–Hilliard equation for fluid–fluid phase separation [*e.g.*, Fu et al., 2016] but, in our case, also account for the mechanical stress generated across diffuse interfaces.

We now consider a test problem with periodic boundary conditions. For the initial condition, we use a homogeneous gas fraction superimposed with small, random perturbations. The subsequent evolution is standard fluid–fluid phase separation via spinodal decomposition, in which the mixture separates spontaneously into distinct gas-rich and liquid-rich domains separated by diffuse interfaces (Figure 2.4). Over time, these domains coarsen as smaller gas 'bubbles' merge with larger gas 'bubbles'. Coarsening is driven by the evolution of the system towards minimum global energy (the smaller the number of bubbles, the smaller the total interfacial energy). In 1D, coarsening is very slow [Sun and Ward, 2000]; as such, we stop our simulations before reaching the eventual equilibrium of a single bubble.

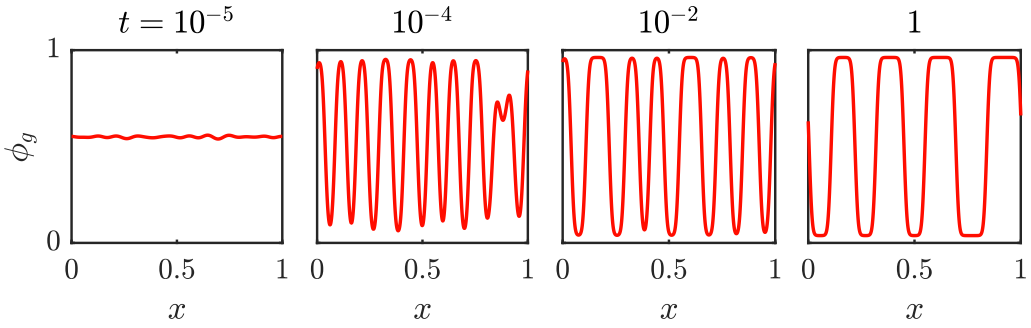

Figure 2.4: Gas–liquid phase separation via the numerical solution of Equations (2.46) and (2.47) subject to periodic boundary conditions. An initially nearly homogeneous mixture undergoes the classical spinodal decomposition and subsequent coarsening characteristic of Cahn–Hilliard-type problems. Parameter values are $\mathcal{M}_r = 50$, $\chi_{gl} = 3.5$, and $\Gamma = 0.0002$. The initial gas fraction is 0.55 with a random perturbation of size 0.01. The simulations were stopped before reaching the final equilibrium due to the slow rate of coarsening in 1D.

2.2.2 Liquid–Solid System (no gas)

In the no-gas limit, our model reduces to a diffuse-interface formulation of the well-known theory of single-phase large-deformation poroelasticity [Biot, 1972, Coussy, 2004]. In this case, there will be no thermodynamically driven phase separation because there is minimal energetic cost to liquid remaining within the pore space of the solid skeleton. However, flow can still drive phase separation, as demonstrated below. Setting $\phi_g \equiv 0$, Equation (2.36) for the evolution of the gas fraction degenerates and Equation (2.37) for the evolution of the porosity simplifies to

$$\frac{\partial \phi}{\partial t} + Q_0 \frac{\partial \phi}{\partial x} - \frac{\partial}{\partial x}\left[(1-\phi)\,\mathcal{M}(\phi)\,\frac{\partial}{\partial x}\left(\sigma'_{xx} + \Psi\right)\right] = 0, \tag{2.48}$$

with

$$\Psi = \log\phi + 1 - \phi - \Gamma_2\left[(1-\phi)\,\frac{\partial^2 \phi}{\partial x^2} + \frac{1}{2}\left(\frac{\partial \phi}{\partial x}\right)^2\right], \tag{2.49}$$

and a dimensionless mobility given by $\mathcal{M}(\phi) = \phi$. This equation is reminiscent of standard sharp-interface poroelasticity [*e.g.*, MacMinn et al., 2016], but with the addition of a potential, Ψ, that allows the formation of internal diffuse interfaces, such as those resulting from the fluid-driven opening of solid-free cavities within the

porous skeleton. The effective stress here also depends on d via Equation (2.38).

For a quantitative comparison of our model with sharp-interface poroelasticity, we consider the uniaxial deformation of a packing of soft grains due to net liquid through-flow from left to right (Figure 2.3b). We impose a constant liquid influx at the left boundary of non-dimensional flow rate Q_0. We take the right boundary to be permeable, allowing free outflow of the liquid but not of the solid. The result is that the packing will be compressed in the direction of the flow, with the left edge acting as an internal free boundary that moves downstream away from its initial position. Traditionally, this problem would be approached by solving the equations of large-deformation poroelasticity within the packing while explicitly tracking the position of the left edge of the packing as a moving boundary, assuming that the effective stress vanishes there. In our model, the left edge of the packing is an internal diffuse interface between a solid-free cavity ($\phi \approx 1$) and a porous domain ($0 < \phi < 1$).

For this problem, the traditional sharp-interface formulation can be solved analytically at steady state, thus allowing for direct comparison with our phase-field approach. Following MacMinn et al. [2016], we define the left edge of the packing to have a position $\delta(t)$, with a fluid-filled domain for $x < \delta$. The porosity in the domain $x \in [\delta(t), 1]$ then evolves according to

$$\frac{\partial \phi}{\partial t} + Q_0 \frac{\partial \phi}{\partial x} - \frac{\partial}{\partial x}\left[(1-\phi)\,\mathcal{M}(\phi)\,\frac{\partial \sigma_0'}{\partial x}\right] = 0. \tag{2.50}$$

Conservation of mass requires that the influx of liquid at the left boundary, $x = \delta$, must match the outflux at the right boundary, $x = 1$. We use this fact, along with the requirement that the solid velocity vanishes at $x = 1$, to enforce that the relative liquid flux at the right boundary is equal to the total mixture flux, $w_l = -\mathcal{M}\frac{\partial \sigma_0'}{\partial x} = Q_0$. We also assume that the solid is relaxed at its left edge, so that the effective stress vanishes at $x = \delta$. The boundary conditions for Equation (2.50)

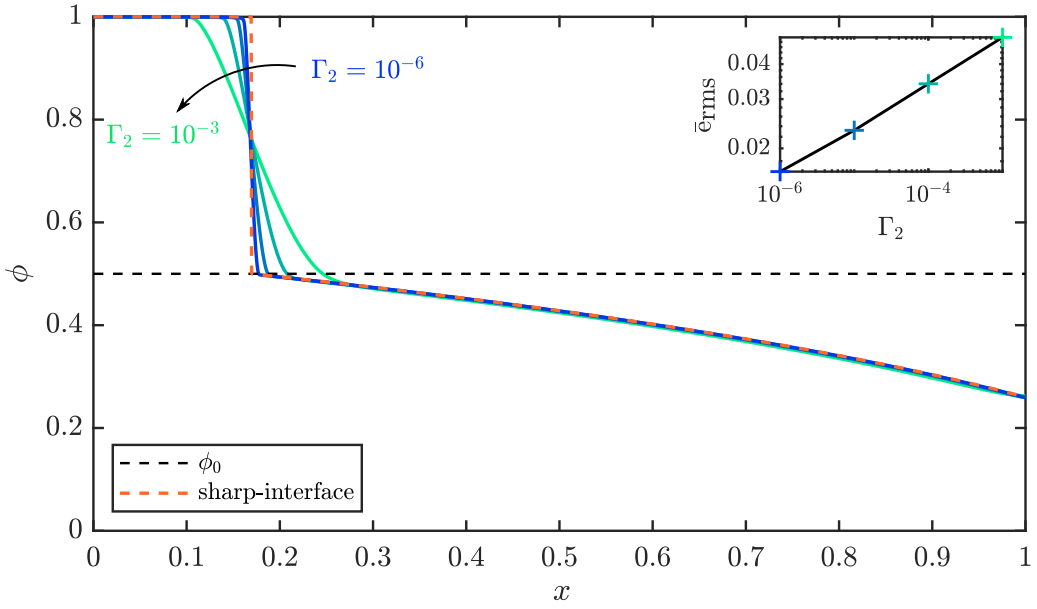

Figure 2.5: Fluid-driven deformation of a poroelastic medium at steady state from the traditional sharp-interface model (analytical solution, Equation 2.52) and from our phase-field formulation (numerical solutions to Equation 2.48) for $\Gamma_2 = 10^{-6}$, 10^{-5}, 10^{-4} and 10^{-3} (blue to green). The phase-field results approach the sharp-interface result as Γ_2 decreases. Here, we take $\phi_0 = 0.5$, $Q_0 = 0.2$, $\mathcal{D} = 2$, $\varsigma = 0.1$, $\kappa_c = 10^{-8}$ and $\mathcal{L}_d = 0.1\Gamma_2$. The inset shows the variation of root-mean-square (RMS) difference, $\bar{e}_{rms}$, between the sharp-interface and phase-field solutions with Γ_2.

are then given by

$$\sigma_0'(x=\delta) = 0 \quad \text{and} \quad \phi \frac{\partial \sigma_0'}{\partial x}\Big|_{x=1} = -Q_0. \tag{2.51}$$

As noted above, the steady-state porosity is piecewise:

$$\phi(x) = \begin{cases} 1 & x < \delta, \\ f(x) & \delta \leq x \leq 1. \end{cases} \tag{2.52}$$

Solving Equation (2.50) subject to the boundary conditions above (Equations 2.51) gives $f(x)$. An analytical solution for $f(x)$ is derived in Appendix B and plotted in Figure 2.5. We anticipate that our phase-field model would reduce to this formulation in the sharp-interface limit $\Gamma_2 \to 0$.

To compare our phase-field model to this sharp-interface result, we solve Equations (2.38) and Equation (2.48) numerically until reaching steady state. With regard to boundary conditions for these equations, we assume that the solid velocity vanishes at both ends of the domain, so that the relative liquid flux, w_l, is equal to Q_0 at $x = 0$ and $x = 1$. To enforce the fact that the solution should not depend on anything exterior to the domain, we also impose that the gradients of porosity and damage vanish at both ends. The boundary conditions for Equation (2.48) are thus

$$w_l\left(x = 0, 1\right) = Q_0, \quad \left.\frac{\partial \phi}{\partial x}\right|_{x=0,1} = 0 \quad \text{and} \quad \left.\frac{\partial d}{\partial x}\right|_{x=0,1} = 0. \tag{2.53}$$

With these boundary conditions, we solve Equations (2.38) and (2.48) numerically with initial condition $\phi\left(x, 0\right) = \phi_0$.

Figure 2.5 compares the steady state of the phase-field simulations for various values of Γ_2 (solid lines) with the analytical solution to the sharp-interface model given in Appendix B (orange dashed line). In both cases, the solution comprises a solid-free region at the left and a compressed porous packing at the right. Within the latter, the porosity is non-linear with position. Away from the interface, the two solutions are in excellent qualitative and quantitative agreement. Near the interface, the discontinuity in the sharp-interface solution is approximated by a smooth interpolation in the phase-field model, the width of which is controlled by Γ_2. As Γ_2 decreases, the phase-field solution converges towards the sharp-interface solution (Figure 2.5, inset).

2.2.3 Rigid System (no deformation)

In the limit of a rigid solid skeleton, our model describes two-phase flow through a rigid porous medium, a process which is commonly described by the Buckley–Leverett equation [Buckley and Leverett, 1942]. In this case, there is no deformation and the porosity is fixed such that $\phi = \phi_0$. As a result, there is no longer a distinction between the current and reference coordinate systems. It is convenient

to rewrite our evolution equations in terms of gas and liquid saturation, denoted $S_g = \frac{\phi_g}{\phi}$ and $S_l = \frac{\phi_l}{\phi} = 1 - S_g$, respectively. Equation (2.36) is then an evolution equation for S_g,

$$\frac{\partial S_g}{\partial t} + Q_0 \frac{\partial S_g}{\partial x} + \frac{\partial}{\partial x}\left[(1 - S_g)\, w_g - S_g w_l\right] = 0, \tag{2.54}$$

where w_g and w_l are the respective gas and liquid fluxes, given by

$$w_g = -\mathcal{M}_r \phi S_g \frac{\partial}{\partial x}\left[\log S_g + \chi'(1 - S_g) - \Gamma' \frac{\partial^2 S_g}{\partial x^2}\right] \tag{2.55}$$

and

$$w_l = -\phi(1 - S_g) \frac{\partial}{\partial x}\left[\log\left(1 - S_g\right) + \chi' S_g + \Gamma' \frac{\partial^2 S_g}{\partial x^2}\right]. \tag{2.56}$$

We define $\Gamma' = \phi\Gamma = \phi\left(\Gamma_g + \Gamma_l\right)$ and $\chi' = \phi\left[\chi_{gl} + \chi_{gsl}\left(1 - \phi\right)\right]$ as a rescaled interfacial coefficient and interaction parameter, respectively. Equations (2.37) and (2.38) for the porosity and damage degenerate in the rigid limit and liquid saturation is determined by the no-void condition, $S_g + S_l = 1$. Although the degeneracy of the evolution equation for porosity is not obvious from Equation (2.37), this result is made clear by setting $\phi_s = 1 - \phi_0$ and $\mathbf{v}_s = 0$ in Equation (2.5). In this limit, our model equations have the same structure as the phase-field formulation of unsaturated flow previously derived by Cueto-Felgueroso and Juanes [2008, 2009]. To relate our approach to classical models of two-phase flow through a rigid porous medium, the fluid mobility, $\mathcal{M}_\alpha$, can be decomposed into a product of absolute permeability P_0, relative permeability $P_{\alpha r}$ and fluid viscosity η_α, such that $\mathcal{M} = \frac{P_0 P_{\alpha r}}{\eta_\alpha}$. The specific form of mobility used here is equivalent to setting $P_0 = \phi\tilde{P}_0$ and $P_{\alpha r} = S_\alpha \tilde{P}_{\alpha r}$, where $\tilde{P}_0$ and $\tilde{P}_{\alpha r}$ are dimensionless constants which are subsumed into $\mathcal{M}_r$.

To test this limit of our model, we consider the injection of liquid into an otherwise dry (gas-saturated) porous medium (imbibition). We impose a liquid flux Q_0 at the left boundary (Figure 2.3c), and additionally enforce that $\frac{\partial S_g}{\partial x} = 0$ at both

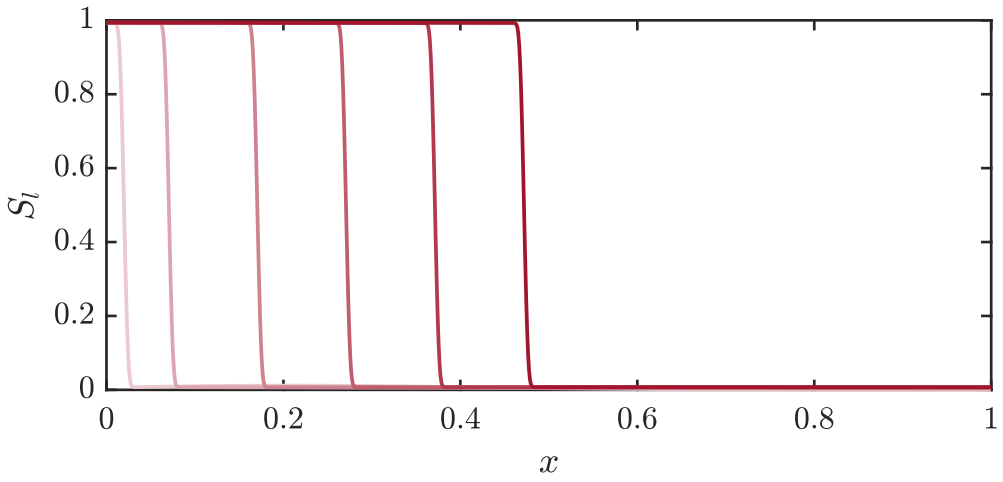

Figure 2.6: Numerical simulation showing liquid injection into a rigid, gas-saturated porous medium. Light to dark colours show simulation results at times $t = 0.05$, 0.15, 0.35, 0.55, 0.75 and 0.95. Parameter values are $\phi = 0.5$, $Q_0 = 0.5$, $\mathcal{M}_r = 2$, $\Gamma' = 0.0001$ and $\chi' = 5$. Simulation results for later times show the liquid front continue to propagate to the right until the entire domain is completely liquid-saturated.

the left and right boundaries ($x = 0, 1$), and that $\frac{\partial^2 S_g}{\partial x^2}$ at $x = 1$. We then solve Equation (2.54) numerically with initial condition $S_l(x, 0) = 10^{-4}$ to simulate an initially dry porous medium. Figure 2.6 shows the result of this simulation. We find that the injected liquid propagates from left to right in the form of a travelling wave, with a diffuse interface connecting the liquid-saturated and gas-saturated regions. The width of the diffuse interface is determined by the size of Γ'. Eventually, the liquid front reaches the right side of the domain, resulting in a completely liquid-saturated system. In the simulation shown here, the liquid saturation in the invaded region is very close to one. We find that the value of S_l in this region can be tuned by varying χ'. We obtain similar results for the injection of gas into an otherwise liquid-saturated porous medium (drainage), with χ' now controlling the amount of residual liquid left by this displacement process.

2.3 Summary

In this chapter, we derive a thermodynamically consistent phase-field model that describes the formation of non-wetting cavities within a soft porous medium as a result of phase separation. A key component of this model is the development of a phenomenological free energy that captures the competing effects of gas–liquid–solid (capillary) interactions, non-linear elasticity and fracture resistance of the solid skeleton, and interfacial stresses between different phases. We assumed simple constitutive relations, including a Darcy-like relationship for fluid fluxes and linear fluid mobilities, but our model generalises readily to other constitutive choices.

We have explored the behaviour of our model in various simplified forms in 1D. In the limiting cases of no-solid, no-gas and no-deformation, our model reproduces the expected behaviour for these well-studied systems. When no solid is present, we reproduce the fluid–fluid phase separation and coarsening behaviour characteristic of the Cahn–Hilliard equation. When no gas is present, our model matches well with analytic solutions to traditional sharp-interface Biot poroelasticity. Finally, when there is no deformation of the solid skeleton, our model displays the expected behaviour for two-phase flow in a rigid porous medium.

Chapter 3

Cavity Formation

The numerical simulations and linear stability analysis presented in this chapter constitute an extension to and reformatting of the work published in Paulin et al. [2022].

We now turn to the full three-phase behaviour of our model by considering a relevant test problem: the spontaneous formation of open gas cavities in a soft porous medium. We consider the evolution of an initially global (and homogeneous) gas distribution within the pore space, and identify the conditions under which cavity formation occurs. This scenario mimics various natural systems, such as a sea bed or peatland, in which biological and/or chemical processes produce gas bubbles throughout the otherwise undeformed and liquid-saturated pore space. A similar situation can be achieved experimentally by saturating a porous packing with a fluid containing dissolved gas. Triggering gas exsolution via either thermal quench [Style et al., 2018] or sudden depressurisation [Terzariol et al., 2021] then leads to the formation and growth of gas bubbles. As bubbles grow, they may collect together within the pore space, forming a phase-separated pore-invasive state (Figure 1.2b), which we refer to as a 'pore-bubble', or they may separate from the pore space entirely by opening gas-rich, solid-free cavities (Figure 1.2c).

In §3.1, we conduct numerical simulations of our three-phase model to investigate the dynamics of cavity formation. In §3.2, we conduct a linear stability analysis to help identify the key parameters controlling the onset of phase separation and the conditions under which cavity formation can occur. We use both numerical simulation and linear stability analysis to characterise the typical size of cavities. Finally, in §3.3, we study a reduced version of our model, informed by the results of our numerical simulations. We use this reduced model to find the equilibrium states of our system and to construct corresponding regime diagrams.

3.1 Numerical Simulations

We begin by conducting numerical simulations of Equations (2.36)–(2.45) to study spontaneous cavity formation. To focus on a porous medium that is sufficiently large that boundary effects are negligible in the bulk of the system, we impose periodic boundary conditions at $x = 0$ and $x = 1$. We also set $Q_0 = 0$ without loss of generality; a non-zero value of Q_0 corresponds to bulk translation. For initial conditions, we set

$$\phi_g(x, 0) = S_0\phi_0 + \nu(x), \tag{3.1}$$

$$\phi(x, 0) = \phi_0 - |\phi^*|, \tag{3.2}$$

where S_0 is the initial gas saturation, ν is a field of small, random fluctuations, and $\phi^* \ll 1$ ensures an initial state of slight compression so that the material is initially undamaged. A perfectly homogeneous initial state ($\nu = 0$) is an unstable equilibrium solution to our equations. Setting ν to be non-zero provides a small amount of noise so that instabilities are able to grow. We set ν by constructing a sum of a large number of sinusoids, whose relative phase and amplitude are chosen from a uniform distribution of random numbers.

Figure 3.1 shows an example simulation of cavity formation. Evolving the system from the initial state, we see that perturbations in the gas fraction grow over time, deforming the solid skeleton. As gas bubbles outgrow the available pore space, they expand to form cavities in the solid by displacing solid grains. As the cavities form and then grow, the rest of the solid skeleton is increasingly compressed into a smaller region. A local equilibrium is reached once elastic stresses balance the thermodynamic forcing that drives phase separation. In this equilibrium state, a negligible amount of solid remains within the cavities and the solid outside the cavities is uniformly compressed, with the same volume fraction throughout the domain. The formation of cavities damages the solid skeleton such that there is negligible elastic stress within the cavities. Although we may expect further coarsening to a global minimum of a single cavity over sufficiently long timescales (see discussion below), the results shown in Figure 3.1 are steady with respect to the length of our simulation. Different realisations of the initial noise ν give rise to qualitatively similar results, but with the exact position and size of the cavities varying.

Three key parameters with regard to the formation of gas cavities are the deformability of the solid matrix, $\mathcal{D}$, the strength of the interaction between the gas and solid phases, χ_{gs}, and the initial gas saturation, S_0. Recall that $\mathcal{D}$ measures the ratio of mixing energy to elastic energy, whereas χ_{gs} measures the energetic cost of gas–solid interactions. Typically, χ_{gs} is a function of physical properties such as the size and wetting characteristics of the solid particles. If the grains are smaller or if the gas phase is more strongly non-wetting to the solid, then the energetic cost of gas invading the pore space will be larger, resulting in a larger value of χ_{gs}. We further discuss the interpretation of χ_{gs} in terms of concrete physical variables in §4.3. The initial gas saturation S_0 measures how much gas is present in the system. If there is insufficient gas present, then capillary effects will not be strong enough to open macroscopic cavities and phase separation will not occur. We next investigate the impact of varying $\mathcal{D}$ and χ_{gs} on phase separation by running

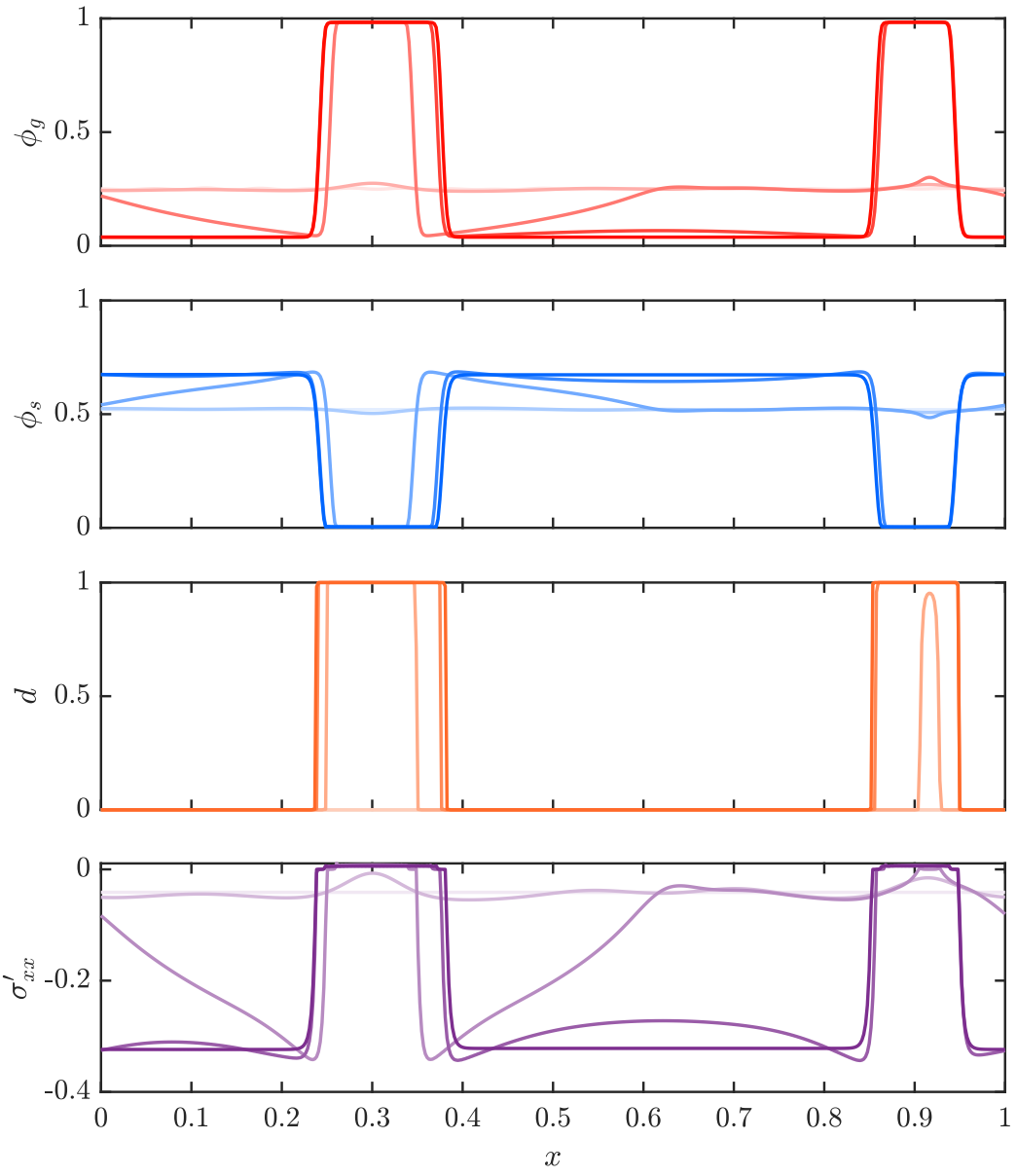

Figure 3.1: Numerical solution of our model illustrates how an initially homogeneous mixture will spontaneously separate into gas-rich cavities surrounded by a compressed, gas-poor porous domain. We show the distribution of ϕ_g, ϕ_s, d and σ'_{xx} at times $t = 0$, 0.004, 0.006, 0.008 and 1 (light to dark colours). Note that the distributions of d at $t = 0.008$ and $t = 1$ overlap such that they are indistinguishable at this scale. We use parameter values of $\phi_0 = 0.5$, $\phi^* = 0.02$, $S_0 = 0.55$, $\Theta = 10^{-4}$, $\mathcal{M}_r = 50$, $\mathcal{D} = 2$, $\varsigma = 0.1$, $\chi_{gl} = 3.5$, $\chi_{gs} = 3$, $\chi_{gsl} = 0$, $\Gamma_i = 10^{-4}$, $\kappa_c = 10^{-4}$ and $\mathcal{L}_d = 10^{-8}$. These parameter values give results which are representative of simulations for the full range of parameter values considered in the rest of this chapter, and for different realisations of the initial noise.

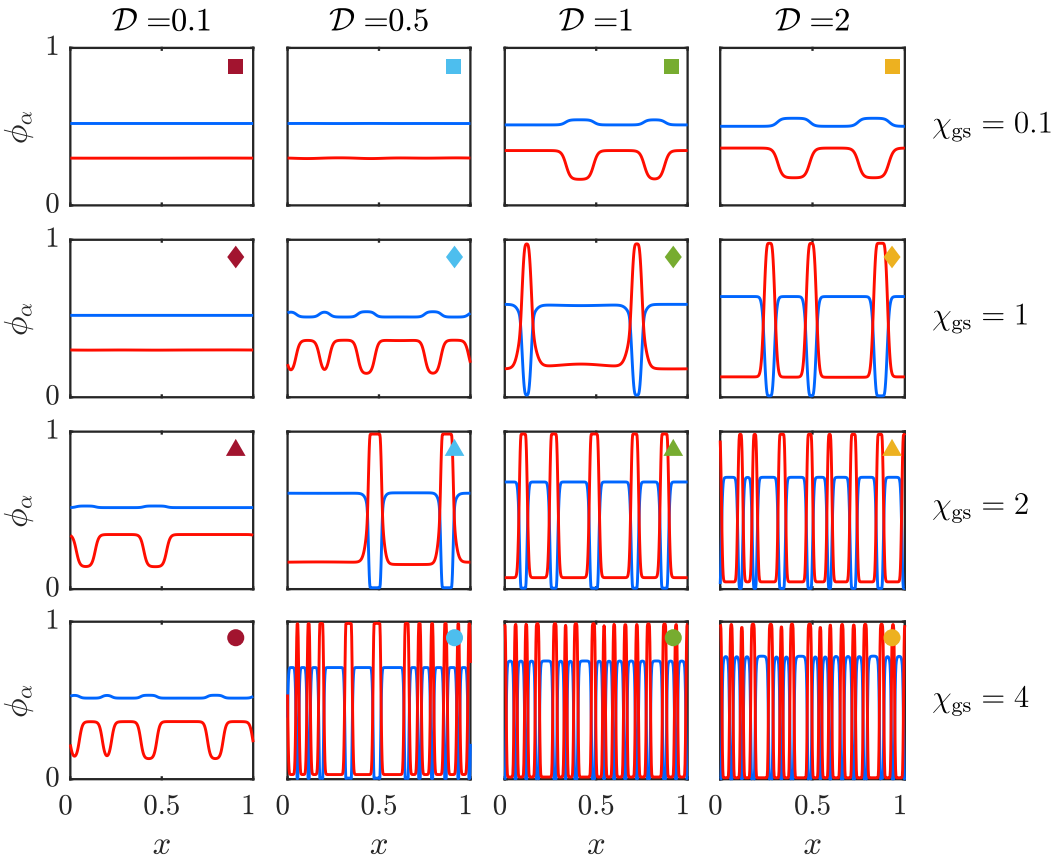

Figure 3.2: Steady-state distribution of ϕ_g (red) and ϕ_s (blue) from numerical simulations for a range of different characteristic deformabilities $\mathcal{D}$ and gas–solid interaction strengths χ_{gs}. Cavity formation is suppressed for low deformability and low interaction strengths (top left corner) and promoted for high deformability and high interaction strengths (bottom right corner). Note that due to the periodic boundary conditions imposed, the average elastic stress in each simulation varies across the phase diagram. Coloured symbols identify each parameter combination for comparison with the reduced model in §3.3. We set $S_0 = 0.6$, $\mathcal{M}_r = 1$, $\varsigma = 0$, $\chi_{gl} = 3.5$ and $\chi_{gsl} = 3.5$. Other parameters are the same as in Figure 3.1.

numerical simulations for a range of parameter values. We discuss the effect of varying S_0 in §3.2 below.

Our simulations show three distinct regimes at steady-state (Figure 3.2). One of these is the spontaneous formation of macroscopic gas cavities, as illustrated in Figure 3.1. However, cavities do not form in all cases. When cavity formation is suppressed, there are then two possibilities for the gas distribution within the pore space: spontaneous separation into gas-rich and gas-poor domains *within the pore space* or remaining uniformly distributed. Physically, phase separation

within the pore space is a result of individual micro-bubbles coalescing to form macroscopic pore-invasive regions, but being unable to deform the solid sufficiently to form cavities. For clarity and conciseness, we refer to this phase-separated state as 'pore-bubbles'. Note that the formation of pore-bubbles still results in slight deformation of the solid skeleton. A uniform gas distribution results when phase separation is suppressed entirely.

Figure 3.2 shows that, typically, cavity formation occurs for large values of $\mathcal{D}$ and χ_{gs}, pore-space phase-separation occurs for intermediate values of $\mathcal{D}$ and χ_{gs}, and phase separation is completely suppressed for low values of $\mathcal{D}$ and χ_{gs}. We rationalise these trends by considering fixed $\chi_{gs} = 1$. For a stiff porous medium ($\mathcal{D} \lesssim 0.1$), the elasticity of the solid skeleton is too strong for capillarity to deform it. Gas thus remains homogeneously distributed within the pore space and all phase separation is suppressed. As $\mathcal{D}$ increases, the gas is able to deform the solid skeleton such that it can more easily rearrange into a series of pore-bubbles, separated by liquid-saturated regions of the pore space. For a sufficiently soft porous medium ($\mathcal{D} \gtrsim 1$), gas is then able to open macroscopic cavities within the packing through large deformations to the solid skeleton. The parameter χ_{gs} is a measure of the strength of capillary effects. For larger χ_{gs} it is more energetically costly for gas and solid to remain mixed, so cavity formation is promoted. Conversely, for lower χ_{gs}, gas-solid interaction is less energetically costly, and so phase separation occurs less readily.

Note that although the simulations shown here have reached an apparent steady solution, they do not represent the global equilibrium state. For a non-cohesive granular medium, in which damage of the solid skeleton is reversible, the global equilibrium is given by a single cavity or pore-bubble, minimising total interfacial energy. Indeed, we see coarsening behaviour in many of our simulations, with a larger number of cavities initially forming. Some of these cavities spontaneously collapse, forcing gas back into the pore space. Gas then diffuses through the pore space and re-separates from the solid skeleton by entering remaining cavities,

resulting in fewer, larger cavities. This is the same behaviour as seen in §2.2.1 for a gas–liquid system. We very rarely see the final equilibrium configuration of a single phase-separated region in our simulations. This is a result of the exponentially slow rate of coarsening in 1D, and a further suppression of coarsening resulting from the extremely slow rate of gas diffusion through the pore space. For porous media which have a cohesive or fibrillar microstructure, cavity formation necessarily results in irreversible damage to the solid skeleton. In this case, the global equilibrium may instead consist of several equally-sized cavities or pore-bubbles [Qiang et al., 2023]. The effect of irreversible mechanical damage could be included in our model through the use of a history-dependent damage function [Miehe et al., 2010a].

3.2 Linear Stability Analysis

For parameter regimes in which phase separation is possible, the initial state of a homogeneous distribution of gas within the pore space is an unstable equilibrium. Local perturbations about this state may lead to a thermodynamic instability that results in the formation of either cavities or pore-bubbles. To help identify the parameters that control the onset of this instability, we now perform a linear stability analysis of our model. To simplify the analysis, we focus on a region of the parameter space in which cavity formation is the dominant instability. We do so by neglecting the effect of ternary interactions between phases, setting $\chi_{gsl} = 0$. Ternary interactions are vital for capturing the desired phenomenological response during compression-driven cavity collapse (as discussed in detailed in Chapter 4), but do not qualitatively affect the dynamics of spontaneous phase separation. The main result of setting $\chi_{gsl} = 0$ is that the formation of pore-bubbles only occurs in a very narrow parameter range. Outside of this parameter range, the possible outcomes of our model are the formation of cavities or gas remaining uniformly distributed within the pore space.

We linearise the system about a base state that represents an undamaged, pre-compressed porous matrix of porosity $\phi_0' = \phi_0 - |\phi^*|$, the pore space of which is occupied by a homogeneous distribution of gas with saturation S_0 and volume fraction $\phi_{g0} = S_0\phi_0$. We assume that perturbations of size $\epsilon \ll 1$ about this base state take the form of normal modes with growth rate s and wavenumber k, such that the perturbed gas fraction and porosity are given by

$$\phi_g = \phi_{g0} + \epsilon\widehat{\phi}_g \exp(st + ikx) + \mathcal{O}\left(\epsilon^2\right), \tag{3.3a}$$

$$\phi = \phi_0' + \epsilon\widehat{\phi} \exp(st + ikx) + \mathcal{O}\left(\epsilon^2\right), \tag{3.3b}$$

where $\widehat{\phi}_g$ and $\widehat{\phi}$ characterise the $\mathcal{O}(\epsilon)$ contributions to ϕ_g and ϕ, respectively.

Substituting this ansatz (Equations 3.3) into our model (Equations 2.36–2.45) and linearising in ϵ leads to a set of equations that describe the evolution of small perturbations. To $\mathcal{O}(\epsilon)$, our model thus reduces to the following algebraic equations for $\widehat{\phi}_g$ and $\widehat{\phi}$,

$$\begin{aligned} s\widehat{\phi}_g = &-\mathcal{M}_r(1-\phi_{g0})\phi_{g0}\left[\left(\mathcal{H}_{gg}k^2 + \mathcal{N}_{gg}k^4\right)\widehat{\phi}_g + \left(\mathcal{H}_{gf}k^2 + \mathcal{N}_{gf}k^4\right)\widehat{\phi}\right] \\ &+ (\phi_0' - \phi_{g0})\phi_{g0}\left[\left(\mathcal{H}_{lg}k^2 + \mathcal{N}_{lg}k^4\right)\widehat{\phi}_g + \left(\mathcal{H}_{lf}k^2 + \mathcal{N}_{lf}k^4\right)\widehat{\phi}\right], \end{aligned} \tag{3.4a}$$

$$\begin{aligned} s\widehat{\phi} = &-\mathcal{M}_r(1-\phi_0')\phi_{g0}\left[\left(\mathcal{H}_{gg}k^2 + \mathcal{N}_{gg}k^4\right)\widehat{\phi}_g + \left(\mathcal{H}_{gf}k^2 + \mathcal{N}_{gf}k^4\right)\widehat{\phi}\right] \\ &- (1-\phi_0')(\phi_0' - \phi_{g0})\left[\left(\mathcal{H}_{lg}k^2 + \mathcal{N}_{lg}k^4\right)\widehat{\phi}_g + \left(\mathcal{H}_{lf}k^2 + \mathcal{N}_{lf}k^4\right)\widehat{\phi}\right]. \end{aligned} \tag{3.4b}$$

In the above, we have introduced the functions $\mathcal{H}_{\alpha\beta} = \frac{\partial\mathcal{H}_\alpha}{\partial\phi_\beta}|_{\phi_0',\phi_{g0}}$, where $\mathcal{H}_\alpha = \Pi_\alpha + \sigma_{xx}'$ is the homogeneous part of the chemical potential of phase α, and the parameters $\mathcal{N}_{\alpha\beta}$, which are different combinations of interfacial coefficients. In general, $\mathcal{H}_{\alpha\beta}$ and $\mathcal{N}_{\alpha\beta}$ depend on the dimensionless groups defined in §2.1.6 and the base states ϕ_{g0} and ϕ_0', but they are constant with respect to k and s. Explicit expressions for $\mathcal{H}_{\alpha\beta}$ and $\mathcal{N}_{\alpha\beta}$ are presented in Appendix C. Collecting like terms

and finding the eigenvalues of Equations (3.4) leads to the dispersion relation

$$s^2 + \zeta_1(k)\, k^2 s + \zeta_2(k)\, k^4 = 0, \tag{3.5}$$

where $\zeta_1(k) = a_1 + a_2 k^2$ and $\zeta_2(k) = b_1 + b_2 k^2 + b_3 k^4$. Explicit forms of a_i and b_i are given in Appendix C.

As noted above, s is the growth rate of small perturbations to the homogeneous system described by Equations (3.3). The dispersion relation allows us to calculate s as a function of the wavenumber, k, of a particular perturbation. If $\Re(s) < 0$ for all values of k (where $\Re(s)$ is the real part of s), then perturbations will decay and the system is stable — gas will remain in the pore space of the solid skeleton. If $\Re(s) > 0$ for any value of k, then perturbations with this particular wavenumber (or range of wavenumbers) will grow exponentially, and the system will be unstable — phase separation will lead to macroscopic gas cavities. The solution of Equation (3.5) is

$$s = -\frac{\zeta_1 k^2}{2} \pm \frac{k^2}{2}\sqrt{\zeta_1^2 - 4\zeta_2}, \tag{3.6}$$

with small-k limit

$$s \approx -\frac{a_1 k^2}{2} \pm \frac{k^2}{2}\sqrt{a_1^2 - 4b_1}, \tag{3.7}$$

which shows that $\Re(s) > 0$ at small k whenever either $a_1 < 0$ or $b_1 < 0$. In these cases, all perturbations with wavenumbers between zero and some cut-off value k_c will be unstable and lead to phase separation. The cut-off value k_c is defined by the non-zero roots of $\zeta_2(k)$. Our system also has the unusual characteristic of instead forming an unstable band of wavenumbers $k \in [k_a, k_c]$, such that $k_a > 0$ under certain circumstances. This characteristic occurs when $a_1 > 0$ and $b_1 > 0$, and $\zeta_2(k)$ has two distinct non-zero roots, which requires that both $b_2 < 0$ and $4b_1 b_3 < b_2^2$. The condition for stability is thus that

$$a_1 > 0 \quad \text{and} \quad b_1 > 0 \quad \text{and} \quad \left(b_2 > 0 \;\text{ or }\; 4b_1 b_3 > b_2^2\right). \tag{3.8}$$

As a_i, b_i are complicated functions of many different parameters, we further explore the consequence of these stability conditions via a phase plane. Specifically, we plot the spinodal (or neutral stability) curves, for which $\Re(s) = 0$, which separate stable and unstable regions of the parameter space.

Equation (3.6) also reveals the possibility of oscillatory modes of instability, for which s is complex, under certain parameter combinations. For the parameter space investigated below, these oscillatory modes occur so close to the spinodal curves that they are not observed in the simulations, and, as such, we do not explore them any further here.

3.2.1 Onset of Phase Separation

The stability condition defined in Equation (3.8) allows us to predict the regions of the parameter space in which phase separation occurs and the regions in which it does not. In Figure 3.3, we plot the spinodal curve for various values of χ_{gs} in the $\mathcal{D} - S_0$ plane. This phase plane shows the physically intuitive behaviour described above. For a particular value of χ_{gs}, phase separation occurs in the top-right corner of the phase plane and is suppressed in the bottom-left corner. Phase separation is promoted as χ_{gs} increases, because if the interaction energy between the gas and solid phases is larger, then the energetic cost of their mixing is larger. For a given value of χ_{gs}, there exists a value of S_0 below which phase separation will not occur.

The deformability of the solid skeleton has a strong influence on the onset of phase separation. At low $\mathcal{D}$, the solid matrix is too stiff to be deformed by capillary forces and the gas will remain within the pore space. For larger values of $\mathcal{D}$, however, the solid skeleton is more easily deformed, and capillary forces may be able to overcome elastic resistance and open macroscopic cavities, provided that S_0 is large enough (*i.e.*, that enough gas is present). For a given value of χ_{gs}, there exists a value of $\mathcal{D}$ below which phase separation will not occur, regardless of S_0. Note also that

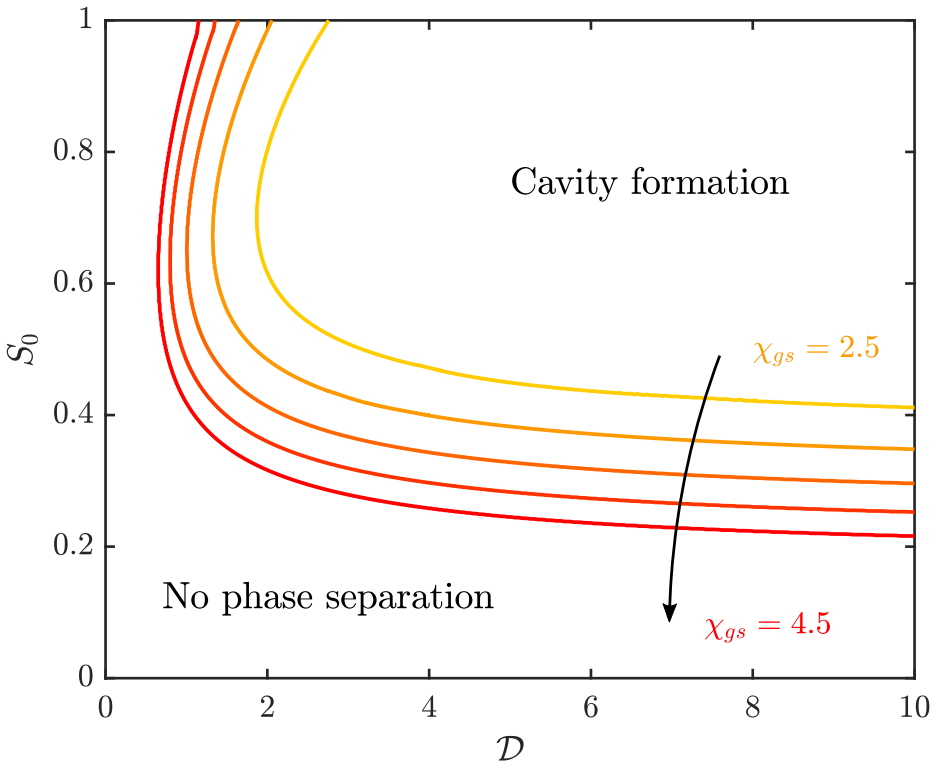

Figure 3.3: A phase plane showing the regions of stability (no phase separation) and instability (cavity formation) from the linear stability analysis of the full 1D system. Spinodal curves are plotted for a range of values of the gas–solid interaction parameter, χ_{gs}. An increase in χ_{gs} corresponds to an increase in capillary potential due to, for example, a smaller grain size, making it more energetically costly for gas to remain within the pore space and therefore promoting phase separation. All other parameters are the same as in Figure 3.1.

phase separation is suppressed for $S_0 \sim 1$. This region of the parameter space corresponds to an almost completely gas-saturated porous medium, and so the total energy of interaction between gas and liquid will be small.

3.2.2 Characteristic Cavity Size

In addition to the parameters that control the onset of phase separation, we also investigate the characteristic size of the gas cavities, Δ_g. The characteristic cavity size can be estimated from the linear stability analysis by finding the wavenumber of the most unstable mode at each point in the parameter space, k^*, and estimating $\Delta_g \approx \frac{\pi}{k^*}$. Doing so for a range of $\mathcal{D}$ then allows us to predict cavity size as

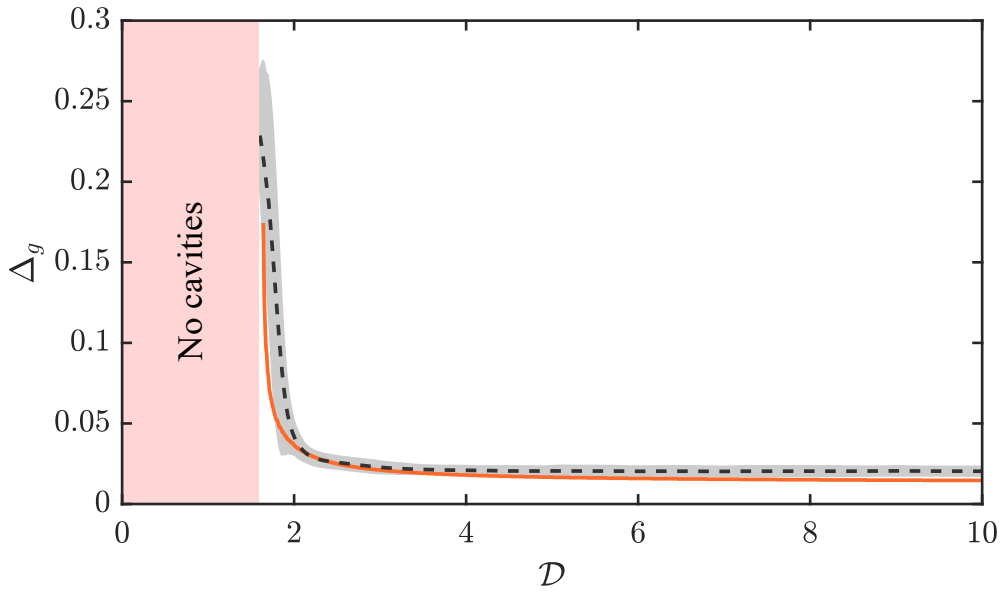

Figure 3.4: Characteristic size of gas cavities, Δ_g, as a function of deformability, $\mathcal{D}$, from numerical simulations (black) and linear stability analysis (orange). The numerical results are the mean (black) and standard deviation (grey band) of 50 slightly different initial conditions at each value of $\mathcal{D}$. Cavity size is calculated from numerical simulations before any thermodynamic coarsening takes place. All other parameters are the same as in Figure 3.1.

a function of deformability. We compare this prediction with the mean cavity size at steady state from numerical simulations (Figure 3.4). Note that Δ_g is a non-dimensional length scale. In dimensional variables, Δ_g corresponds to the proportion of the domain which is taken up by a cavity.

As $\mathcal{D}$ increases, Δ_g decreases. However, the total amount of gas within cavities increases with $\mathcal{D}$, so this decrease in Δ_g is offset by an increase in the total number of cavities. This behaviour can also be seen qualitatively in Figure 3.2: for a fixed value of χ_{gs}, there are more, smaller cavities for large $\mathcal{D}$ than for small $\mathcal{D}$. Intuitively, we might expect larger cavities to form in a softer material since the solid skeleton can undergo larger deformations. Indeed, the total 'cavity volume' is larger for softer materials, but these cavities are smaller and more numerous. We attribute this observation to the fact that, in a softer material, a smaller amount of gas is needed locally to open a cavity. For a stiff porous material, a large amount of gas will need to accumulate in order to force open a cavity, and so when the

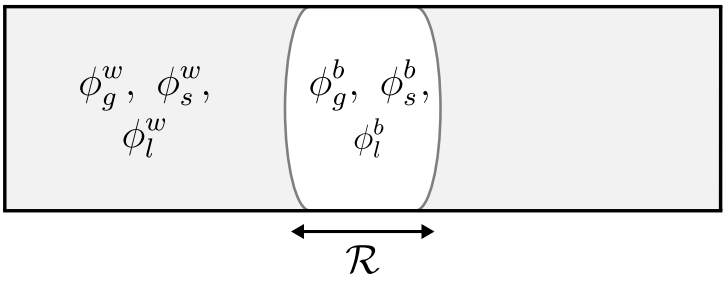

Figure 3.5: A schematic to show the assumed form of the solution used to construct a reduced, equilibrium model. The solution has two distinct regions; we define these as the 'bubble' and 'wet' regions, which have size $\mathcal{R}$ and $1 - \mathcal{R}$, respectively.

cavity is formed, it will be correspondingly larger.

Our numerical simulations show remarkably good qualitative and quantitative agreement with the linear stability analysis for the value of Δ_g, which is surprising given the strongly nonlinear nature of this process. Figure 3.4 also shows that, as expected, there exists a certain critical deformability below which phase separation does not occur. The linear stability analysis and numerical simulations show this transition occurring at around the same value of $\mathcal{D}$.

3.3 Reduced Model

We now use the results of our numerical simulations to inform the construction of a reduced, equilibrium form of our model. Such a model allows further exploration of the parameter space in an efficient manner. A simplified model also allows us to elucidate the different energetic effects that control cavity formation.

To construct a reduced model that represents the global equilibrium state, we assume that the solution takes the form of a single phase-separated gas region (cavity or pore-bubble) surrounded by compressed, liquid-saturated porous medium. A representation of this solution is shown in Figure 3.5. We assume that there exists a gas-rich region of non-dimensional size $\mathcal{R} \in [0, 1]$ surrounded by a gas-poor region of size $1 - \mathcal{R}$. This construction can capture all possible equilibrium states

(cavity, pore-bubble or homogeneous). For conciseness, we refer to the gas-rich region of the solution as the 'bubble' region, and the gas-poor region of the solution as the 'wet' region, regardless of the state. Within the bubble region, composition is uniform, and volume fractions are denoted ϕ_α^b. Similarly, within the wet region, composition is also uniform, and volume fractions are denoted ϕ_α^w. A bubble gas fraction of $\phi_g^b \sim 1$ and solid fraction of $\phi_s^b \sim 0$ represent a cavity. For the homogeneous state, $\mathcal{R} = 0$, $\phi_\alpha^w \equiv \overline{\phi}_\alpha$, where $\overline{\phi}_\alpha$ is the average volume fraction of each phase in our domain, and ϕ_α^b is undefined. A pore-bubble corresponds to volume fractions of $\phi_g^b > \overline{\phi}_g$ and $\phi_s^b \sim \overline{\phi}_s$. In theory, it is also possible to find equilibrium states that are between cavities and pore-bubbles, with $0 < \phi_s^b < \overline{\phi}_s$; in practice (both in numerical simulations of the full model and equilibrium solutions of the reduced model), these states are never found.

For systems in which $\overline{\phi}_\alpha$ are fixed, conservation of gas and solid constrain possible solutions such that

$$\mathcal{R}\phi_g^b + (1-\mathcal{R})\phi_g^w = \overline{\phi}_g \tag{3.9}$$

and

$$\mathcal{R}\phi_s^b + (1-\mathcal{R})\phi_s^w = \overline{\phi}_s. \tag{3.10}$$

We note that $\phi_l^{b,w}$ can be calculated from the no-void condition, $\sum_\alpha \phi_\alpha^{b,w} = 1$. Equations (3.9) and (3.10) reduce our system to just three degrees of freedom. We choose $\mathcal{R}$, ϕ_g^b and ϕ_l^b as free variables, calculating all other volume fractions from these when required. Following the free energy developed in §2.1.4, the total energy for a bubble of size $\mathcal{R}$ is then

$$\mathfrak{F}_T = \mathcal{R}\mathfrak{F}_M(\phi_g^b, \phi_l^b) + (1-\mathcal{R})\left[\mathfrak{F}_M\left(\phi_g^w, \phi_l^w\right) + \mathfrak{F}_E\left(\phi_s^w\right)\right], \tag{3.11}$$

with the mixing energy of each region, $\mathfrak{F}_M$, given by

$$\mathfrak{F}_M\left(\phi_g, \phi_l\right) = \phi_g \log \phi_g + \phi_l \log \phi_l + \chi_{gs}\phi_g\phi_s + \chi_{gl}\phi_g\phi_l + \chi_{gsl}\phi_g\phi_s\phi_l, \tag{3.12}$$

and the elastic energy, $\mathfrak{F}_E$, given by

$$\mathfrak{F}_E = \frac{1}{2\mathcal{D}J_w}\left[J_w^2 - 1 - 2\log J_w + \varsigma\left(\log J_w\right)^2\right], \tag{3.13}$$

where $J_w = \frac{1-\phi_0}{\phi_s^w}$. Note that there is no elastic energy in the bubble region due to the inability of the solid skeleton to support tension. We neglect both the damage and interfacial energies in this formulation. Results of our numerical simulations in §3.1 show that the total damage energy is typically very small compared to the mixing and elastic energies. Similarly, whilst the interfacial energy is the key driver of thermodynamic coarsening, and is in fact relatively large in the vicinity of diffuse interfaces, it is globally very small compared to the other energetic contributions.

To find equilibrium states of the reduced model, we seek to minimise Equation (3.11) over the variables $\mathcal{R}$, ϕ_g^b and ϕ_l^b. To simplify this minimisation, we note that for a fixed combination of parameters, the equilibrium value of ϕ_l^b (the amount of residual liquid in a gas bubble), is relatively insensitive to $\mathcal{R}$ and ϕ_g^b. This feature is unsurprising, as the ternary energy diagram shown in Figure 2.2 displays a notable invariance along the $\phi_l = 0$ axis; that is, the mixing energy does not depend strongly on ϕ_g and ϕ when ϕ_l is small. The equilibrium value of ϕ_l^b does depend more strongly on χ_{gl} and χ_{gsl}, but we keep these parameters fixed for simplicity in the analysis that follows. Equilibrium states can thus be found by fixing ϕ_l^b to a value informed by our numerical simulations of the full model and then minimising Equation (3.11) over $\mathcal{R}$ and ϕ_g^b by numerically finding the minimal value of $\mathfrak{F}_M[\mathcal{R}, \phi_g^b]$ for the corresponding matrix $[\mathcal{R}, \phi_g^b]$.

3.3.1 Energy of Cavity Formation

To understand the energetics of cavity formation, we first investigate a region of the parameter space in which pore-bubbles do not form, so that we expect either

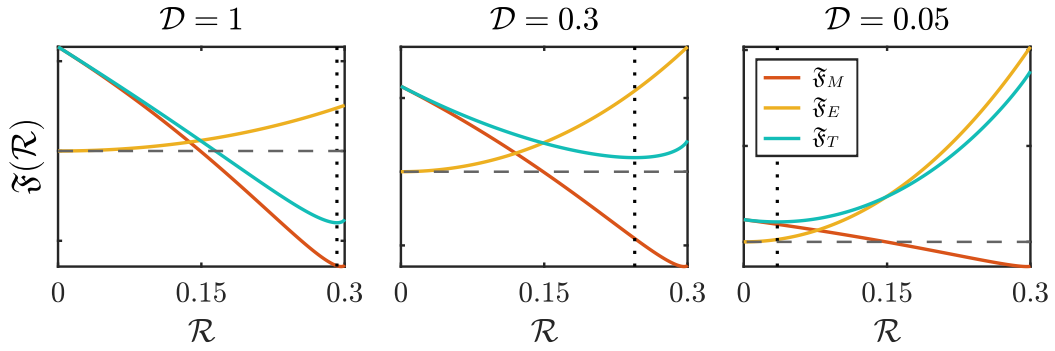

Figure 3.6: Solutions of the reduced model (Equations 3.9–3.13) showing mixing energy (red), elastic energy (yellow), and total energy (turquoise) as functions of cavity size for $\mathcal{D} = 1$, 0.3 and 0.05, and $\phi_g^b = 1$. The dotted line corresponds to the value of $\mathcal{R}$ for which $\mathfrak{F}_T$ is minimum in each case. The dashed grey line indicates $\mathfrak{F} = 0$. Note that $\mathfrak{F}$ is plotted on a different vertical scale for each value of $\mathcal{D}$, hence axis labels are not displayed. We set $\overline{\phi}_s = 1 - \phi_0 = 0.5$, $\overline{\phi}_g = 0.3$, $\phi_l^b = 0.0001$, $\varsigma = 0$, $\chi_{gs} = 4$, $\chi_{gl} = 3.5$ and $\chi_{gsl} = 3.5$.

the formation of open cavities or that the mixture remains homogeneous. We can then further simplify our reduced model by setting $\phi_g^b = 1$ and $\phi_l^b = 0$ (pure gas cavity), such that the size of the cavity, $\mathcal{R}$, is the only free variable. Figure 3.6 shows the mixing energy, elastic energy and total energy as functions of $\mathcal{R}$, for three different values of $\mathcal{D}$. For all values of $\mathcal{D}$, we see that $\mathfrak{F}_M$ has a minimum at $\mathcal{R}_{\text{eq}} \sim 0.3$, which corresponds to all of the gas entering the cavity (since we have taken $\overline{\phi}_g = 0.3$). This result is as expected: neglecting elastic effects, it is always energetically favourable for the gas to completely de-mix from the solid and liquid. On the other hand, $\mathfrak{F}_E$ increases monotonically with $\mathcal{R}$. This result is also as expected: as $\mathcal{R}$ increases, the solid skeleton is increasingly compressed, resulting in a larger elastic cost. Note that $\mathfrak{F}_E$ is always positive, but that $\mathfrak{F}_M$ and $\mathfrak{F}_T$ may be positive or negative.

For $\mathcal{D} = 1$, the solid skeleton is very soft, and changes in $\mathfrak{F}_M$ dominate changes in $\mathfrak{F}_E$. As a result, $\mathfrak{F}_T$ has a minimum at $\mathcal{R}_{\text{eq}} \sim 0.3$ (black dotted line), which corresponds to the equilibrium cavity size. As $\mathcal{D}$ decreases, the solid is less deformable and changes in $\mathfrak{F}_E$ becomes large enough to compete with changes in $\mathfrak{F}_M$. For $\mathcal{D} = 0.3$, the equilibrium cavity size is then smaller, resulting from a balance between capillary and elastic effects. For $\mathcal{D} = 0.05$, the elastic cost of

cavity formation dominates and $\mathcal{R}_{\text{eq}} \sim 0$. In practice, the diffuse interfaces of our phase-field model impose a minimum possible size for cavities, set by the width of the diffuse interface. As such, cavities will most likely not form for $\mathcal{D} = 0.05$, and gas will remain in the pore space.

3.3.2 Equilibrium Regime Diagram

We now allow ϕ_g^b to vary such that our reduced model captures both pore-bubbles and cavities. Which of these two states is the global equilibrium depends on which has the lower total energy. Figure 3.6 shows how the minimum energy and corresponding equilibrium bubble size vary for a given value of $\phi_g^b = 1$. Extending this analysis to all possible values of ϕ_g^b, we then identify the value of ϕ_g^b that results in the lowest minimum energy. We find that the minimum energy is always given by either $\phi_g^b \sim 1$ (cavity), or $\phi_g^b \sim \phi_0$ (pore-bubble). Figure 3.7 shows a regime diagram highlighting the different regions of the parameter space for which cavities and pore-bubbles are energetically favoured, separated by the purple line. We find that, in general, large values of $\mathcal{D}$ and χ_{gs} result in open cavities as the equilibrium state, and small values of $\mathcal{D}$ and χ_{gs} give pore-bubbles, which is consistent with the results of our full model. The coloured symbols in Figure 3.7 represent the different simulations presented in Figure 3.2. The crossover between the formation of cavities and the formation of pore-bubbles is well predicted by our reduced model.

The above analysis focuses on the global equilibrium. Regardless of the global equilibrium state, it is possible for either cavities or pore-bubbles to represent a local equilibrium state; indeed, for much of the 'cavity region' in Figure 3.7, there also exists a local energetic minimum corresponding to a pore-bubble. This result raises the possibility of 'meta-stable' states, in which the system may arrive (and remain) at a local equilibrium despite the existence of a separate, global

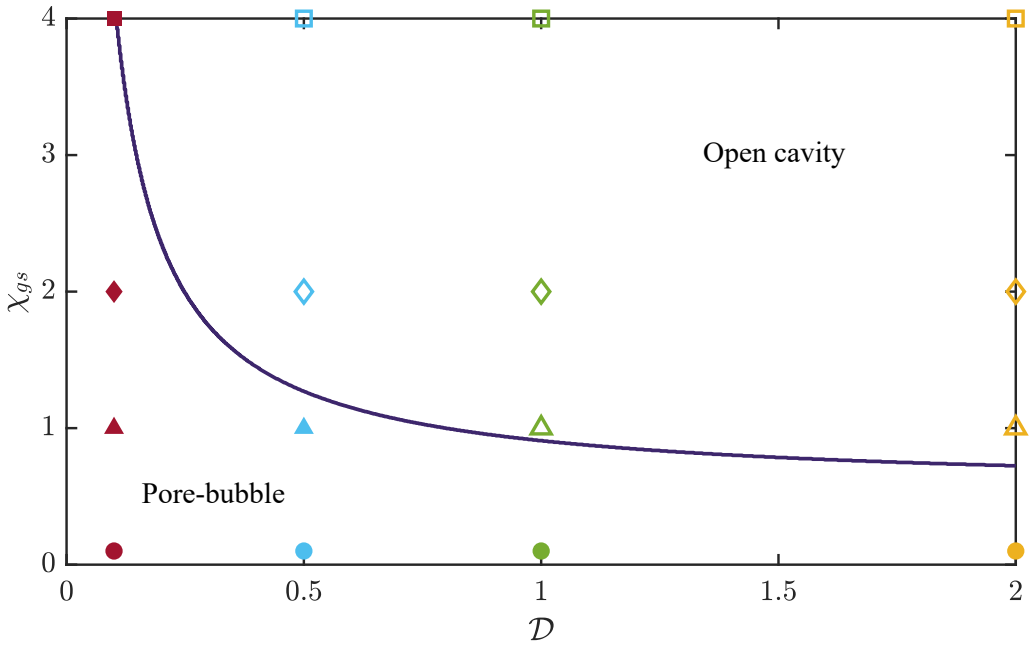

Figure 3.7: Regime diagram showing different equilibrium states from the reduced model, separated by the purple line. For large $\mathcal{D}$ and χ_{gs}, the equilibrium state is an open cavity. For small $\mathcal{D}$ and χ_{gs}, the equilibrium state is a pore-bubble. The coloured symbols represent the parameter combinations corresponding to the simulations of the full model in Figure 3.2. Open symbols indicate simulations where cavities form, and filled symbols represent simulations where they do not. To generate the purple line, we set $\overline{\phi}_s = 0.52$, $\overline{\phi}_g = 0.288$ and $\phi_l^b = 0.01$. These parameter values are equivalent to the initial conditions used to generate Figure 3.2. All other parameters are the same as in Figure 3.2.

equilibrium. We consider these meta-stable states in more detail in the context of cavity collapse in §4.2.

In Figure 3.8, we plot the equilibrium bubble size from our reduced model, $\mathcal{R}_{\text{eq}}$, for a fixed value of $\chi_{gs} = 2$. The dependence of $\mathcal{R}_{\text{eq}}$ on $\mathcal{D}$ shows two qualitatively different behaviours depending on whether the equilibrium state is a pore-bubble or a cavity. For $\mathcal{D} \lesssim 0.45$, pore-bubbles are the equilibrium state and $\mathcal{R}_{\text{eq}}$ decreases with $\mathcal{D}$. As $\mathcal{D}$ passes the crossover point between pore-bubbles and cavities, $\mathcal{R}_{\text{eq}}$ drops suddenly. For $\mathcal{D} \gtrsim 0.45$, cavities are the equilibrium state and $\mathcal{R}_{\text{eq}}$ increases with $\mathcal{D}$. The sudden drop in $\mathcal{R}_{\text{eq}}$ across the transition between pore-bubbles and cavities is expected: gas in pore-bubbles is limited to a maximum volume fraction $\phi^b \sim \phi_0$, whereas in cavities $\phi^b \sim 1$. A given amount of gas will therefore occupy

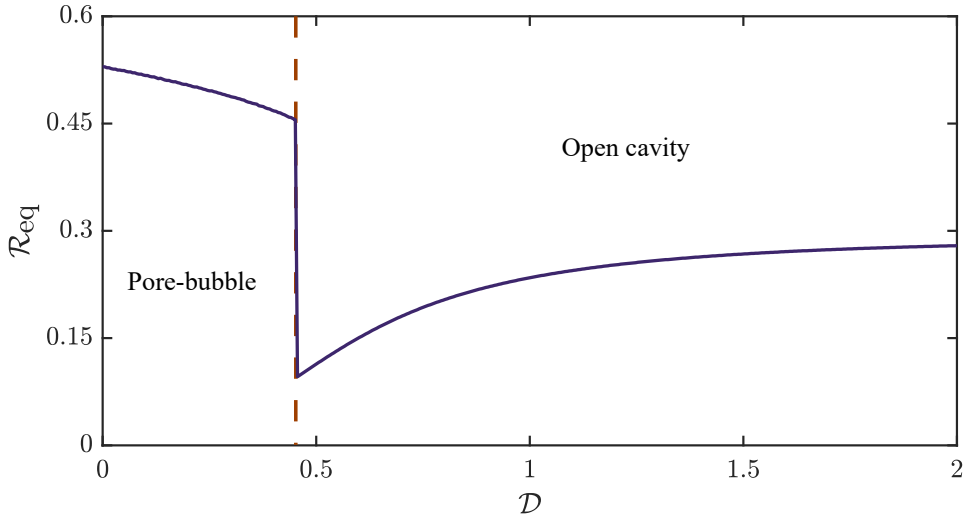

Figure 3.8: Equilibrium bubble size as a function of $\mathcal{D}$ calculated from the reduced model with $\chi_{gs} = 2$. $\mathcal{R}_{\rm eq}$ decreases with $\mathcal{D}$ for pore-bubbles ($\mathcal{D} \lesssim 0.45$), but increases with $\mathcal{D}$ for cavities ($\mathcal{D} \gtrsim 0.45$). All other parameters are the same as in Figure 3.7.

a larger region as a pore-bubble than as a cavity. We explain the dependence of $\mathcal{R}_{\rm eq}$ on $\mathcal{D}$ in the pore-bubble regime in the same manner: as $\mathcal{D}$ increases, the pore-bubble is able to more easily deform the local pore space, such that ϕ^b is larger, and the bubble occupies a smaller region. For the cavity regime, larger $\mathcal{D}$ means that it is easier for the cavity to compress the solid skeleton, and so larger cavities are able to form (as also demonstrated in Figure 3.6). This is in contrast with the characteristic cavity size predicted by numerical simulations and linear stability analysis in §3.2.2. We emphasise that Figure 3.4 shows the size of cavities which initially separate from a homogeneous state, rather than the total amount of 'cavity volume'. Over time, we expect cavities to coarsen until eventually they reach the global equilibrium of a single cavity, whose size is predicted by Figure 3.8.

3.4 Summary

In this chapter, we have investigated the spontaneous formation of gas cavities from a gas–liquid–solid mixture. Numerical simulations of the phase-field model

developed in Chapter 2 demonstrate the formation of open cavities, in which gas separates from the pore space by displacing both liquid and solid. We find that phase separation is inhibited by elastic resistance from the solid, which imposes limits on the conditions under which cavities form: if the solid skeleton is too stiff, gas will remain within the pore space, either as phase-separated 'pore-bubbles' or in a homogeneous state.

We have shown how the onset of phase separation depends on different parameters, including the deformability of the solid matrix and the strength of fluid–solid interactions, via both linear stability analysis and numerical simulation. We have found the surprising result that, for a softer porous material, we expect smaller, but more numerous, cavities to spontaneously form than for a stiffer porous material. This fact is a result of a smaller amount of gas needing to accumulate within the pore space in order to open a cavity in the softer case. In the equilibrium state however, we expect a single cavity, the size of which increases with increasing deformability. Finally, we have also constructed a reduced, equilibrium version of our full model and used it to rationalise our numerical results.

Quantitative predictions of the characteristic size, and corresponding size distribution, of non-wetting fluid bubbles are important for understanding the macroscopic mechanical properties of a range of deformable porous media, such as gassy soils [Wheeler, 1986] and soft composite materials [Style et al., 2015, Bartlett and Style, 2020]. Our results indicate that it is vital to not only assess the size and number of bubbles, but also their state of pore occupancy, when characterising non-wetting fluid distributions. Whether or not non-wetting fluid invades the pore space or forms open cavities significantly affects the expected bubble size, as well as the qualitative dependence of bubble size on relevant material properties (Figure 3.8).

Chapter 4

Cavity Collapse: Theory

As a second test problem, we consider the deformation-driven collapse of cavities due to increasing confining stress. At equilibrium, the characteristic size and number of cavities in a given soft porous medium depends primarily on a balance between capillary forces and elastic stresses. Increasing the confinement will shift this balance by increasing the elastic stress in the solid skeleton. Sufficiently large confining stress may trigger either partial or complete cavity collapse, with gas invading the pore space, as capillary forces are no longer sufficient to deform the solid skeleton. The role of confining stress in determining whether a non-wetting fluid (*e.g.*, gas) forms open cavities or remains within the pore space is widely acknowledged [Wheeler, 1988a, Lee et al., 2020], but the dynamic transition between these two states due to changing confining stress has received little attention, and remains poorly understood.

In this chapter, we study the collapse of a gas cavity due to compression via a fluid-permeable piston. Although unlikely to be directly relevant to natural physical systems, this simple scenario is helpful for understanding the physics of cavity collapse. In §4.1, we conduct numerical simulations of our phase-field model to explore the phenomenology of cavity collapse, identifying the confining stress at which cavities collapse and the key parameters that control this process. Next, in §4.2, we investigate the reversibility of cavity formation and collapse under

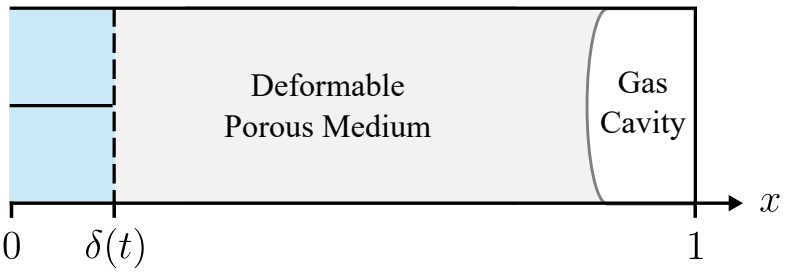

Figure 4.1: Deformation-driven collapse of a pre-existing cavity in 1D. We study the case of a single gas cavity (right side) subject to increasing compression via a fluid-permeable piston (left side), the position of which is denoted δ.

sequentially increasing and then decreasing confinement via numerical simulations complemented by further analysis of the reduced model derived in §3.3. Finally, in §4.3, we compare the results of our numerical simulations with predictions from a simple toy model of cavity collapse, allowing us to connect the phenomenological free-energy parameters of our phase-field model with concrete physical properties.

4.1 Phase-Field Simulations

To study deformation-driven cavity collapse, we first conduct numerical simulations of the phase-field model developed in Chapter 2. A schematic of the arrangement investigated here is shown in Figure 4.1. For simplicity, we focus on the case of a single gas cavity within an otherwise relaxed, liquid-saturated porous medium. The cavity is initially situated at the far right side of the domain, and has initial size Δ_g^0. Confinement increases via the motion of a fluid-permeable piston at the left side. The piston is freely permeable to liquid and gas, but not to solid. We take the right side of the domain to be fixed and impermeable (or equivalently, a line of symmetry). We study displacement-controlled deformation, in which the (non-dimensional) position of the piston, $\delta(t)$, is imposed. We choose $\delta(t)$ to be a linear function of time up to a maximum displacement δ^*, so that piston speed $\dot{\delta}$ is constant.

We focus exclusively on the slow-piston limit. In this case, the response of our system can be assumed to be quasi-static; the state of the system will pass continuously through a series of local equilibria. The quasi-static limit can be formalised as requiring sufficiently slow piston motion that rate effects are not important. In our system, this constraint requires that viscous pressure gradients resulting from both poromechanical and capillary effects are able to dissipate sufficiently fast compared to the motion of the piston. For this constraint to be satisfied, we require that

$$\mathcal{T}_{\text{cap}},\ \mathcal{T}_{\text{pe}} \ll \dot{\delta}^{-1},$$

where $\mathcal{T}_{\text{cap}} = \frac{L^2}{\mathcal{M}_l^0 \mathcal{E}_{\text{mix}}}$ is the characteristic time scale associated with liquid transport by capillary effects, as defined in §2.1.6, and $\mathcal{T}_{\text{pe}} = \frac{L^2}{\mathcal{M}_l^0 G} = \mathcal{T}_{\text{cap}} \mathcal{D}$ is the classical poroelastic timescale.

4.1.1 Numerical Method

We solve the model equations outlined in §2.1.6 on the domain $x \in [\delta(t), 1]$, for times $t \in [0, t_{\text{f}}]$. We take $\delta(t) = \dot{\delta} t$, such that $\delta(0) = 0$ and $t_f = \frac{\delta^*}{\dot{\delta}}$, where δ^* is the maximum displacement. For the impermeable boundary at the right side, we impose no-flux conditions for the two fluids, and a no-displacement condition for the solid:

$$v_s|_{x=1} = w_g|_{x=1} = w_l|_{x=1} = 0. \tag{4.1}$$

Recall that the total mixture flux $q = v_s + w_g + w_l$ must be a function of time only. Evaluating this expression at $x = 1$ suggests that $q = 0$. At the left boundary, we enforce that the piston is impermeable to solid by setting $v_s|_{x=\delta} = \dot{\delta}$. To find boundary conditions for the fluid flux at the piston, we evaluate q at $x = \delta$ to give

$$q = \dot{\delta} + w_g|_{x=\delta} + w_l|_{x=\delta} = 0. \tag{4.2}$$

We also assume that transport of gas and liquid through the piston are purely advective, implying that there are no capillary effects resulting from the composition of the mixture exterior to the domain. This assumption is enforced by requiring that gradients in capillary potential vanish,

$$\frac{\partial \mu_\alpha}{\partial x}\Big|_{x=\delta} = \frac{\partial p}{\partial x}\Big|_{x=\delta}. \tag{4.3}$$

Combining Equations (4.2) and (4.3) then implies that

$$\dot{\delta} = (\mathcal{M}_r \phi_g + \phi_l)\frac{\partial p}{\partial x}\Big|_{x=\delta}. \tag{4.4}$$

Explicit boundary conditions for gas and liquid flux at the piston are then

$$w_g|_{x=\delta} = -\mathcal{M}_r \frac{\phi_g}{(\mathcal{M}_r \phi_g + \phi_l)}\dot{\delta}\Big|_{x=\delta} \tag{4.5a}$$

and

$$w_l|_{x=\delta} = -\frac{\phi_l}{(\mathcal{M}_r \phi_g + \phi_l)}\dot{\delta}\Big|_{x=\delta}. \tag{4.5b}$$

Finally, we also impose that gradients in order parameter vanish at each boundary, such that $\frac{\partial \phi}{\partial x} = \frac{\partial \phi_g}{\partial x} = \frac{\partial d}{\partial x} = 0$ at $x = \delta$ and $x = 1$. The choice of these boundary conditions is justified by assuming that the boundary at $x = \delta$ (*i.e.*, the piston) is inert with respect to interactions with the gas–liquid–solid mixture, and by interpreting the boundary at $x = 1$ as a symmetry line.

The above system of equations is a moving-boundary problem. To solve it, it is convenient to re-scale to a static domain $x_* \in [0, 1]$ via the transformation

$$x_* = \frac{x - \delta}{1 - \delta}. \tag{4.6}$$

Using the chain rule, we see that for some variable $h(x_{(*)}, t)$,

$$\frac{\partial h}{\partial x} = \frac{1}{1 - \delta}\frac{\partial h}{\partial x_*}, \tag{4.7a}$$

$$\frac{\partial h}{\partial t} = \frac{\partial h}{\partial t} - \frac{(1-x_*)\,\dot{\delta}}{1-\delta}\frac{\partial h}{\partial x_*}. \tag{4.7b}$$

Using this transformation in our governing equations and dropping the stars results in an additional factor $1/L^*$ in front of every spatial derivative, where $L^* = 1-\delta$ is the rescaled domain length, as well as a new advective-like term in the evolution equations for gas fraction and porosity:

$$\frac{\partial \phi_g}{\partial t} = (1-x_*)\,\frac{\dot{\delta}}{L^*}\frac{\partial \phi_g}{\partial x} - \frac{1}{L^*}\frac{\partial}{\partial x}\left[(1-\phi_g)\,w_g - \phi_g w_l\right] \tag{4.8}$$

and

$$\frac{\partial \phi}{\partial t} = (1-x_*)\,\frac{\dot{\delta}}{L^*}\frac{\partial \phi}{\partial x} - \frac{1}{L^*}\frac{\partial}{\partial x}\left[(1-\phi)\,w_g + (1-\phi)\,w_l\right], \tag{4.9}$$

where we have also set Q_0 equal to zero.

To represent a cavity of size Δ_g^0 at the right side of the domain, we initialise simulations with ϕ_g and ϕ given by

$$\phi_g(x,0) = \begin{cases} 0 & \text{for } x < 1-\Delta_g^0, \\ 1 & \text{for } x \geq 1-\Delta_g^0, \end{cases} \qquad \phi(x,0) = \begin{cases} \phi_0 & \text{for } x < 1-\Delta_g^0, \\ 1 & \text{for } x \geq 1-\Delta_g^0. \end{cases} \tag{4.10}$$

We take the initial damage profile to be equal to the initial porosity profile, $d(x,0) = \phi(x,0)$. We enforce this set of initial conditions in a smooth manner via hyperbolic tangent functions. This initial condition closely approximates that of the equilibrium state at $\delta = 0$, so the solution very rapidly adjusts to that equilibrium at the beginning of each simulation. The motion of the piston is negligible during this brief adjustment period. This equilibrium state is then the effective initial condition for the simulation, and is shown in the top panel of Figure 4.2. We solve our equations as described in §2.1.6, but use a first-order upwinding finite difference scheme for the advective terms.

4.1.2 Phenomenology of Cavity Collapse

Figure 4.2 shows the results of an example simulation of deformation-driven cavity collapse. The top panel shows the effective initial state, with the piston (grey dashed line) at $x = 0$ and an open cavity of size $\Delta_g^0 = 0.18$ at the right side of the domain. As the piston advances, liquid leaves the domain at the left side (through the piston). Initially, cavity size remains approximately constant while the solid skeleton becomes increasingly compressed. As solid deformation increases, the elastic energy stored in the porous medium also increases. Eventually, it becomes energetically favourable for gas to invade the pore space rather than further compress the solid (third panel). As gas invades the pore space, it remains compact in space, forming a phase-separated state that corresponds to an almost-completely gas-saturated pore-invaded region (pore-bubble). In this pore-invaded region, the solid skeleton is relaxed compared to the liquid-saturated region at the left of the domain. We denote piston position at initial pore invasion by δ_1. As the piston further advances, gas continues to enter the pore space from the cavity until the cavity vanishes (bottom panel). We denote the piston position at which cavity collapse is complete by δ_2. Further displacement of the piston beyond δ_2 corresponds to compression of a partially saturated porous medium.

Figure 4.3 shows cavity size Δ_g and confining stress $\overline{\sigma}$ as functions of δ (black dashed lines). Confining stress is determined by evaluating the effective stress, σ'_{xx}, at the piston, $x = 0$. This figure highlights the three distinct regimes of cavity collapse described above. We refer to these regimes as 'pre-invasion' (Figure 4.2 panels 1 and 2), 'post-invasion' (panels 3 and 4) and 'post-collapse' (panel 5). During the pre-invasion regime ($\delta < \delta_1$), cavity size remains approximately constant and confining stress increases in line with the constitutive response of the solid skeleton (fairly linearly, here). Once gas invades the pore space ($\delta > \delta_1$), cavity size then decreases linearly with δ and confining stress remains constant. We denote the value of $\overline{\sigma}$ during this stress plateau by $\overline{\sigma}_{\text{plat}}$. During the post-invasion

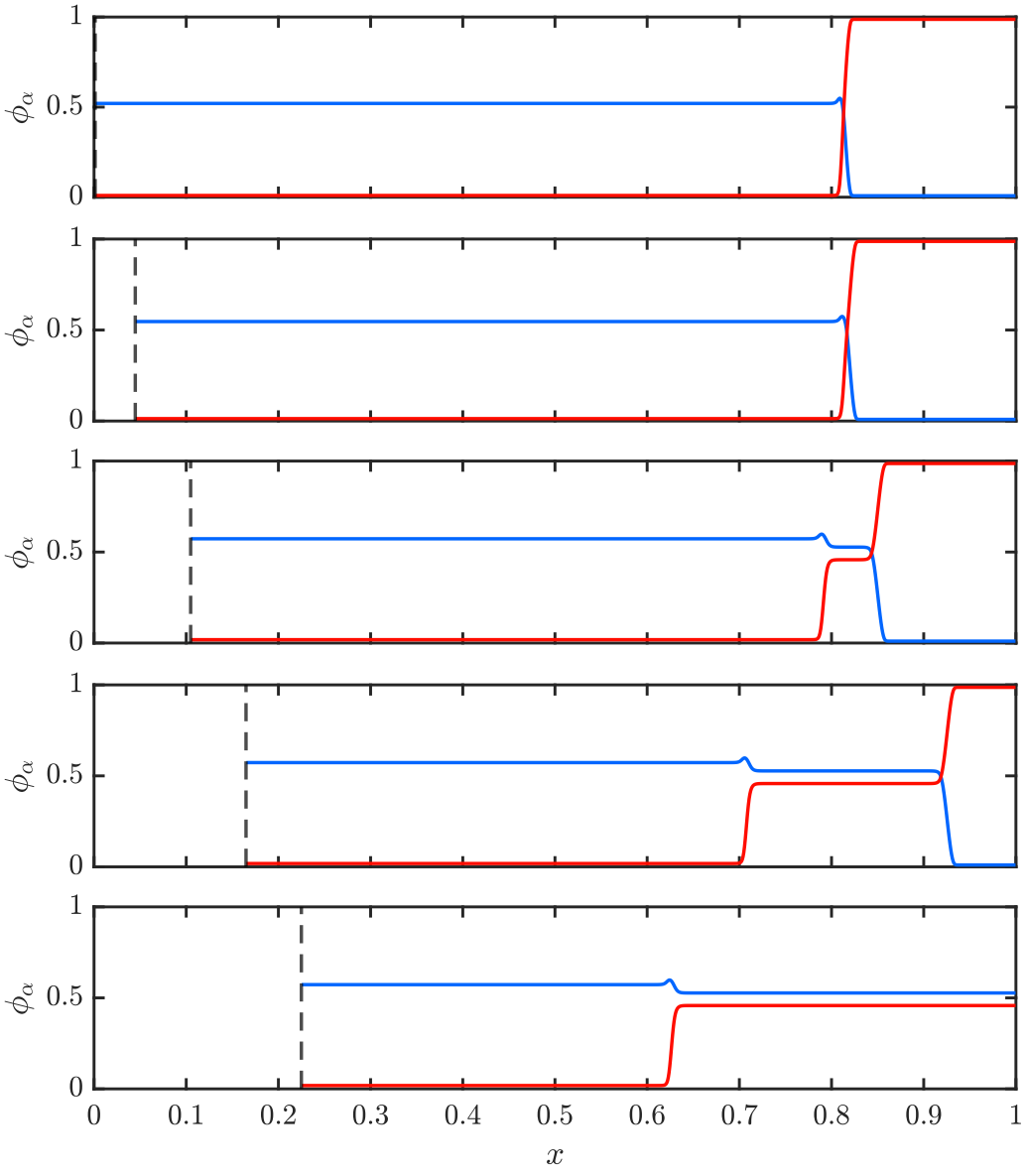

Figure 4.2: Snapshots of a numerical simulation of deformation-driven cavity collapse, showing the distribution of ϕ_g (red) and ϕ_s (blue), at times $t = 10$, 445, 1045, 1640, and 2240 (top to bottom). As the piston (grey dashed line) advances, solid is increasingly compressed, eventually leading to gas invading the pore space and the cavity collapsing. Note that the small bump in ϕ_s is a numerical artefact that decreases in size for decreasing Γ_i, and which does not otherwise influence simulation results. The initial cavity size is $\Delta_g^0 = 0.18$ and the piston speed is $\dot{\delta} = 0.0001$. We use parameter values of $\phi_0 = 0.5$, $\Theta = 10^{-4}$, $\mathcal{M}_r = 1$, $\mathcal{D} = 0.5$, $\varsigma = 0$, $\chi_{gl} = 5$, $\chi_{gs} = 1.5$, $\chi_{gsl} = 5$, $\Gamma_i = 10^{-4}$, $\kappa_c = 10^{-4}$ and $\mathcal{L}_d = 10^{-8}$.

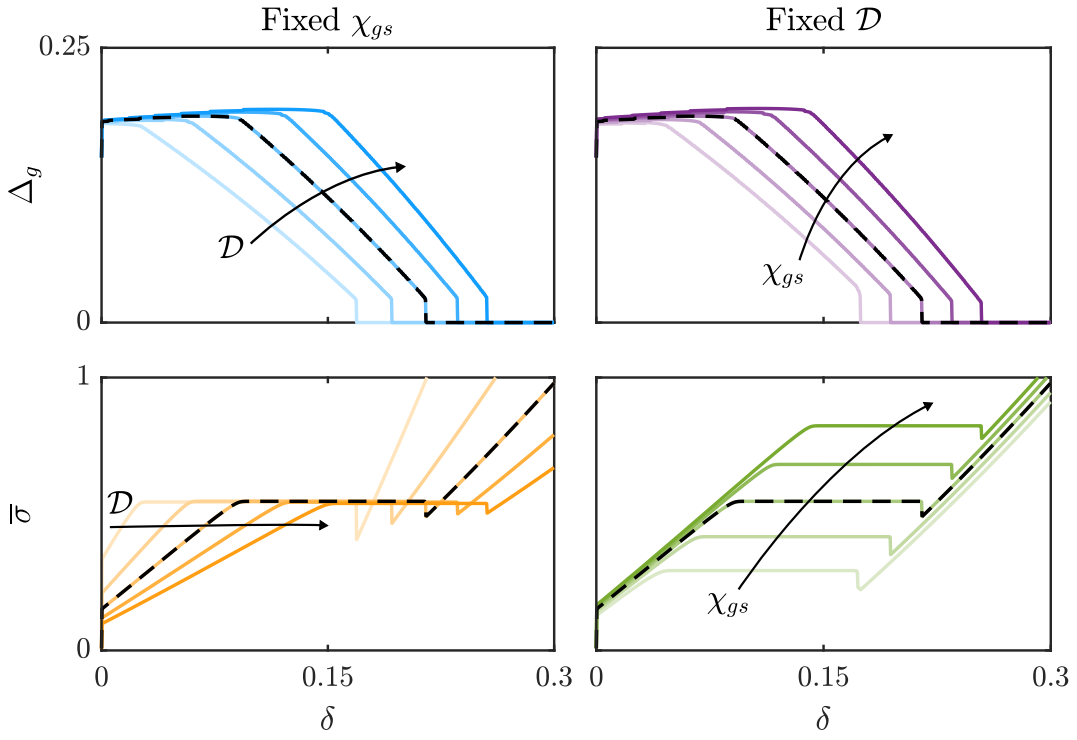

Figure 4.3: Cavity size (top row) and confining stress (bottom row) as functions of piston position computed from numerical simulations of deformation-driven cavity collapse for a range of $\mathcal{D}$ and χ_{gs}. The dashed black lines show the results for the simulation shown in Figure 4.2. For the left panels, $\chi_{gs} = 1.5$ and $\mathcal{D}$ is 0.2, 0.35, 0.5, 0.65 and 0.8 (light to dark colours). For the right panels, $\mathcal{D} = 0.5$ and χ_{gs} is 1, 1.25, 1.5, 1.75 and 2 (light to dark colours). All other parameters are the same as in Figure 4.2. Compare the second row with Figure 4.9.

regime, the porous medium is effectively being 'shunted' along by the piston, with gas entering from the cavity at right, and liquid exiting through the piston at the left. Once the cavity has completely collapsed ($\delta > \delta_2$), cavity size remains equal to zero and confining stress resumes increasing as the solid skeleton is compressed against the impermeable right boundary. Note that the magnitude of the slope of the stress-displacement curve in the post-collapse regime is larger than in the pre-invasion regime. We attribute the different constitutive responses in these two regimes to the presence of the 'relaxed' solid in the pore-invaded region. Note also that the cavity size Δ_g does not decrease smoothly to zero, but rather vanishes relatively suddenly once it reaches a small but nonzero critical size. This feature is a result of our phase-field approach, which effectively imposes a minimum possible cavity size corresponding to the width of the diffuse interface. This drop in

cavity size also leads to a drop in confining stress at the end of the plateau region, before $\overline{\sigma}$ begins increasing again. Reducing the size of the interfacial parameters Γ_i reduces the size of these drops.

We now investigate the effect of various model parameters on cavity collapse. Figure 4.3 shows the result of numerical simulations for a range of values of $\mathcal{D}$ and χ_{gs}, keeping all other parameters fixed. First, we vary $\mathcal{D}$ and fix χ_{gs} (left panels). As $\mathcal{D}$ increases, the slope of the stress-displacement curve in the pre-invasion and post-collapse regions decreases, but $\overline{\sigma}_{\text{plat}}$ does not change. In general, pore invasion occurs because it is energetically unfavourable to further increase elastic energy beyond some critical value. Increasing the deformability of the solid skeleton (*i.e.*, larger $\mathcal{D}$; a softer porous medium) implies that more deformation will be needed to reach this critical value of elastic energy (*i.e.*, pore invasion begins later), but does not change the critical value itself.

Next, we vary χ_{gs} and fix $\mathcal{D}$ (right panels). The evolution of cavity size as a function of δ varies with χ_{gs} in much the same way as it varies with $\mathcal{D}$: as χ_{gs} increases, pore invasion is delayed. As χ_{gs} increases, however, $\overline{\sigma}_{\text{plat}}$ also increases. Increasing χ_{gs} increases the energy penalty of gas and solid mixing, and so pore invasion is more energetically costly for large χ_{gs} than for small χ_{gs}. The confining stress required to trigger pore invasion is thus correspondingly larger. However, the stiffness of the material (*i.e.*, the rate at which $\overline{\sigma}$ increases with δ) is essentially independent of χ_{gs}. Thus, although increasing $\mathcal{D}$ and increasing χ_{gs} lead to delayed pore invasion, the reasons behind this delay are different. Increasing $\mathcal{D}$ decreases the rate at which $\overline{\sigma}$ approaches $\overline{\sigma}_{\text{plat}}$ without changing the value of $\overline{\sigma}_{\text{plat}}$, whereas increasing χ_{gs} increases the value of $\overline{\sigma}_{\text{plat}}$ without changing the rate at which $\overline{\sigma}$ increases.

4.1.3 Three-State Coexistence

A striking feature of the simulation shown in Figure 4.2 is the fact that gas remains compact in space once it enters the pore space, resulting in the 'staircase state' seen in the third and fourth panels. We find that the existence of the staircase state depends strongly on the value of the ternary interaction parameter χ_{gsl}. When χ_{gsl} is sufficiently small (or equal to zero), the gas does not remain compact, but instead spreads rapidly throughout the entire pore space. The diffusive-like transport of gas for low χ_{gsl} results in a fundamentally different phenomenology for cavity collapse; in particular, a stress plateau is no longer observed. For intermediate values of χ_{gsl}, the result is somewhere between the two extremes, with gas initially spreading throughout the pore space as the cavity collapses, before a staircase state then forms later in the cavity collapse process. Which of these different phenomenologies is appropriate depends on the specific nature of the system being studied. For the remainder of this thesis, we focus on the large χ_{gsl} case, in which the staircase state forms, as we expect this to be the right physical behaviour for the class of systems which we are interested in. We note that the ability of a ternary interaction term to stabilise three-state coexistence has previously been studied in the context of multi-component lipid mixtures [Idema et al., 2009].

4.2 Meta-Stability of Cavity Collapse

Many natural soft porous media experience fluctuating confinement. Thus, it is natural to ask whether collapsed cavities will re-form as confinement decreases. We investigate this possibility by studying what happens when the piston retracts to its initial position once it has reached its maximum displacement. We focus on a single compression-relaxation cycle, but we expect similar behaviour to occur for additional cycles. Using the final state of cavity collapse (*e.g.*, bottom panel

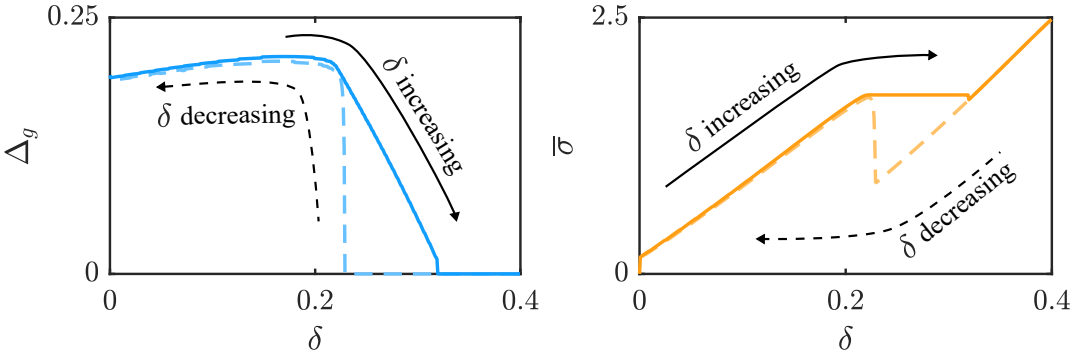

Figure 4.4: Cavity size, Δ_g, and confining stress, $\overline{\sigma}$, as functions of δ from numerical simulation of cavity collapse and re-formation for $\mathcal{D} = 0.5$ and $\chi_{gs} = 3$. Solid lines indicate an advancing piston (compression) and dashed lines indicate a retracting piston (relaxation). All other parameters are the same as in Figure 4.2.

of Figure 4.2) as the new initial state, we now conduct numerical simulations in which $\delta(t) = \delta^* - \dot{\delta}t$ from $t = 0$ to $t = t_f$.

As a starting point, we first consider what happens when confinement is decreased before the cavity has fully collapsed (*e.g.*, using the penultimate panel of Figure 4.2 as the initial condition). We find that, in this case, cavity collapse is fully reversible. As the piston retracts, gas re-enters the cavity from the pore space, the cavity fully reforms, and the solid skeleton fully relaxes. Simulations of this process are well represented by considering the snapshots in Figure 4.2 in reverse order (*i.e.*, from penultimate panel to top panel). Cavity size and confining stress again follow the paths plotted in Figure 4.3, but in reverse.

When confinement is decreased after complete cavity collapse, however, we find that cavity collapse is not a fully reversible process. Figure 4.4 shows cavity size and confining stress for an example simulation demonstrating this behaviour. The key feature of this simulation is that cavity re-formation is delayed compared to cavity collapse: cavity re-formation occurs at smaller δ and lower $\overline{\sigma}$ than those at which the cavity originally collapsed ($\delta = \delta_2$), resulting in hysteresis in both cavity size and confining stress. We find that cavity re-formation happens suddenly and completely, with Δ_g abruptly jumping up to $\Delta_g \sim \Delta_g^0$ at some $\delta < \delta_2$.

Unlike during cavity collapse, there is no staircase state: all of the gas in the pore space emerges into the cavity at once. Similarly, the confining stress continues to decrease linearly until the point of cavity re-formation, where it then jumps up to $\overline{\sigma}_{\text{plat}}$ and decreases along the same path as during cavity collapse, which is controlled by the stiffness of the (now once again) liquid-saturated porous medium. We interpret this phenomenon as the persistence of meta-stable states beyond the point of global equilibrium and discuss the energetics of this process further in §4.2.1 below. We also note that in, general, the cavity does not re-form in its initial position.

4.2.1 Local Equilibrium States

In order to elucidate the behaviour observed in Figure 4.4, we use the reduced form of our model from §3.3 to construct the energy landscape for different values of δ. Setting the mean gas and solid fractions in the reduced model, $\overline{\phi}_g$ and $\overline{\phi}_s$, equal to the corresponding values in our numerical simulation, we then plot the total energy, $\mathfrak{F}_T$, as a function of the gas fraction in the bubble, ϕ_g^b (Figure 4.5, top panels). Each point on this plot represents the global minimum value of $\mathfrak{F}_T$ for each value of ϕ_g^b. The corresponding value of $\mathcal{R}$ that minimises $\mathfrak{F}_T$ is also shown (Figure 4.5, bottom panels).

To understand these plots, we start by considering a small amount of compression ($\delta = 0.12$; left column). In this case, $\mathfrak{F}_T$ has a single minimum at $\phi_g^b \sim 1$ (black dot). That is, the equilibrium state is a cavity. The size of this cavity is given by the dot on the lower panel. For a moderate amount of compression ($\delta = 0.24$; middle column), $\mathfrak{F}_T$ has two local minima: at $\phi_g^b \sim 1$ (as before) and now also at $\phi_g^b \sim 0.5$. The latter is a pore-bubble. This pore-bubble is a local minimum in the energetic landscape, but it is clearly not the global minimum and so we refer to it as a meta-stable state. For large compression ($\delta = 0.28$; right column), $\mathfrak{F}_T$ still has two local minima: at $\phi_g^b \sim 1$ and at $\phi_g^b \sim 0.4$. However, the latter

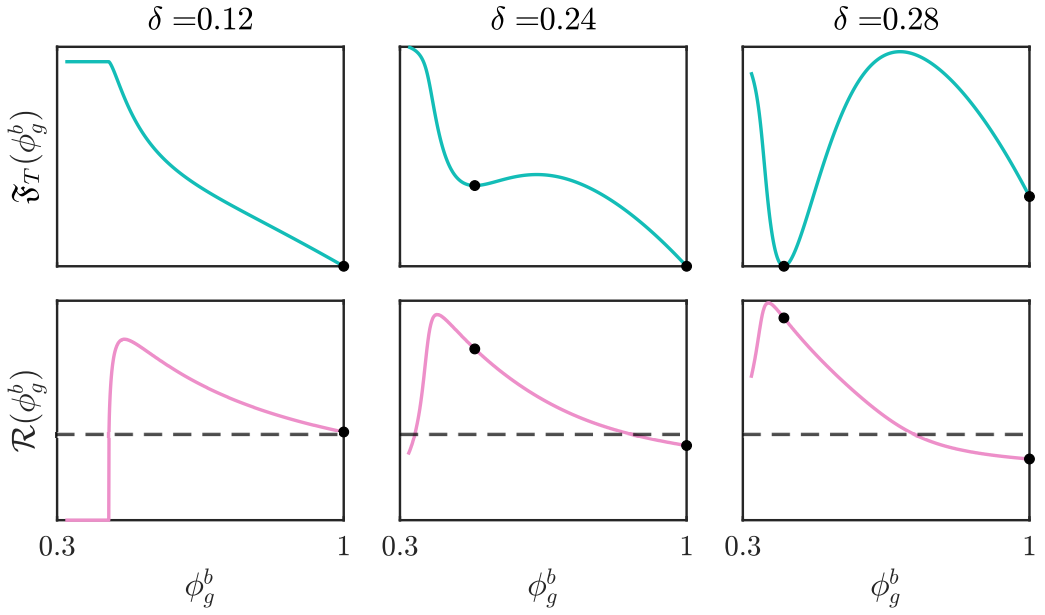

Figure 4.5: Results from our reduced model, highlighting how the structure of the energetic landscape changes with piston position. Top panels show the minimum achievable value of total energy $\mathfrak{F}_T$ (turquoise curve) at each value of ϕ_g^b. Black dots show the position of local energy minima. Note that the vertical scale varies from left to right in order to highlight the shape of $\mathfrak{F}_T$; the quantitative values of $\mathfrak{F}_T$ are unimportant and hence axis labels are not displayed. Bottom panels show the corresponding bubble size (*i.e.*, the value that minimises $\mathfrak{F}_T$) for each value of ϕ_g^b (pink curve). Dashed black lines show the values of $\mathcal{R}$ that correspond to all gas existing in a cavity. At each value of δ, we set $\overline{\phi}_s$ and $\overline{\phi}_g$ to equal the corresponding values from the simulation shown in Figure 4.4. All other parameters are the same as in Figure 4.4.

is now the global minimum. Thus, it is now energetically favourable to form a pore-bubble rather than a cavity. This transition makes intuitive sense: as δ increases, the solid skeleton is increasingly compressed. Correspondingly, it is more energetically costly for the gas to deform the solid and form a cavity. Pore-bubbles deform the solid skeleton significantly less than cavities, so it eventually becomes less energetically costly for gas to form a pore-bubble than a cavity. Note, however, that cavities remain meta-stable, representing a local minimum in the energy landscape.

In the simulation illustrated in Figure 4.4, the initial cavity size is $\Delta_g^0 = 0.18$ and the system is initially very near to its equilibrium state. The gas remains in this cavity as δ increases. As δ increases further, past δ_1, gas begins to invade the

pore space and form the staircase state discussed in §4.1.3, due to the emergence of a meta-stable pore-bubble state. This may seem counter-intuitive since cavity formation is still energetically more favourable than pore invasion. The middle panels of Figure 4.5 show an example energy landscape at a point where a staircase state occurs. For this value of δ, the equilibrium cavity size (lower panel, black dot) is lower than the initial cavity size (Δ_g^0, black dashed line). It is therefore not an energetic minimum for all of the gas that originally formed the cavity to remain within the cavity. Gas can thus either all remain as a cavity (but at a greater energetic cost), or it can invade the pore space, and also occupy the meta-stable equilibrium at $\phi_g^b \sim 0.4$. We find that the latter is typically less energetically costly. As δ continues to increase, the energy of pore invasion relative to cavity formation decreases, and so more gas invades the pore space until, eventually, pore-invasion is the global minimum, and all of the gas exists within the pore space ($\Delta_g = 0$).

As the piston retracts, the energetic landscape of the system changes in a reversible manner. At first, pore-bubbles are the equilibrium state and cavities are meta-stable, then cavities become the equilibrium state and pore-bubbles become meta-stable, and eventually the meta-stable pore-bubble state disappears altogether. In Figure 4.4, we see that as δ decreases, the staircase state never re-forms as δ decreases, despite the existence of a meta-stable cavity state. We rationalise this by noting that the formation of the staircase state was triggered by the equilibrium cavity size becoming less than the initial cavity size. Such a process does not happen for the pore-bubble state. Therefore, a pore-bubble is able to persist as a meta-stable equilibrium, rather than re-forming a partial cavity. As δ decreases further, the meta-stable pore-bubble state eventually ceases to exist (Figure 4.5, left panels), at which point the gas suddenly and spontaneously transitions into a cavity.

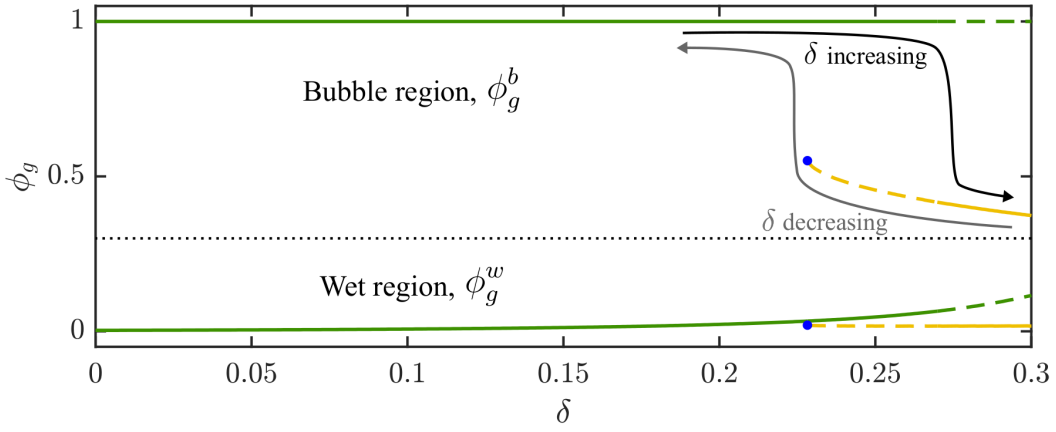

Figure 4.6: A bifurcation diagram constructed from our reduced model for the simulation shown in Figure 4.4. Solid lines correspond to equilibrium states and dashed lines correspond to meta-stable states. Green lines represent the cavity branch and yellow lines represent the pore-bubble branch. Blue dots indicate the value of δ below which the pore-bubble branch does not exist. All parameters are the same as in Figure 4.5.

4.2.2 Bifurcation Structure

We quantify how the different global and local equilibrium states vary over the course of a compression-relaxation cycle by constructing a bifurcation diagram (Figure 4.6). Here, we show the values of ϕ_g that correspond to equilibrium states as solid lines, and those which correspond to meta-stable states as dashed lines. The cavity branch is coloured green and the pore-bubble branch is coloured yellow. Note also that there always exists an additional equilibrium further to those discussed in Figure 4.5 that corresponds to the gas fraction in the wet region (outside of the bubble), and which is given by ϕ_g^w. When there are two branches in ϕ_g^b, there are two corresponding branches in ϕ_g^w.

As expected, we see that a cavity ($\phi_g^b \sim 1$) always represents a local energetic minimum, which transitions from the (global) equilibrium state to a meta-stable state for sufficiently large δ. In contrast, pore-bubbles only exist as local minima for $\delta \gtrsim 0.23$. The bifurcation diagram is helpful for explaining some of the behaviour discussed above. Decreasing confinement prior to complete cavity collapse corresponds to following the cavity branch ($\phi_g^b \sim 1$), but then retracting the

piston before reaching the transition to meta-stability. As such, this process is reversible. For the complete cavity collapse shown in Figure 4.4, the system eventually transitions to the pore-bubble branch, and then remains on this branch as δ subsequently decreases. Once the pore-bubble branch ceases to exist, the system jumps suddenly onto the cavity branch.

4.3 Identification of Phase-Field Parameters

The free energy developed in Chapter 2 involves a number of phenomenological parameters that together determine the shape of the energy landscape, among them χ_{gs}, χ_{gl} and χ_{gsl}. For our model to be applied to real-world systems, it is important to relate these parameters to concrete material properties. Deformation-driven cavity collapse is a convenient setting in which to examine the impact of these parameters on identifiable physical effects.

We start by considering the strength of gas–solid interactions, χ_{gs}. As discussed in §4.1.2, the value of χ_{gs} controls the plateau stress, $\overline{\sigma}_{\text{plat}}$. Figure 4.7a quantifies the impact of χ_{gs} on $\overline{\sigma}_{\text{plat}}$ across a series of simulations at different values of $\mathcal{D}$ and χ_{gsl}. Clearly, $\mathcal{D}$ and χ_{gsl} do not strongly influence the value of $\overline{\sigma}_{\text{plat}}$. The black line is a power-law fit to the simulation results,

$$\overline{\sigma}_{\text{plat}} = 0.3\chi_{gs}^{1.44}. \tag{4.11}$$

For $\chi_{gs} \lesssim 0.5$ (shaded region), cavities are unable to form and $\overline{\sigma}_{\text{plat}}$ is undefined.

Next, we consider the strength of gas–liquid interactions, χ_{gl}. We find that the primary role of χ_{gl} is to control the saturation at which gas invades the pore space during the staircase state (*i.e.*, during the stress plateau). We denote this saturation $\overline{S}_g$, and plot $\overline{S}_g$ as a function of χ_{gl} in Figure 4.7b. We fit a power law

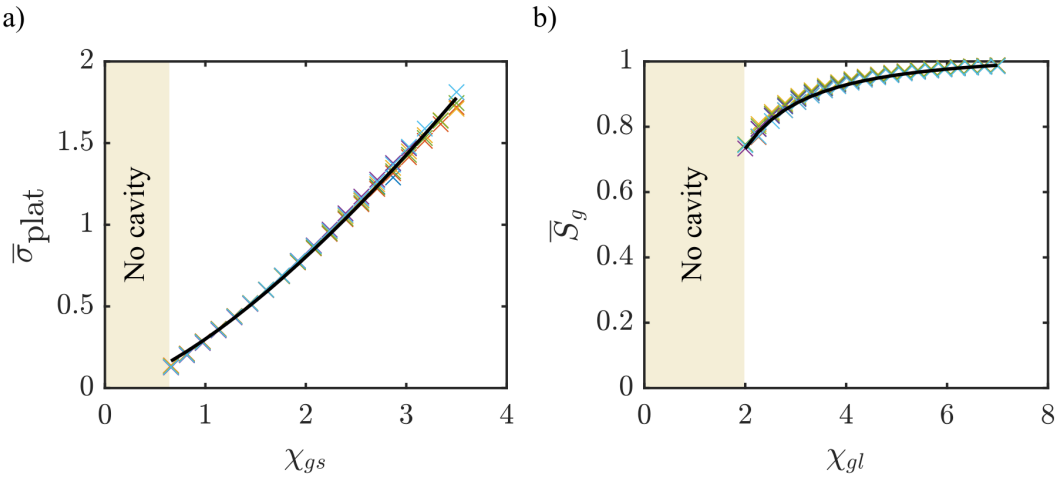

Figure 4.7: (a) Simulation results exploring the impact of χ_{gs} on $\overline{\sigma}_{\mathrm{plat}}$. Coloured crosses correspond to simulations with parameter values of $\mathcal{D} = 0.35$, 0.5 and 0.65 and $\chi_{gsl} = 1$, 3 and 5. The black line shows the power-law fit described in Equation (4.11). All other parameters are the same as in Figure 4.2. (b) Simulation results exploring the impact of χ_{gl} on $\overline{S}_g$. Coloured crosses correspond to simulations with parameter values of $\mathcal{D} = 0.35$, 0.5 and 0.65 and $\chi_{gs} = 1.5$, 2 and 2.5. The black line shows the power-law fit described in Equation (4.12).

to the liquid saturation $1 - \overline{S}_g$, finding that

$$\overline{S}_g = 1 - 0.86\chi_{gl}^{-1.52}. \tag{4.12}$$

Increasing χ_{gl} increases $\overline{S}_g$ by increasing the energetic cost of gas–liquid interactions, increasingly penalising the presence of liquid in the invaded region. For $\chi_g \lesssim 2$ (shaded region), cavities are unable to form and $\overline{S}_g$ is undefined.

4.3.1 Simple Toy Model

To link $\overline{\sigma}_{\mathrm{plat}}$ to physically meaningful material properties, we now consider a simple toy model of cavity collapse. Informed by our numerical simulations, we assume that, for a given piston position, there may exist three distinct regions: the uninvaded region, which consists of a liquid-saturated porous medium; the invaded region, where gas has entered the pore space to displace liquid; and the cavity,

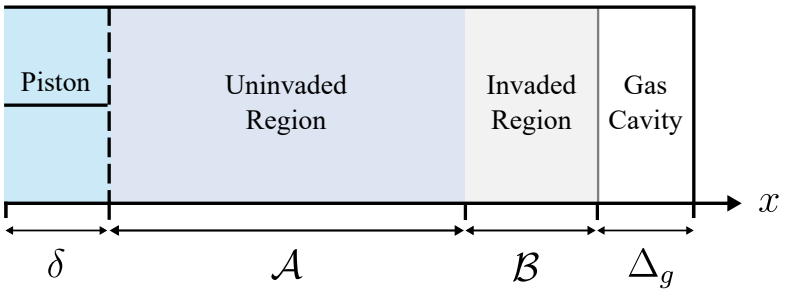

Figure 4.8: A schematic of the toy model, showing three distinct regions: the uninvaded region, the invaded region, and the gas cavity. At the left side of the porous medium, a fluid-permeable piston compresses the system. At the right side, there exists an impermeable boundary.

which consists only of gas (Figure 4.8). We denote the gas saturation in the invaded region by S_g^i. In our numerical simulations above, we primarily consider the limit of large χ_{gl}, in which $\overline{S}_g \sim 1$. Correspondingly, and for simplicity, we then assume that gas completely displaces pore-liquid such that S_g^i=1. We denote the porosity in the invaded region by ϕ^i and in the uninvaded region by ϕ^u. We denote the liquid and gas pressures by p_l and p_g, respectively. In the quasi-static limit, we assume that ϕ^i, ϕ^u, p_l and p_g are all uniform in space, allowing us to construct a zero-dimensional model. The sizes of each region are denoted $\mathcal{A}$, $\mathcal{B}$ and Δ_g, for the uninvaded, invaded and cavity regions, respectively. At the left, there exists a fluid-permeable piston with displacement δ from its initial position, δ_0. At the right, there is an impermeable wall a distance L from δ_0. Without loss of generality, we set $\delta_0 = 0$ and $L = 1$, such that $\delta + \mathcal{A} + \mathcal{B} + \Delta_g = 1$.

We consider the deformation-driven collapse of the gas cavity in the same manner as the numerical simulations described above. Initially, when $\delta = 0$, no gas has invaded the pore space ($\mathcal{B} = 0$) and the porous medium is relaxed ($\phi^u = \phi^i = \phi_0$). Conservation of mass for gas and solid requires that

$$\Delta_g + \mathcal{B}\phi^i = \Delta_g^0 \tag{4.13a}$$

and

$$(1 - \phi^u)\mathcal{A} + (1 - \phi^i)\mathcal{B} = (1 - \phi_0)\mathcal{A}_0, \tag{4.13b}$$

where Δ_g^0 and $\mathcal{A}_0$ are the initial size of the cavity and porous medium, respectively. We note that $\mathcal{A}_0 + \Delta_g^0 = 1$. We denote the elastic stress in the uninvaded region by σ^u, and note that this must be equal to the negative of the confining stress applied by the piston, $\overline{\sigma}$. Similarly, we denote the elastic stress in the invaded region by σ^i. Force balance then requires that at the interface between the invaded and uninvaded regions,

$$\sigma^i - \sigma^u = p_g - p_l \equiv p_c, \tag{4.14}$$

where p_c is defined as the capillary pressure, and σ^u, σ^i, p_g, p_l and p_c all represent dimensional quantities here. For simplicity, we assume a linearly elastic response for the elastic solid, such that

$$\sigma^{u,i} = M\mathcal{S} = M\frac{\phi^{u,i} - \phi_0}{1 - \phi_0}, \tag{4.15}$$

where M is the p-wave (oedometric) modulus and $\mathcal{S}$ is the true strain.

As δ begins to increase, the porous medium is compressed, but gas does not yet invade the pore space and $\mathcal{B} = 0$ (*i.e.*, this is the pre-invasion regime). Combining Equations (4.13)–(4.15) then reveals that the capillary pressure and confining stress are equal and given by

$$p_c = \overline{\sigma} = \frac{M\delta}{1 - \Delta_g^0 - \delta}. \tag{4.16}$$

Eventually p_c will reach p_c^e, the capillary entry pressure, defined as

$$p_c^e = \frac{2\gamma_{gl}\cos\vartheta_c}{r_p}, \tag{4.17}$$

where γ_{gl} is gas–liquid surface tension and ϑ_c is the contact angle. Once $p_c = p_c^e$, gas can freely invade the pore space (*i.e.*, this is the post-invasion regime). As the gas invades, we assume that the invaded region relaxes, such that $\phi^i = \phi_0$ and therefore that $\overline{\sigma} = p_c^e$ is constant, and $\mathcal{A}$, $\mathcal{B}$ and Δ_g^0 are determined by Equation (4.13). We note that the value of $\delta = \delta_1$ at the onset of pore invasion is

given by

$$\delta_1 = \frac{p_c^e}{M + p_c^e}\left(1 - \Delta_g^0\right). \tag{4.18}$$

Cavity collapse is complete when $\Delta_g = 0$. This occurs at $\delta = \delta_2$, where

$$\delta_2 = 1 - \left[\frac{M}{p_c^e} + \frac{\Delta_g^0}{\phi_0\left(1 - \Delta_g^0\right)}\right]\delta_1 \tag{4.19}$$

can be derived by setting $\Delta_g = 0$ in Equation (4.13a), and solving Equation (4.13b) for δ, with ϕ^u determined by $\overline{\sigma} = p_c^e$.

Once the cavity has completely collapsed, the elastic solid is in contact with the impermeable right boundary, which causes the invaded region to also compress, such that $\phi^i < \phi_0$. From Equation (4.14), the confining stress for $\delta > \delta_2$ is then given by $\overline{\sigma} = p_c^e - \sigma^i$. Recall that the stress in the invaded region, σ^i, is negative in compression, and determined by Equation (4.15). Solving Equations (4.13) with $\Delta_g = 0$ then gives

$$\overline{\sigma} = p_c^e - M\left[1 - \frac{1 - \Delta_g^0 - (1 + p_c^e)\mathcal{A}_2}{1 - \delta - \mathcal{A}_2}\right], \tag{4.20}$$

where $\mathcal{A}_2 = 1 - \delta_2 - \frac{\Delta_g^0}{\phi_0}$ is the size of the uninvaded region at $\delta = \delta_2$.

4.3.2 Comparison to Phase-Field Results

We now compare the predictions of our toy model with the numerical simulations presented in §4.1. To directly compare the toy model with our phase-field results, we non-dimensionalise such that $\widetilde{p_c} = \frac{p_c}{\mathcal{E}_{\text{mix}}}$. Dropping the tilde for convenience, we then note that p_c is equal to the confining stress, $\overline{\sigma}$ (Equation 4.14; $\sigma^i = 0$). Figure 4.9 shows $\overline{\sigma}$ as a function of δ via Equations (4.16)–(4.20). Varying both M and p_c^e, we find that the results compare well with the phase-field simulations shown in Figure 4.3: the stress in the plateau region is independent of M but

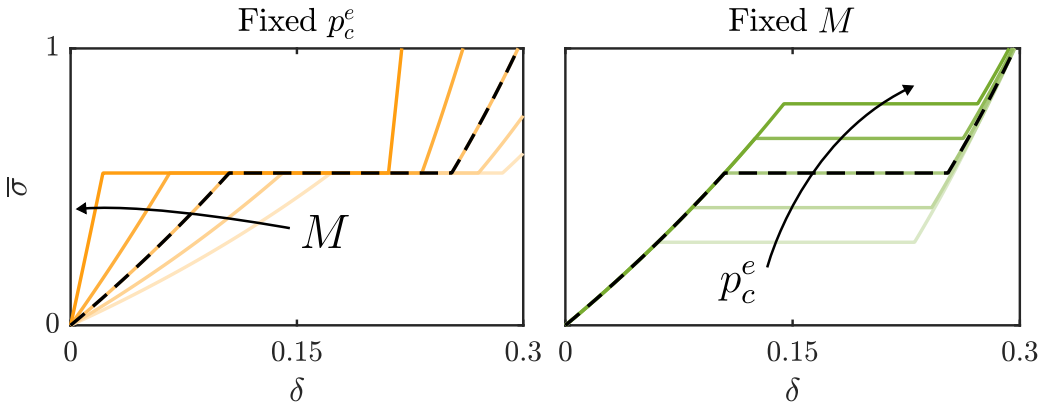

Figure 4.9: Analytical solutions of Equations (4.13)–(4.15) showing $\overline{\sigma}$ as a function of δ. For the left plot, we fix $p_c^e = 1.5$ and show results for $M = 2$, 2.6, 3.6, 6.2 and 20 (light to dark colours). For the right plot, we fix $M = 3$, and vary $p_c^e = 0.3$, 0.425, 0.55, 0.675, 0.8 (light to dark colours). We also set $\phi_0 = 0.5$ and $\Delta_g^0 = 0.2$. The black dashed line corresponds to the same solution in each plot. Compare with the second row of Figure 4.3.

increases with p_c^e, whereas the stiffness of the material increases with M and is independent of p_c^e.

Equation (4.11) above describes how $\overline{\sigma}_{\text{plat}}$ varies with χ_{gs}. In the toy model, the plateau stress is exactly equal to the capillary entry pressure. We can thus write χ_{gs} in terms of natural physical quantities, using Equation (4.17),

$$\chi_{gs} = 2.3 \left[\frac{2\gamma_{gl} \cos \vartheta_c}{\mathcal{E}_{\text{mix}} r_p} \right]^{0.69} . \tag{4.21}$$

We also note that $M = 2G + \Lambda$, where G and Λ are the bulk modulus and Lamé's first parameter, respectively. We use these two expressions to choose parameter values for Figure 4.9 that match those used in Figure 4.3. Finally, we note that although our toy model and phase-field formulation agree well for describing cavity collapse, the former does not capture the meta-stability of cavities. We attribute this to the fact that we have assumed that each phase exists in a 'pure' form in the toy model: gas perfectly displaces pore liquid, and there is no residual gas in the uninvaded region. Residual trapping of the non-wetting fluid is likely to occur in real-world porous media, and thus we expect the non-reversible nature of cavity collapse and re-formation to be an important physical phenomenon.

4.4 Summary

In this chapter, we have investigated the deformation-driven collapse of a single gas cavity via compression with a fluid-permeable piston. Simulations of our phase-field model illustrate the phenomenology of this process. We find that, as confinement increases, gas is forced from the cavity into the pore space, forming a pore-bubble. The confinement required to trigger cavity collapse depends strongly on the strength of the gas–solid interaction parameter, χ_{gs}. If confinement subsequently decreases, the cavity can re-form, with gas separating from the pore space. Note that although we have focused exclusively on the quasi-static limit, our model is also able to capture transient effects.

We find that, in general, a cycle of cavity collapse and re-formation under compression and then decompression is not reversible: the confining stress required to trigger cavity collapse is larger than the confinement at which cavities re-form. We attribute this behaviour to the existence of meta-stable states that allow cavities to persist long after they cease to be the equilibrium state. Finally, we use a simple toy model to connect key phenomenological parameters in our phase-field model to concrete material properties. We find that χ_{gs} correlates strongly with the capillary entry pressure, and that χ_{gl} controls the saturation at which gas from the cavity invades the pore space.

Note that we have focused on cavity collapse via displacement-controlled motion of the confining piston. In this case, it is possible to sequentially advance the piston during cavity collapse in a quasi-static manner. This is the key feature which gives rise to the staircase state observed in §4.1. The control afforded by this procedure may have application to industrial processes which involve the manipulation and storage of hazardous fluids, such as in chemical waste ponds [Kam et al., 2001]. Conversely, many geophysical scenarios are controlled by either an overlying pressure or stress (*e.g.*, for gas venting from marine sediments [Scandella et al., 2011]). We expect cavity collapse due to stress-controlled piston motion to

show markedly different behaviour to that discussed in this chapter; specifically, the long-term persistence of staircase states will not be possible, and cavities will collapse abruptly once the confining stress is reached. A thorough investigation of this process is thus a key direction for future work.

Chapter 5

Cavity Collapse: Experiments

To test the predictions of the theory developed in Chapter 4, we now investigate deformation-driven collapse of cavities in soft porous media experimentally. To focus on the key physical processes that control cavity collapse, we seek an example soft porous medium that has a simple pore geometry and relatively simple mechanical properties. For our example soft porous medium, we use a close packing of hydrogel beads. Hydrogels consist of a cross-linked polymer network swollen in water. The polymer chains which make up hydrogel are hydrophilic in nature, and so it is energetically favourable for water to imbibe into the space between polymers. As hydrogels swell, however, the polymer chains become increasingly stretched, providing an elastic resistance to the further imbibition of water. An equilibrium size is reached when the elastic energy penalty of stretching the polymer network balances the energetic benefit of further water imbibition [Bertrand et al., 2016].

Swollen hydrogel beads are extremely soft (Young's modulus of $\sim 10\,\mathrm{kPa}$) and slippery. In water, hydrogels are essentially transparent and almost perfectly neutrally buoyant. As a result, hydrogels have been used as example soft porous media in a range of recent work [*e.g.* Mukhopadhyay and Peixinho, 2011, Hewitt et al., 2015, 2016, MacMinn et al., 2015, Sutherland and Balmforth, 2019, Dijksman and Mullin, 2022]. Fluid-saturated packings of hydrogel particles have also been

shown to exhibit reproducible elastic behaviour under simple consolidation tests [Mukhopadhyay and Peixinho, 2011], which makes them an appropriate choice of material for our experiments.

In this chapter, we undertake a series of experiments in a custom-built millifluidic set up. We first inject a small amount of air (the non-wetting phase) into a liquid-saturated packing of hydrogels, creating a gas cavity. We then increase or decrease the confinement via a fluid-permeable piston controlled by an actuator. In §5.1, we describe our experimental apparatus and discuss the calibration of various experimental parameters. In §5.2, we undertake experiments to measure the confinement required to trigger cavity collapse, characterise the mechanical response of the porous packing during collapse, and investigate the reversibility of cavity collapse under increasing and then decreasing confinement. Finally, in §5.3, we examine an extended toy model to help explain the results of our experiments.

5.1 Experimental Setup

An overview of our experimental setup is shown in Figure 5.1. We use a close packing of polyacrylamide hydrogel beads (JRM Chemical) as our solid phase. We swell the polyacrylamide beads in a dilute solution of blue food dye (erioglaucine disodium salt) in water. The beads partially exclude the dye, making them lighter in colour than the surrounding water (beads swollen in pure water are colourless and closely index-matched to the water, and thus essentially invisible). The fully swollen beads are $> 99.9\%$ solvent by mass; as such, the solvent is essentially perfectly wetting to the solid relative to almost any other fluid. We use air as the non-wetting phase. Below, we refer to the solvent and the air as 'liquid' and 'gas', respectively.

To constrain our system to uniaxial flow and deformation, we conduct experiments in a long, thin tube (acrylic; length $L = 120\,\mathrm{mm}$ and internal radius $r_t = 2.5\,\mathrm{mm}$).

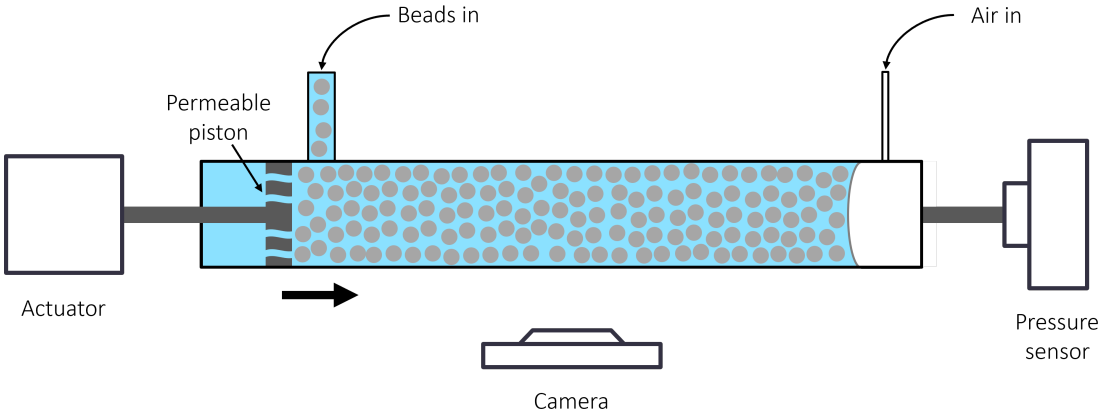

Figure 5.1: The experimental setup, showing uniaxial deformation applied to a model soft porous medium containing a single gas cavity. The experiment is confined within a cylindrical tube of radius $r_t = 2.5\,\mathrm{mm}$ and length $L = 120\,\mathrm{mm}$. The porous medium is a packing of hydrogel beads with mean radii ranging from $r_b = 0.40\,\mathrm{mm}$ to $r_b = 0.63\,\mathrm{mm}$. The liquid is water and the gas is air. We measure the force on the piston, the motion of the packing, and the pressure in the gas cavity via a load cell, a camera, and a pressure transducer, respectively.

The internal diameter of our tube is less than the capillary length for an air–water system by design, such that macroscopic cavities can span the cross-section of the tube and will therefore be essentially one-dimensional. We fill the tube with a mixture of hydrogel beads and water and then inject gas at the right end to form a cavity between the saturated packing and the impermeable right boundary.

We control the confinement with a fluid-permeable piston at the left side of the apparatus. The piston head and shaft are made of PTFE to minimise friction between the piston and tube walls. Motion of the piston is driven by a syringe pump (AL-1010; WPI), which we henceforth refer to as the 'actuator'. We measure the pressure in the gas cavity relative to atmospheric pressure via a pressure transducer (15 psi; 015PGAA5; Honeywell), and the total confining stress via a micro-load cell (100 g; 3139_0; Phidgets) connected in series with the actuator. We record the evolution of the packing and the gas visually with a digital camera (ACA4096-3UM; Basler) at a spatial resolution of 30 pixels per mm and a temporal resolution of 0.5 frames per second. Readings from the load cell and pressure transducer are collected via a LabJack U6 device.

5.1.1 Experimental Protocol and Calibration

We focus on slow (quasi-static), displacement-controlled compression, analogous to the test problem investigated theoretically in Chapter 4. Motion of the permeable piston is controlled by specifying its velocity as a function of time. The piston advances at a uniform speed, $\dot{\delta}$, from an initial position δ_0 until reaching a maximum displacement δ^*. As the piston advances, it compresses the porous medium, with liquid exiting to the left, through the piston. The liquid reservoir to the left of the piston is connected to a fixed hydrostatic head, so that constant liquid pressure is maintained at the left boundary throughout an experiment. At the end of a complete compression sequence, the piston is fully retracted and the tube emptied.

We repeat experiments for different initial cavity size and bead radius. For each set of hydrogel beads used, we first characterise the constitutive response of the solid skeleton by conducting uniaxial compression tests on a liquid-saturated packing (no gas cavity). We measure the effective stress in the packing via the load cell and thereby calculate a corresponding stress-strain relation. Further details and the results of this characterisation procedure are given in Appendix D.1. We determine the size distribution of the swollen hydrogel beads by photographing a monolayer of beads and analysing the resulting images; details and results are provided in Appendix D.2.

5.2 Mechanics of Cavity Collapse

We first consider a single representative experiment to explore the typical phenomenology of cavity collapse. Figure 5.2 shows a series of snapshots from such an experiment. Figure 5.3 shows the associated evolution of the sizes of the cavity, Δ_g, and the invaded region, $\mathcal{B}$. We calculate Δ_g and $\mathcal{B}$ via analysis of experimental images, as detailed in Appendix E. Typically, the bead–liquid mixture initially

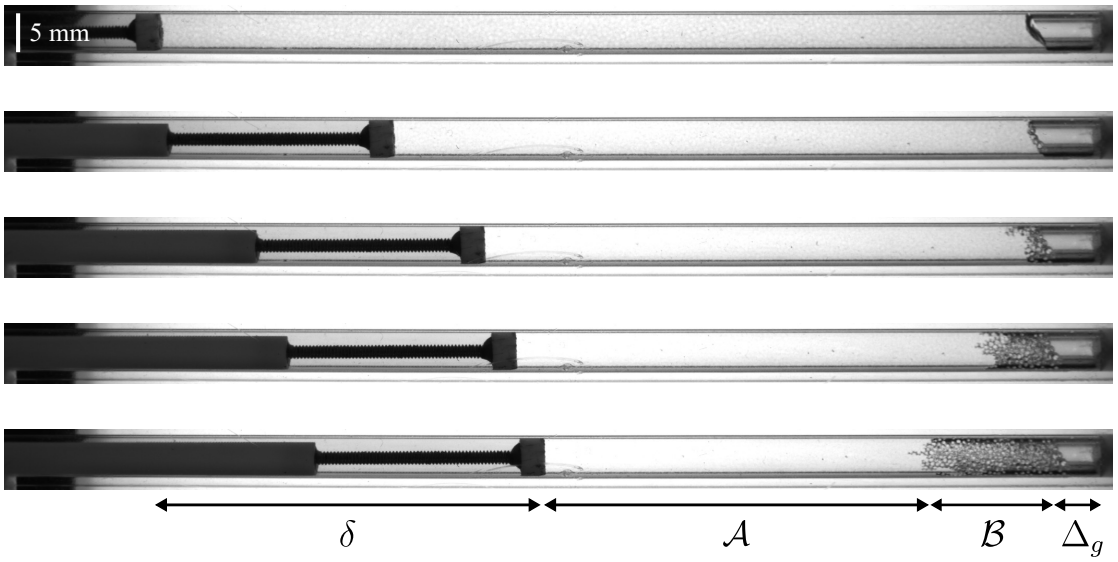

Figure 5.2: A series of experimental snapshots showing the deformation-driven collapse of a gas cavity via compression with a fluid-permeable piston. The hydrogel beads used in this experiment have a mean radius of $r_b = 0.48\,\mathrm{mm}$. The piston speed is $\dot{\delta} = 0.5\,\mathrm{mm/min}$ and the compression sequence shown here took ~ 1 hour.

injected into our experimental apparatus is sub-isostatic, meaning that there are insufficient bead–bead contacts to support an applied force; this initial mixture may be considered a dense suspension rather than a compact porous medium. As a result, we shift our experimental results such that $\delta = 0$ corresponds to the point at which the packing is first able to support force (when p_c first increases above zero), at which point it can be considered to be a relaxed porous medium.

Initially, the gas cavity and liquid-saturated porous medium are separated by a gas–liquid meniscus that spans the cross-section of the tube. As the piston advances and confinement increases, this interface begins to invade the narrow pore throats between hydrogel beads. This results in the formation of many small menisci between individual beads. As confinement increases further, gas is eventually able to invade the pore space, displacing liquid. Gas invasion continues as the piston continues to advance, with the size of the gas cavity decreasing as a result. Eventually, the last of the gas invades the pore space and the cavity vanishes. At this point, the solid packing is in direct physical contact with the impermeable right boundary. Further motion of the piston is equivalent to uniaxial compression

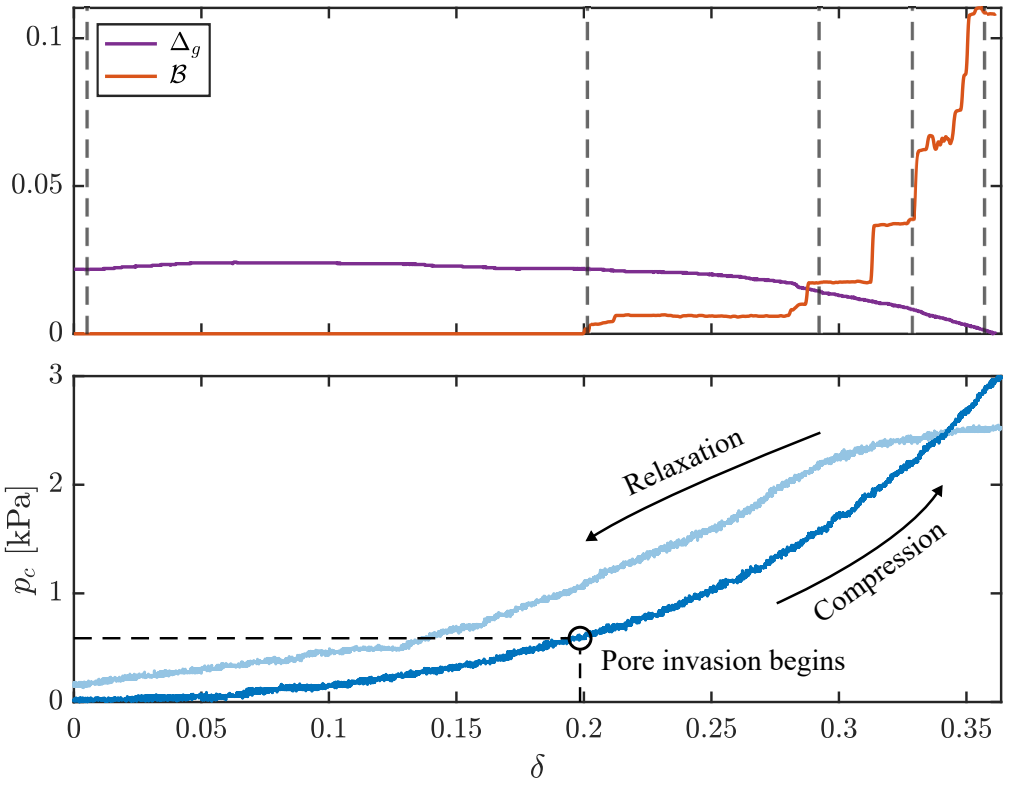

Figure 5.3: Top: non-dimensional cavity size, Δ_g, (purple) and size of the invaded region, $\mathcal{B}$, (orange) as functions of non-dimensional piston position, δ, during cavity collapse for the experiment shown in Figure 5.2. Δ_g and $\mathcal{B}$ are calculated via analysis of experimental images, as detailed in Appendix E. The vertical dashed lines correspond to the snapshots shown in Figure 5.2. Bottom: capillary pressure, p_c, as a function of δ during one compression-relaxation cycle for the experiment shown in Figures 5.2 (compression, dark blue) and 5.4 (relaxation, light blue). The dashed black lines highlight the values of δ and p_c at which pore invasion first occurs during compression.

of an unsaturated, deformable porous medium (without cavities).

As demonstrated in Figure 5.3, gas invasion proceeds in a series of bursts in our experiments, unlike the smooth, continuous invasion suggested by our model. The size of each burst event is typically between one and five bead diameters. We attribute this feature to inhomogeneity in the pore space of the porous medium. Even for perfectly spherical, monodisperse solid grains, the solid skeleton will consist of a random arrangement of pores and throats. As a result, the gas–liquid menisci encounter local variations in pore size and throat size as they propagate through the packing. In particular, the menisci will become 'stuck' at smaller pore

throats until gas pressure increases sufficiently for the interface to burst through to the next local constriction. This burst-like behaviour is a standard feature of quasi-static drainage in a rigid porous medium [Blunt, 2017]. Neither our phase-field model derived in Chapter 2 nor our toy model derived in Chapter 4 predict this burst-like behaviour, as both assume a uniform pore structure. Burst-like gas invasion could be introduced to these models by incorporating random spatial variations to χ_{gs} and r_p, respectively. Despite the burst-like invasion of the gas–liquid interface within the pore space, the size of the cavity, Δ_g, decreases relatively smoothly. This result is due to gas displacing residual liquid within the invaded region between burst events, increasing gas saturation in this region.

Figure 5.3 also shows the evolution of pressure in the gas cavity during cavity collapse, as a function of piston position. The liquid phase is held at near-atmospheric pressure throughout the experiment, so the measured gas pressure is equal to the capillary pressure, p_c. As confinement increases, the capillary pressure increases as the porous medium is compressed. Prior to gas invasion, the pressure-displacement profile is dictated by the elastic properties of the hydrogel packing. Once p_c reaches the capillary entry pressure, gas is able to invade the pore space. Recall that the theory detailed in Chapter 4 predicts a plateau in the confining stress (and thus also capillary pressure) during pore invasion; however our experimental measurements do not share this feature. Instead, the measured capillary pressure increases steadily and monotonically with the amount of compression. We attribute this behaviour to a combination of stress relaxation in the hydrogel packing, and deformation-dependent pore closure, as discussed in detail in §5.3.4 below.

5.2.1 Stress Relaxation

Once a compression sequence is complete, we continue to record the experiment whilst the piston remains stationary for a short period (approximately one tenth of

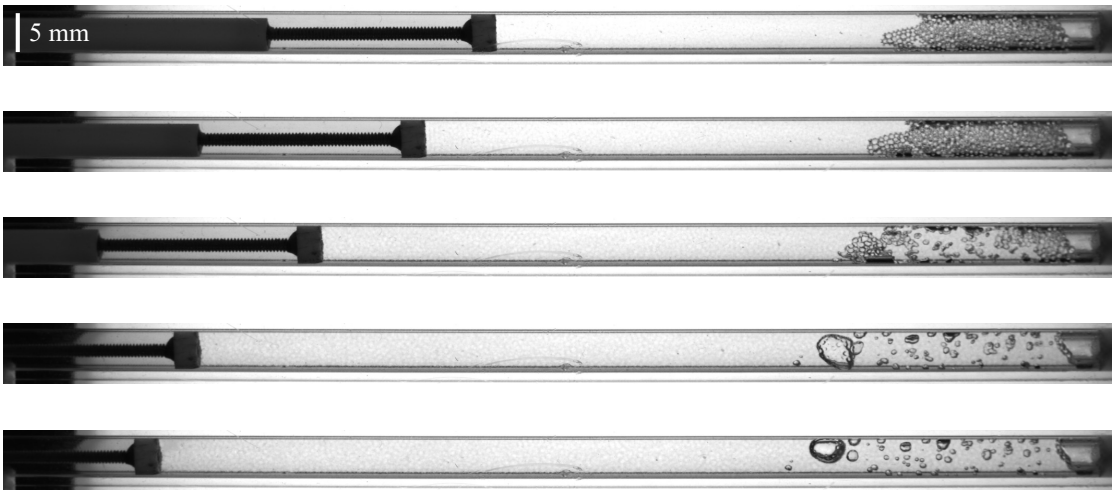

Figure 5.4: A series of experimental snapshots showing the partial re-formation of a cavity as confinement is reduced. These snapshots are from the same experiment as those in Figure 5.4, with the piston held stationary for 10 minutes between the final panel of Figure 5.4 and the first panel of this figure. A small amount of gas redistribution occurs in this waiting time as a result of stress relaxation in the hydrogel packing.

the time taken for compression). During this time, both the capillary pressure and the confining stress decrease by about 10%. Similar stress-relaxation behaviour has been observed in previous studies with packings of hydrogel beads [Dijksman and Mullin, 2022]. This behaviour is most likely caused by the partial de-swelling, relaxation, and rearrangement of the hydrogel beads under applied confinement. Stress relaxation results in a small amount of further gas motion, as the invaded gas phase rearranges within the pore space to accommodate the new stress and pressure.

5.2.2 Reversibility of Collapse

In addition to deformation-driven cavity collapse, we also investigate the reversibility of cavity collapse during decompression. Once the piston reaches its maximum displacement, we pause for about 10 minutes and then retract it to its initial position at the same speed. As discussed in §4.2, we expect a reduction in confining stress to result in cavities being able to re-form. Figure 5.4 shows snapshots of an experiment as the piston retracts. Figure 5.3 shows the capillary pressure as

a function of δ during retraction, demonstrating that capillary pressure decreases as the piston retracts.

As confinement decreases, gas initially remains fixed in place, with only minimal rearrangement of its distribution in the pore space. As the piston retracts further, however, gas starts to exit the pore space and form small cavities throughout the porous medium (middle to bottom panels of Figure 5.4), eventually resulting in a series of small cavities along the entire previously invaded region of the porous medium. Note that these cavities are typically too small to span the cross-section of the tube. The formation of several small cavities instead of one large cavity is a result of individual pinch-off events during decompression. As the gas invades and then occupies the tortuous pore space between hydrogel beads, individual blobs of gas may pinch off from the previously connected gas domain, forming a series of small, disconnected pore-bubbles. As confinement then decreases, many of these individual pore-bubbles leave the pore space separately, forming a number of small gas cavities. Note also that cavity re-formation occurs at a smaller confinement than that required to trigger cavity collapse, as predicted in §4.2.

5.2.3 Influence of Bead Size

We now investigate the influence of bead radius, r_b, on our experimental results. Figure 5.5 shows the capillary pressure during cavity collapse for three different sets of hydrogel beads. For each set of beads, the experiment was repeated at least 5 times. The solid black lines in Figure 5.5 show the mean capillary pressure from these repeats. Coloured bands show a variation of one standard deviation from the mean value. To account for small variations in the initial packing length between experiments, we re-scale δ by the length of the packing at $\delta = 0$. For different experiments, the initial size of the cavity, Δ_g^0, varied slightly. This variation does not notably affect the results shown in Figure 5.5, as variations in Δ_g^0 are much smaller than typical variations due to other effects.

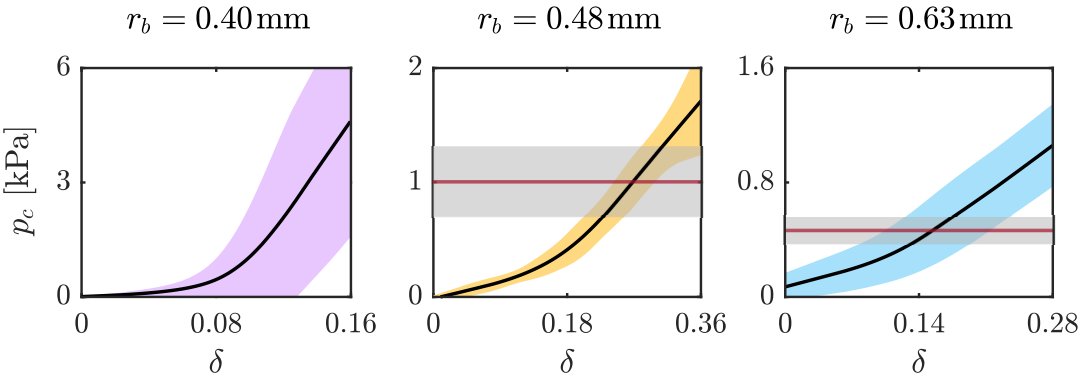

Figure 5.5: Experimental results showing p_c as a function of δ for $r_b = 0.40\,\mathrm{mm}$, $0.48\,\mathrm{mm}$ and $0.63\,\mathrm{mm}$ (left to right). Bead size is calculated as detailed in Appendix D.2. Each experiment was repeated at least 5 times for each bead size. The black lines show the mean of each set of repeats, with the coloured bands indicating one standard deviation around the mean. Horizontal red lines show the mean capillary pressure at the onset of pore invasion, with grey bands indicating one standard deviation around this mean. Note the different pressure scales for each value of r_b. For the smallest bead size (left panel), we do not observe pore invasion.

For $r_b = 0.95\,\mathrm{mm}$ and $1.25\,\mathrm{mm}$ (middle and right panels of Figure 5.5), we observe the dynamics shown in Figure 5.2. Initially, the hydrogel packing is increasingly compressed and p_c increases, until, eventually, gas invades the pore space and the cavity collapses with further piston displacement. The value of p_c at the point of first pore invasion is denoted p_c^e. The mean and standard deviation of p_c^e are shown by the red lines, and respective grey bands, in Figure 5.5. Our results suggest that p_c^e is higher for $r_b = 0.48\,\mathrm{mm}$ than for $r_b = 0.63\,\mathrm{mm}$, consistent with the Young-Laplace law.

For $r_b = 0.40\,\mathrm{mm}$ (left panel of Figure 5.5), we do not see pore invasion in the vast majority of our experiments. Instead, p_c continues to increase much past the expected value of $p_c^e \sim 1.4\,\mathrm{kPa}$. Eventually, as p_c becomes very large, the cavity begins to shrink due to compression of the gas. We attribute this 'clogging' behaviour to deformation-driven pore closure. Entry pressure scales as r_p^{-1}, where r_p is the characteristic size of a pore throat (Equation 1.2). As r_p decreases due to the compression of the packing, p_c^e will increase. If r_p decreases sufficiently strongly with δ, it may be possible for p_c^e to increase more quickly than p_c, making

it impossible for the gas to invade the pore space. We discuss this phenomenon further in §5.3.2 in the context of an extended toy model.

5.3 Extended Toy Model

Motivated by our experimental observations, we now consider the effect of several additional physical mechanisms not included in our previous theoretical work: compressibility of the gas phase, deformation-driven pore closure, and frictional drag at the domain walls. We investigate these phenomena by extending our toy model (§4.3.1), and comparing the predictions of this model to experimental results where appropriate. A full derivation of the extended toy model is presented in Appendix F. In §5.3.1–5.3.3 below, we highlight the key changes to the simple toy model of §4.3.1 as a result of each additional physical effect.

5.3.1 Gas Compressibility

Throughout this thesis, we have assumed that both fluid phases are incompressible. In the experiments presented above (and indeed in many natural systems) the non-wetting fluid is gas, which in reality is highly compressible in many practical scenarios. In general, the assumption of incompressibility is valid when typical variations in gas pressure are small relative to the absolute gas pressure. For quasi-static cavity collapse, we expect the size of pressure variations to be roughly equal to the capillary entry pressure of the solid skeleton. Once the capillary pressure exceeds the entry pressure, gas will invade the pore space rather than further displacing solid grains. Thus, if the entry pressure is sufficiently small in comparison to the ambient pressure of the liquid, pore invasion will occur before any significant compression of the gas takes place. If capillary entry pressure is sufficiently large on the other hand, gas compressibility may be significant.

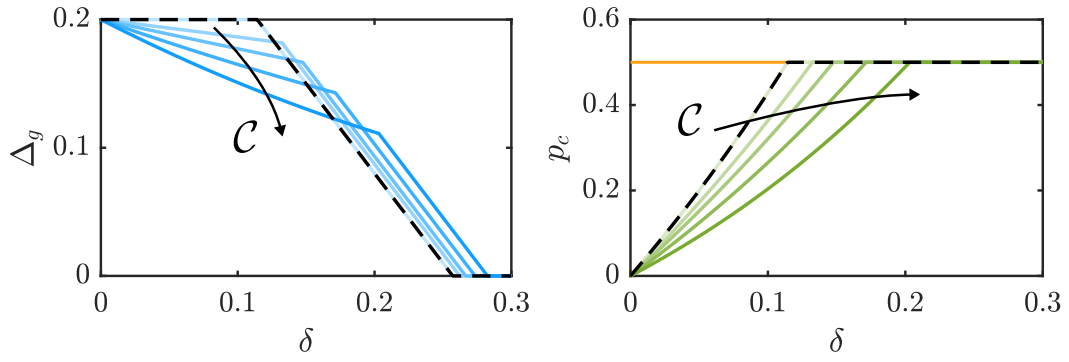

Figure 5.6: Results of the extended toy model demonstrating the effect of gas compressibility on deformation-driven cavity collapse. We plot cavity size (blue) and capillary pressure (green) as functions of piston position, δ, for $\mathcal{C} = 0$, 0.1, 0.2, 0.4, 0.8 (light to dark). The orange line shows the capillary entry pressure and the dashed black lines show the incompressible limit ($\mathcal{C} = 0$). Other parameter values are $p_c^{e,0} = 0.5$, $M = 3$ and $\Delta_g^0 = 0.2$.

To account for compressibility, we assume that gas obeys Boyle's law and that it remains isothermal, such that $p_g V_g$ is constant for a gas volume V_g. Assuming that liquid pressure is fixed at atmospheric pressure, $p_l = p_{\text{atm}}$, and that $p_c = 0$ when $\delta = 0$, conservation of mass for gas (Equation 4.13a) then becomes

$$\Delta_g + \mathcal{B}\phi_0 = \frac{\Delta_g^0}{1 + \mathcal{C}p_c/p_c^{e,0}}, \tag{5.1}$$

where $\mathcal{C} = \frac{p_c^{e,0}}{p_{\text{atm}}}$ is a dimensionless 'compressibility' and $p_c^{e,0} = \frac{2\gamma_{gl}\cos\vartheta_c}{r_p^0}$ is the capillary entry pressure at $\delta = 0$ for an initial pore size r_p^0. The rest of the model is unchanged from §4.3.1.

Figure 5.6 shows the effect of varying $\mathcal{C}$ on Δ_g and p_c during cavity collapse. We use the same model set up as in §4.3.1, with a fluid-permeable piston advancing from $\delta = 0$ to a maximum displacement δ^*. The incompressible limit is given by $\mathcal{C} = 0$ (dashed black lines). As $\mathcal{C}$ increases, we see that cavity size decreases *before* p_c reaches p_c^e (orange line) as the gas is increasingly compressed, increasingly delaying pore invasion relative to the incompressible case. Once gas invades the pore space, p_c is constant and no further gas compression takes place; Δ_g continues to decrease, but now as a result of pore invasion rather than gas compression.

5.3.2 Deformation-Dependent Pore Closure

For a porous medium comprising incompressible solid grains, compression results in a decrease in the pore volume and, thus, the expulsion of a corresponding volume of fluid. This effect is a key aspect of poroelasticity and is captured in all theoretical models discussed in this thesis. As porosity decreases, the local spaces between individual solid grains must clearly also decrease. The capillary pressure is set by the size of these pore throats, so it reasonable to expect that compression of the porous medium should correspond to an increase in the capillary entry pressure. We have neglected this effect thus far for simplicity, but it appears to be important in our particular experimental system. We model deformation-dependent entry pressure by letting r_p, the radius of a typical pore throat, be a simple function of strain, $\mathcal{S}$. We assume a linear dependence for simplicity, such that

$$r_p = r_p^0(1 + \tau\mathcal{S}), \tag{5.2}$$

where τ is a dimensionless constant. Recall that $\mathcal{S}$ is negative for compression. A more complex form of $r_p(\mathcal{S})$ can be found by considering in detail the geometry of a given porous medium as it changes under compression, but we expect this simple model to capture the key features.

Figure 5.7 shows the effect of a deformation-dependent entry pressure on deformation-driven cavity collapse. For $\tau = 0$, the entry pressure (orange lines) remains constant as δ increases. For $\tau > 0$, however, p_c^e increases with δ. As a result, pore invasion is delayed, as gas must be increasingly pressurised in order to reach the entry pressure. Once gas invades the pore space, p_c remains constant regardless of τ because the solid skeleton does not become further deformed, and strain remains constant.

A key result of deformation-dependent entry pressure is that it is possible for p_c^e to increase sufficiently quickly that gas is never able to invade the pore space. This 'self-clogging' behaviour is seen for $\tau = 1.6$ in Figure 5.7, with p_c^e diverging as

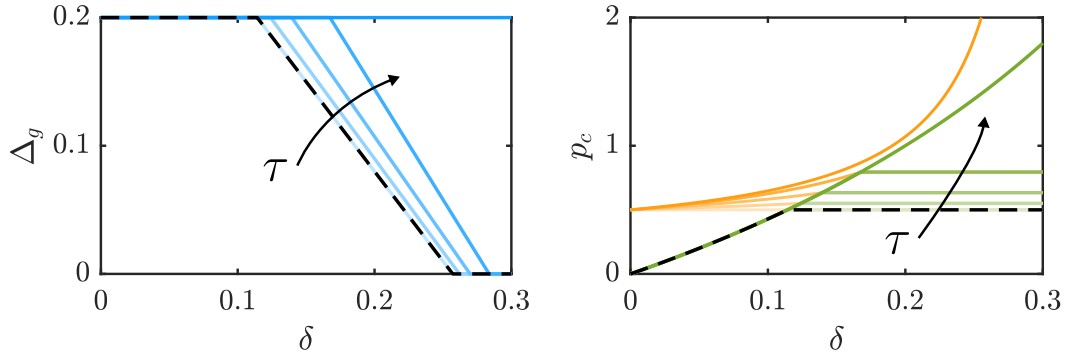

Figure 5.7: Results of the extended toy model with deformation-dependent pore closure, showing Δ_g and p_c as functions of δ for $\tau = 0,\ 0.5,\ 1,\ 1.4,\ 1.6$ (light to dark). The orange line shows the capillary entry pressure, and the dashed black lines highlight the limiting case $\tau = 0$. For $\tau = 1.6$, p_c never reaches p_c^e and gas never invade the pore space. Other parameter values are $p_c^{e,0} = 0.5$, $M = 3$, $\mathcal{C} = 0$ and $\Delta_g^0 = 0.2$.

δ increases. As a result, p_c is always less than p_c^e and Δ_g remains equal to Δ_g^0. Equating Equations (4.14), (4.17) and (5.2), we find that the p_c^e is found by solving

$$(p_c^e)^2 - \frac{M}{\tau} p_c^e + \frac{M}{\tau} p_c^{e,0} = 0. \tag{5.3}$$

Self-clogging occurs when Equation (5.3) has complex solutions. A condition for self-clogging is then given by

$$\omega_c > 1, \tag{5.4}$$

where $\omega_c = \frac{4 p_c^{e,0} \tau}{M}$ is the 'clogging number'. As noted above, we observe self-clogging for experiments with bead radius $r_b = 0.40\,\text{mm}$, suggesting that $\omega_c > 1$ for the parameters used in those experiments. In practice, even when self-clogging occurs, cavity size will decrease, as p_c becomes large enough that gas compression is no longer negligible.

5.3.3 Wall Friction

Swollen hydrogel beads consist of 99.9% water by mass, and so are extremely slippery. Despite this, frictional effects may still be important in highly confined

systems such as the apparatus used here. The primary cause of this phenomenon is the Janssen effect, in which normal stresses are redirected into a perpendicular plane in granular materials [Janssen, 1895]. The result of this stress redirection is that, as the porous medium is increasingly compressed, an increasingly large stress will be redirected against the walls of the confining tube. According to Coloumb's friction law, the frictional drag between the porous medium and the walls is given by

$$\sigma_F = -C_F \sigma'_{\varrho\varrho}, \tag{5.5}$$

where C_F is the coefficient of friction and $\sigma'_{\varrho\varrho}$ is the effective normal stress in the radial direction at the tube walls. Even for a very low coefficient of friction (small C_F), frictional effects will therefore become important for large values of $\sigma'_{\varrho\varrho}$.

The effect of friction in our toy model is that force balance (Equation 4.14) becomes

$$\sigma^u = \frac{p_c}{\mathcal{A}\mathcal{J}} \left[1 - \exp(\mathcal{J}\mathcal{A})\right], \tag{5.6}$$

where $\mathcal{J} = \frac{C_F K_J}{r_t}$ is a dimensionless measure of the strength of friction, with K_J the Janssen coefficient quantifying the amount of stress redirection, r_t the radius of the confining tube, and we recall that σ^u is the effective stress in the uninvaded region. A full derivation of Equation (5.6), following the works of Marks et al. [2015] and Morrow et al. [2023b], is provided in Appendix F.1. The key result of this derivation is that frictional drag depends exponentially on the length of the uninvaded region, $\mathcal{A}$. We note that the invaded region of the porous medium does not contribute to the total frictional stress because we have taken the porous medium to be relaxed in this region. The effect of friction on the predictions of our toy model are shown in Figure 5.8. As $\mathcal{J}$ increases, pore invasion is delayed due to an increasing proportion of the confining stress being supported by wall friction, rather than by gas pressure. As a result, gas is less pressurised relative to the no-friction limit, and so a larger confinement is required for p_c to reach p_c^e. Once gas invades the pore space, p_c remains constant throughout cavity collapse.

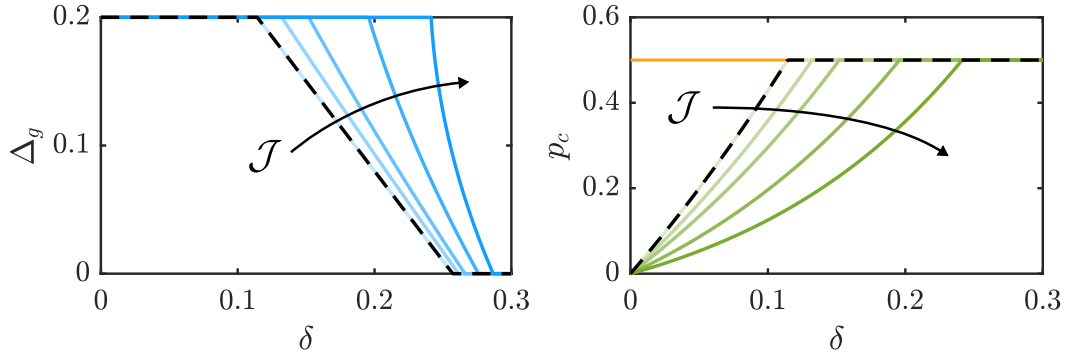

Figure 5.8: Results of the extended toy model with friction, showing Δ_g and p_c as functions of δ for $\mathcal{J} = 0.001,\ 0.5,\ 1,\ 2,\ 3$ (light to dark). The orange line shows the capillary entry pressure, and the dashed black lines highlight the limiting case $\mathcal{J} \to 0$. Other parameter values are $p_c^{e,0} = 0.5$, $M = 3$, $\mathcal{C} = 0$, $\tau = 0$, and $\Delta_g^0 = 0.2$.

5.3.4 Comparison to Experimental Results

To quantitatively compare the predictions of our toy model to experimental results, we first calculate values of the relevant dimensionless constants from experimental parameters. Calculated values of M and r_b for our experiments are given in Appendix D. We estimate the entry pressure at $\delta = 0$ by using the Young-Laplace law, $p_c^{e,0} = \frac{2\gamma_{gl}\cos\vartheta_c}{r_p^0}$, assuming that $2r_p^0 \sim r_b$ (*i.e.*, that the typical radius of a pore throat is half the mean bead radius). Water–air surface tension at room temperature is $\gamma_{gl} = 72\,\mathrm{mN/m}$ and we assume $\cos\vartheta_c = 1$ because the liquid phase is almost perfectly wetting to the hydrogel beads in our experiments. To calculate values of $\mathcal{C}$ and $\mathcal{J}$, we use $p_{\mathrm{atm}} = 101\,\mathrm{kPa}$, $C_F \sim 0.01$ [Cuccia et al., 2020], $K_J \sim 1$ [Ovarlez and Clément, 2005], and $r_t = 2.5\mathrm{mm}$. These values suggest that $\mathcal{J} \sim 1$, and $\mathcal{C} \sim 0.005$. Assuming that τ is independent of bead size, we then estimate $\tau \sim 1$, as this provides the best match with our experimental results. In the parameter regime considered in our experiments, we thus expect deformation-driven pore closure and wall friction to be important, but gas compression to be negligible unless the system clogs.

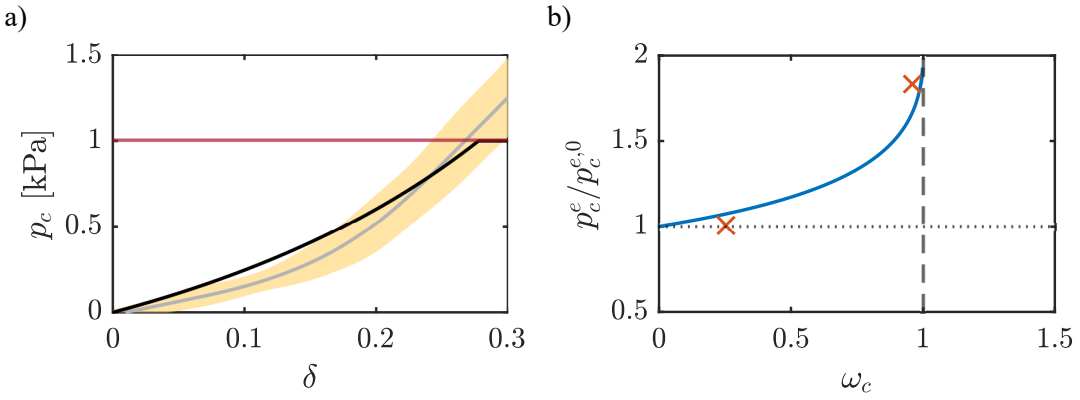

Figure 5.9: (a) Comparison between predictions of our toy model (black curve) and experimental results, showing p_c as a function of δ for $r_b = 0.48\,\mathrm{mm}$. The grey curve shows the mean value of p_c over all experiments and the yellow band shows one standard deviation either side of this mean. The horizontal red line shows the mean capillary entry pressure from the experiments. In the toy model, we set $\phi_0 = 0.37$, $\mathcal{C} = 0.005$, $\tau = 1$, $\mathcal{J} = 1$ and $\Delta_g^0 = 0.2$. (b) Comparison between solutions of Equation (5.3) (blue curve) and experimental results (crosses), showing entry pressure, p_c^e, normalised by $p_c^{e,0}$ as a function of clogging number, ω_c. The red crosses show experimental results for $r_b = 0.63\,\mathrm{mm}$ ($\omega_c = 0.25$) and $0.48\,\mathrm{mm}$ ($\omega_c = 0.96$). The dashed vertical line shows $\omega_c = 1$, which demarcates the transition from pore invasion to self-clogging. The dotted horizontal line shows $p_c^e = p_c^{e,0}$ (limit of $\tau \to 0$). For $r_b = 0.40\,\mathrm{mm}$ ($\omega_c = 1.37$), pore invasion does not occur, so p_c^e is undefined. We use the same parameter values as for (a) in our toy model.

Figure 5.9 shows a comparison between our experimental results and the predictions of our toy model. In Figure 5.9a, we plot capillary pressure, p_c, as a function of δ for $r_b = 0.48\,\mathrm{mm}$. As δ increases, p_c also increases until it reaches the entry pressure, $p_c^e \sim 1\,\mathrm{kPa}$, at which point gas invades the pore space. Our experimental results and toy model show this threshold being reached at similar values of δ. Similar comparisons can be made for the other bead sizes shown in Figure 5.5. In Figure 5.9b, we plot p_c, normalised by p_c^e, as a function of the clogging number, ω_c. A value of $\tau = 1$ provides the best fit between predictions of this model and our experiments. Note that, although the parameter value $\tau = 1$ and the ratio $\frac{r_b}{r_p^0} = 2$ have been chosen to give the best comparison between our model and experimental results, both values are consistent with order-of-magnitude estimates, and that we have no physical reason to apply further constraints on their value.

As ω_c increases, the normalised entry pressure also increases, as expected; ω_c represents the degree to which the entry pressure is able to increase as a result of deformation-dependent pore closure. As discussed in §5.3.2, self-clogging occurs when $\omega_c > 1$. For our experiments with $r_b = 0.40\,\mathrm{mm}$, we calculate $\omega_c = 1.37$, and so we expect the system to clog. This is indeed what happens, as demonstrated in Figure 5.5. In the absence of pore closure, p_c^e always equals $p_c^{e,0}$. Our experimental results clearly demonstrate that this is not the case, and so deformation-driven pore closure must be important in this system.

The key difference between our theory and experiments is that for the toy model (and indeed numerical simulations of our phase-field model), p_c remains constant once gas invasion begins. In our experiments, in contrast, p_c increases steadily and smoothly throughout cavity collapse. Although we sometimes see an inflection in $p_c(\delta)$ at pore invasion, the measured capillary pressure continues to increase beyond this. We attribute this behaviour to stress relaxation in the hydrogel packing. As highlighted in §5.2.1, hydrogel beads show stress relaxation under constant deformation, as a result of partial de-watering of the swollen polymer network. By the same mechanism, constant stress leads to a creep response [Dijksman and Mullin, 2022]. Once gas invades the pore space, the gas–liquid interface continues to apply stress to the uninvaded region of the hydrogel packing. Even if this stress remains constant (as might be expected from our toy model), the hydrogels in the uninvaded region will begin to slowly de-water, and their mean bead size will shrink. As a result, the beads will be able to pack more densely, and the relaxed porosity of the packing, ϕ_0, will decrease. As ϕ_0 decreases, the size of the pore throats will decrease and the capillary entry pressure will increase, as discussed in §5.3.2.

5.4 Summary

In this chapter, we have described a series of table-top experiments to investigate the deformation-driven collapse of gas cavities. Using a packing of hydrogel beads as an example soft porous medium, we study the basic evolution of cavity collapse. As a cavity collapses, gas invades the pore space in a burst-like manner, but remains within a compact region in the pore space. We find that the confining stress required to trigger pore invasion increases with decreasing bead size. For sufficiently small hydrogel beads, we find that gas is in fact unable to invade the pore space due to the deformation-driven closure of pore throats. An extension of our previous toy model indicates the existence of a critical 'clogging number', the value of which determines whether gas is able to invade the pore space or if the packing will instead 'self-clog'. We also find the effect of frictional drag between the hydrogel beads and the walls of the apparatus to be important in our experimental system, delaying the onset of pore invasion.

Our experimental results also show that capillary pressure continues to increase once pore invasion has occurred. This result is in contrast to the predictions of our theories in Chapter 4, where we observed a stress plateau after initial pore invasion. We hypothesise that this discrepancy is due to stress relaxation within the packing, with a corresponding decrease in porosity at fixed stress, coupled with the deformation-driven closure of pore throats. Stress relaxation could be incorporated into our toy model by modelling a visco-elastic rheology for the solid. Additional experiments could test our hypothesis by investigating faster piston motion, so that the timescale of stress relaxation is much longer than the timescale of the experiment. An associated challenge is that, as piston speed increases, the quasi-static approximation may no longer be valid, and dynamic poroelastic effects may become important. Many natural porous media are subject to periodic loading conditions [*e.g.*, Scandella et al., 2011, Fiori et al., 2023], and so further experiments could focus on repeated compression–decompression cycles, and the

associated cavity collapse and re-formation. For these experiments, it will be important to form cross–section-spanning cavities during decompression. Using a confining tube with a smaller internal diameter could potentially achieve this effect.

Chapter 6

Conclusions and Future Work

A key feature of two-phase flow in a deformable porous medium is the ability of the non-wetting phase to form open cavities within the solid skeleton. In this thesis, we have studied the formation and collapse of non-wetting cavities in soft (elastically deformable) porous media. We have derived a thermodynamically consistent phase-field model that describes the formation of cavities as a result of fluid–fluid–solid phase separation, and have explored our model in the context of two test problems in a one-dimensional setting. In addition, we have performed a series of simple table-top experiments to test the predictions of our model. This work lays the groundwork for various exciting future developments, as detailed in §6.1 below.

Our model, presented in Chapter 2, assumes incompressible, immiscible fluids, which interact with a hyperelastic solid skeleton. The different interactions between phases are characterised by relevant free energy functions. Our model makes use of a phenomenological free energy. Although such an approach is useful for understanding the key physical processes that control this complex, multiphase system, developing a rigorous free energy in terms of natural physical quantities represents a key avenue for future study. Detailed upscaling of the pore-scale thermodynamics of a fluid–fluid–solid mixture could provide this link. How to formulate such a procedure, however, remains unclear.

In the three well-studied limiting cases of no-solid, no-gas and no-deformation, our model reproduces the expected behaviour. When no solid is present, we reproduce the fluid–fluid phase separation and coarsening behaviour characteristic of the Cahn–Hilliard equation. When no gas is present, our model gives a diffuse-interface formulation of single-phase Biot poroelasticity, whose results match well with analytical solutions to the traditional sharp-interface approach. Finally, when the solid skeleton is rigid, our model reduces to previous phase-field descriptions of two-phase flow in rigid porous media.

In the full three-phase system, non-wetting cavities are able to spontaneously form from an initially homogeneous pore-space distribution of fluid, with the non-wetting phase separating from the solid skeleton, as studied in Chapter 3. Relative to fluid–fluid phase separation in an unconstrained domain, we find that phase separation is inhibited by elastic resistance from the solid, which imposes limits on the conditions under which cavities form: if the solid skeleton is too stiff, the non-wetting fluid will remain within the pore space. We have shown how the onset of phase separation depends on different parameters, including the deformability of the solid matrix and the wetting characteristics of the two fluids, via numerical simulation, linear stability analysis and analytical solution of a reduced model. We have also shown that, for a softer porous material, we expect smaller, but more numerous, cavities than for a stiffer porous material, owing to a smaller amount of non-wetting fluid needing to accumulate within the pore space in order to open a cavity in the former case. Despite this, we find that the total cavity volume is larger for a softer porous medium, as the solid skeleton is more easily deformed by the non-wetting phase.

Our work has been partially motivated by the venting of gas from non-cohesive granular sediments, in which the compressibility of the gas phase can be neglected when the capillary entry pressure of the granular skeleton is sufficiently small compared to the ambient liquid pressure. Our model is also relevant for different fluid pairs in other contexts, such as phase-separating liquid droplets in polymer

networks [Style et al., 2018, Rosowski et al., 2020a, Fernández-Rico et al., 2023]. In polymer systems, the porous skeleton does not have a granular microstructure and the energy required to fracture the polymer network when opening a cavity has an important impact on the final size of droplets [Kim et al., 2020, Vidal-Henriquez and Zwicker, 2021, Ronceray et al., 2022]. Our model can capture fluid–fluid phase separation in 1D within such materials through an appropriate choice of the Griffith fracture energy. We also note that while we have solved our model assuming a neo-Hookean elastic response for the solid skeleton, our theory allows for other elastic laws relevant to the system being studied.

Cavities are only able to form if the solid skeleton is sufficiently soft and/or if the confining stress is sufficiently low. An increase in confining stress can thus trigger the collapse of cavities, forcing the non-wetting fluid into the pore space. We have studied cavity collapse via both numerical simulation of our phase-field model (Chapter 4) and experiments with an example soft porous medium (Chapter 5). We find that the non-wetting fluid remains compact as it invades the pore space, with constant saturation in the invaded region. As a result, we observe a 'staircase' state during cavity collapse, in which there is coexistence between three distinct mixture compositions. We find that the stability of three-state coexistence depends strongly on the presence of a ternary interaction term in our free energy. When this ternary term is not included, the non-wetting phase instead spreads diffusively through the porous medium during cavity collapse.

We have investigated how cavity collapse depends on different model parameters, using a simple toy model to connect phenomenological phase-field parameters with concrete material properties. We find that, as the capillary entry pressure of the solid skeleton increases, the confining stress required to trigger cavity collapse correspondingly increases. As the deformability of the solid skeleton increases, the amount of deformation required to achieve this confining stress also increases. We have demonstrated the possibility of cycles of successive cavity collapse and

re-formation as a result of increasing and then decreasing confining stress. Typically, this process is not reversible: cavity re-formation is delayed relative to cavity collapse due to the persistence of meta-stable states. Although we have focused exclusively on quasi-static cavity collapse, our model is also able to capture transient responses resulting from faster piston motion. Similarly, we have only considered displacement-controlled deformation, in which the position of the confining piston is specified for all times. We anticipate that a study of force-controlled cavity collapse, in addition to an investigation of transient behaviour, will produce further interesting results.

In our experiments, we use swollen hydrogel beads as a model system with which to study the collapse of a gas cavity due to compression via a fluid-permeable piston. We find the same underlying behaviour as in our theoretical work: once confining stress reaches a threshold value, gas invades the pore space, remaining compact as it does so. If confinement subsequently decreases, gas may leave the pore space to form a series of smaller cavities, rather than the single large cavity that was originally present. The confinement required to trigger cavity collapse increases as the size of solid grains decreases. For sufficiently small solid grains, we also find that gas may be unable to invade the pore space at all. We attribute this feature to a deformation-dependent entry pressure that results from the progressive closure of individual pore throats as the solid skeleton is increasingly deformed.

Our numerical simulations and toy model predict that confining stress remains constant once the gas invades the pore space, but we do not see this stress plateau in our experimental results. Instead, the confining stress in experiments increases smoothly and steadily throughout cavity collapse. This discrepancy arises from additional physical effects that are not included in our idealised continuum model; namely, friction between solid grains and the walls of the apparatus, deformation-driven pore-closure, and stress relaxation. Extending our phase-field formulation to incorporate these effects is a clear avenue for future work.

6.1 Future Work

In this thesis, we have studied the spontaneous formation and deformation-driven collapse of non-wetting cavities in elastically deformable porous media, for incompressible, immiscible fluids in 1D. Even within this framework, there remains significant scope for future work. Most notably, the development of a more representative free energy which accurately captures the energetic landscape of a fluid–fluid–solid mixture in terms of concrete physical quantities is a key step in being able to apply our model to real-world scenarios. Our experimental results also highlight the importance of additional physical effects, even in the most simple of settings. Extending our phase-field model to capture the effects of frictional drag, deformation-dependent entry pressure, stress relaxation, and heterogeneity of the pore space represents a relatively straightforward, but nonetheless important, step in being able to faithfully reproduce experimental observations.

Although considering a 1D system is useful for making physically meaningful predictions of real-world behaviours, the extra degree(s) of freedom arising from 2D and 3D systems can allow for novel behaviour not possible in 1D. Developing 2D (or 3D) simulations for comparison to complementary experiments would thus dramatically increase the range of physical problems that could be studied, as discussed further in §6.1.1. While simplified constitutive behaviours, such as a cohesion-less elastic solid and incompressible, immiscible fluids, are reasonable assumptions in many settings, in reality most biological and geophysical systems are more complex. The effects of inter-grain cohesion or an elasto-plastic solid rheology could be captured naturally within our current framework through a history-dependent damage function [Miehe et al., 2010a] and an appropriate choice of free energy [Houlsby and Puzrin, 2010], respectively. On the other hand, incorporating compressible and/or partially miscible fluids is likely to be more challenging, as detailed in §6.1.2 below.

6.1.1 2D Systems

Despite the additional conceptual and computational complexity, developing 2D simulations represents a key step in building on the work undertaken in this thesis. Initial numerical simulations could be simplified by considering a linearised version of our model. The reduction of our model to a linearly elastic constitutive response for the solid skeleton is straightforward. The suitability of representing open cavities (in which the solid fraction goes to zero) by a linearised kinematic framework, however, is unclear.

A natural starting point for exploring our model in 2D is to consider the direct injection of non-wetting fluid into a solid skeleton saturated with the wetting phase. The single-phase equivalent of this problem has been widely studied [*e.g.,* Auton and MacMinn, 2017, 2018] as a result of direct applications to industrial processes such as hydraulic fracturing. Similarly, multiphase fluid injection into rigid and inelastic porous media has been studied in a variety of different contexts. A key feature of multiphase fluid injection in 2D is the range of complex displacement patterns that are observed, resulting from viscous instability [Homsy, 1987], frictional forces [Sandnes et al., 2011], cohesive forces in the solid skeleton [Guével et al., 2023], or combinations of these effects. We expect simulations of non-wetting fluid injection into a soft porous medium to demonstrate many of these patterns, as well as additional features specific to this system. Complementary experiments for simulations of such a process could involve the radial injection of fluid into a planar packing of hydrogel beads, as previously studied by MacMinn et al. [2015] for the single-phase case.

Studying spontaneous cavity formation in 2D is also an exciting direction for future work. The key difference here relative to a 1D system is that cavities will have a two-dimensional shape. As a result, the curvature of inter-phase boundaries will control the size and shape of cavities that form through interfacial contributions to the free energy. In 1D, the influence of interfacial energy is restricted to controlling

the width of the diffuse interface between different phases. In 2D, however, the energetic cost of forming curved interfaces will affect the final size of cavities, and potentially suppress their formation altogether. Uniaxial compression tests (both numerical and experimental) on a porous medium containing a distribution of non-wetting cavities would inform predictions of the mechanical properties of offshore foundations [Liu et al., 2022]. The mechanical response observed in a 2D system may differ substantially from that observed in a 1D setting. In 2D, the solid skeleton will be able to support force chains which bypass the non-wetting cavities, thus reducing the impact of cavities on uniaxial deformations of the porous medium. Conversely, we expect resistance to shear deformations to be significantly reduced by the presence of cavities [Kaminski et al., 2019].

The effect of a background fluid flow on a porous medium containing a distribution of cavities also represents an exciting direction for future work. Flow-driven deformation of a soft porous medium results in a non-uniform stress field along the flow direction [MacMinn et al., 2016]. As demonstrated in Chapters 4 and 5, an increase in stress can trigger cavity collapse. A non-uniform stress field thus raises the possibility of cavity collapse in some parts of the domain, but not in others. The prospect of cavity localisation via flow-driven deformation has potential application to industrial process such as the storage of hazardous chemicals in waste ponds [Kam et al., 2001].

Finally, 2D simulations could be used to reproduce the recent experiments of Lee et al. [2020]. In these experiments, buoyant bubbles of non-wetting gas are injected into the base of a soft granular medium, highlighting how different gas migration mechanisms are possible for different confining stresses. Relative buoyancy of the fluid phases can be naturally included in our model through the addition of a gravitational potential to the free energy, thus allowing further investigation of this system.

6.1.2 Model Extensions

In this thesis, we have focused on the formation and collapse of non-wetting cavities when both fluid phases are incompressible. This assumption is reasonable when the capillary entry pressure of the solid skeleton is sufficiently small compared to the ambient fluid pressure. However, for many natural systems in which the non-wetting phase is gas, this assumption may be inappropriate. For example, for methane bubbles in mud and clay sediments, where grain sizes are on the order of microns, compressibility will likely be important. Recent works have shown how compressibility of an injected fluid can lead to dramatic changes in the observed dynamics [Sandnes et al., 2011, Cuttle and MacMinn, 2023, Cuttle et al., 2023, Morrow et al., 2023a]. Extending such an analysis to fluid injection in a deformable porous medium would have direct relevance to industrial processes such as CO_2 sequestration [Vilarrasa et al., 2010].

The framework used to derive our phase-field model in Chapter 2 requires local phase densities to be constant, such that conservation laws are expressed in terms of the volume fractions of each phase. To account for compressibility of one (or both) of the fluid phases, the model will most likely need to be reformulated in terms of mass fractions rather than volume fractions. Such a reformulation will complicate the details of the derivation, but an outline for how to derive such a model is given in the work of Oden et al. [2010]. The constitutive response of the compressible fluid can be captured through the addition of an appropriate contribution to the total free energy [Dai et al., 2022].

In practice, most fluids in natural biological and geophysical systems are not completely immiscible, but instead show partial miscibility. A key contributor to the release of greenhouse gases in underwater sediments is the exsolution of these gases from the saturating fluid. Similarly, extending our model to account for partial miscibility of the fluid phases would more readily facilitate the study of fluid–fluid phase separation in biological cells and synthetic gels [Hyman et al., 2014, Style

et al., 2018, Fernández-Rico et al., 2022]. Previous phase-field models of partially miscible fluids have focused on fluid–fluid systems only [Fu et al., 2016, 2017]. In these works, an additional phase-field order parameter, the concentration, must be introduced to account for the dissolution and exsolution of species from one phase to another. This behaviour is typically modelled by the Allen-Cahn equation [Allen and Cahn, 1979]. Successfully generalising this approach to a deformable porous system within the rigorous thermodynamic framework of Gurtin [1996], represents a significant modelling challenge.

The key distinction between immiscible and partially miscible fluids in the context of non-wetting cavities is the ability of a non-wetting cavity to dissolve into the surrounding wetting fluid. This promotes the possibility of thermodynamic coarsening, which is otherwise suppressed. Dissolution of the non-wetting phase may result in partial (or complete) cavity collapse, with the dissolved species then exsolving into remaining cavities. Previous experimental and theoretical studies have demonstrated that the presence of an elastic network can inhibit coarsening [Rosowski et al., 2020a, Kothari and Cohen, 2020], but an extended poromechanical model would allow the dynamics of this process to be more thoroughly investigated.

6.2 Outlook

Overall, the work contained in this thesis provides a detailed investigation of the behaviour of non-wetting cavities in soft porous media, focusing on incompressible, immiscible fluids. As well as providing fundamental physical insight into multiphase flow through soft porous media, the results of this work have direct application to important real-world problems, such as the venting of greenhouse gases from seabeds and peatlands [Skarke et al., 2014, Chen and Slater, 2015, Lee et al., 2020] and the formation of biomolecular condensates in the cellular matrix [Hyman et al., 2014, Vidal-Henriquez and Zwicker, 2021]. In particular, we

have highlighted the need to differentiate between non-wetting fluid which remains within the pore space and that which forms open cavities, especially when assessing macroscopic mechanical properties of a given material. Whilst our experimental results highlight the need for further modelling efforts to be able to capture the full complexity of any natural physical system, the theories developed in this thesis provide a vital platform for doing so and represent a significant development on previous work in this field.

Appendix A

Further Details of Model Derivation

A.1 Solid Mechanics

As noted in §2.1.4, our system displays distinct mechanical behaviours depending on whether the material is in tension or compression. As such, we must identify when each regime occurs. Following the approach of Tang et al. [2019], we first rewrite the neo-Hookean strain-energy density in terms of the principal stretches, λ_i,

$$\mathcal{W}_{el} = \frac{1}{2}G\sum_{i=1}^{3}\left(\lambda_i^2 - 1 - 2\log\lambda_i\right) + \frac{1}{2}\Lambda\left(\log J\right)^2, \tag{A.1}$$

where we have used that $J = \lambda_1\lambda_2\lambda_3$. The first part of this expression corresponds to straining deformations and the second part to volumetric deformations. We then decompose this strain-energy function into tensile and compressive parts, given by $\mathcal{W}^+ = \mathcal{W}_{el}\left(\lambda_i^+, J^+\right)$ and $\mathcal{W}^- = \mathcal{W}_{el}\left(\lambda_i^-, J^-\right)$, respectively. We define $\lambda_i^\pm$ and $J^\pm$ as piecewise functions, with

$$\lambda_i^+ = \begin{cases} 1 & \text{for } \lambda_i \leq 1, \\ \lambda_i & \text{for } \lambda_i > 1, \end{cases} \qquad J^+ = \begin{cases} 1 & \text{for } J \leq 1, \\ J & \text{for } J > 1 \end{cases} \tag{A.2}$$

and

$$\lambda_i^- = \begin{cases} \lambda_i & \text{for } \lambda_i < 1, \\ 1 & \text{for } \lambda_i \geq 1, \end{cases} \qquad J^- = \begin{cases} J & \text{for } J < 1, \\ 1 & \text{for } J \geq 1. \end{cases} \tag{A.3}$$

As per Equations (2.22), the tensile part of the elastic energy, $\mathcal{W}^+$ is degraded by an increase in the damage parameter.

The effective stress, $\boldsymbol{\sigma}'$, is found by taking the derivative of the elastic free energy (Equation 2.29),

$$\boldsymbol{\sigma}' = g(d)\,\frac{1}{J}\frac{\partial \mathcal{W}^+}{\partial \mathbb{F}} \cdot \mathbb{F}^\intercal + \frac{1}{J}\frac{\partial \mathcal{W}^-}{\partial \mathbb{F}} \cdot \mathbb{F}^\intercal. \tag{A.4}$$

Using the chain rule, we have that (following Tang et al. [2019]),

$$\frac{\partial \mathcal{W}^+}{\partial F_{ij}} = \sum_{k=1}^{3} \frac{\partial \mathcal{W}^+}{\partial \lambda_k^+}\frac{\partial \lambda_k^+}{\partial F_{ij}} + \frac{\partial \mathcal{W}^+}{\partial J^+}\frac{\partial J^+}{\partial F_{ij}}, \quad \frac{\partial \mathcal{W}^-}{\partial F_{ij}} = \sum_{k=1}^{3} \frac{\partial \mathcal{W}^-}{\partial \lambda_k^-}\frac{\partial \lambda_k^-}{\partial F_{ij}} + \frac{\partial \mathcal{W}^-}{\partial J^-}\frac{\partial J^-}{\partial F_{ij}}, \tag{A.5}$$

where

$$\frac{\partial \lambda_k^+}{\partial F_{ij}} = \begin{cases} 0 & \text{for } \lambda_k \leq 1, \\ \frac{\partial \lambda_k}{\partial F_{ij}} & \text{for } \lambda_k > 1, \end{cases} \qquad \frac{\partial \lambda_k^-}{\partial F_{ij}} = \begin{cases} \frac{\partial \lambda_k}{\partial F_{ij}} & \text{for } \lambda_k < 1, \\ 0 & \text{for } \lambda_k \geq 1, \end{cases} \tag{A.6a}$$

$$\frac{\partial J^+}{\partial F_{ij}} = \begin{cases} 0 & \text{for } J \leq 1, \\ \frac{\partial J}{\partial F_{ij}} & \text{for } J > 1, \end{cases} \qquad \frac{\partial J^-}{\partial F_{ij}} = \begin{cases} \frac{\partial J}{\partial F_{ij}} & \text{for } J < 1, \\ 0 & \text{for } J \geq 1 \end{cases} \tag{A.6b}$$

and

$$\frac{\partial \mathcal{W}^+}{\partial \lambda_k^+} = G\left(\lambda_k^+ - \frac{1}{\lambda_k^+}\right), \qquad \frac{\partial \mathcal{W}^-}{\partial \lambda_k^-} = G\left(\lambda_k^- - \frac{1}{\lambda_k^-}\right), \tag{A.7a}$$

$$\frac{\partial \mathcal{W}^+}{\partial J^+} = \Lambda\frac{\log J^+}{J^+}, \qquad \frac{\partial \mathcal{W}^-}{\partial J^-} = \Lambda\frac{\log J^-}{J^-}. \tag{A.7b}$$

This constitutive law reduces to a standard neo-Hookean behaviour in the case of an undamaged system ($d = 0$).

The solid mechanics of our system greatly simplify in the uniaxial case, as described in §2.1.6. In 1D, $\mathbf{u}_s = u_s(x,t)\,\hat{\mathbf{e}}_x$, and hence using Equation (2.2), we see that the

deformation gradient tensor is diagonal, with

$$\mathbb{F}^{-1} = \begin{pmatrix} 1 - \frac{\partial u_s}{\partial x} & 0 & 0 \\ 0 & 1 & 0 \\ 0 & 0 & 1 \end{pmatrix}. \tag{A.8}$$

Noting that $J = \det(\mathbb{F})$, we thus write that

$$\mathbb{F} = \begin{pmatrix} J & 0 & 0 \\ 0 & 1 & 0 \\ 0 & 0 & 1 \end{pmatrix}. \tag{A.9}$$

In this case, the principal stretches λ_i are the eigenvalues of the deformation gradient, and so only one of these stretches $\lambda = \lambda_1 = J$ is non-constant in this system. As such, the neo-Hookean strain-energy can be written solely in terms of J, and we can identify tension as being when $J > 1$. The above constitutive behaviour (Equation A.4) thus simplifies to

$$\sigma'_{xx} = g(d)\frac{\partial \mathcal{W}^+}{\partial J} + \frac{\partial \mathcal{W}^-}{\partial J}, \tag{A.10}$$

with the tensile and compressive components of the free energy defined as,

$$\mathcal{W}^+ = \begin{cases} 0 & \text{for } J \leq 1, \\ \mathcal{W}^0_{el} & \text{for } J > 1, \end{cases} \tag{A.11}$$

and

$$\mathcal{W}^- = \begin{cases} \mathcal{W}^0_{el} & \text{for } J < 1, \\ 0 & \text{for } J \geq 1, \end{cases} \tag{A.12}$$

respectively, where $\mathcal{W}_{el}^0 = \frac{1}{2}G\left(J^2 - 1 - 2\log J\right) + \frac{1}{2}\Lambda\left(\log J\right)^2$. Undertaking the differentiation of the free energy with respect to J then gives

$$\sigma'_{xx} = \begin{cases} \sigma'_0\left(\phi\right) & J \leq 1, \\ \sigma'_0\left(\phi\right) g\left(d\right) & J > 1, \end{cases} \tag{A.13}$$

where σ'_0 is the undamaged neo-Hookean stress, given by,

$$\sigma'_0 = G\left(J - \frac{1}{J}\right) + \Lambda\frac{\log J}{J}. \tag{A.14}$$

To complete our description of the mechanics, we link J to the porosity, ϕ, using Equation (2.4).

A.2 Capillary Potential

To formulate explicit expressions for the capillary potentials, we start by substituting the free energy of the system into Equation (2.26b). The liquid and gas potentials contain three distinct parts,

$$\Psi_\alpha = \frac{\partial\psi_{\text{bulk}}}{\partial\varphi_\alpha} + \frac{\partial\psi_{\text{mix}}}{\partial\varphi_\alpha} - \nabla_0 \cdot \left(\frac{\partial\psi_{\text{interface}}}{\partial\nabla_0\varphi_\alpha}\right), \tag{A.15}$$

each associated with different components of the free energy. The free energy is written in §2.1.4 as a function of Eulerian variables, ϕ_α and ∇, whereas the capillary potential is defined in terms of derivatives with respect to Lagrangian variables, φ_α and ∇_0. We thus use the relations $\varphi_\alpha = \phi_\alpha J$, $\nabla = \mathbb{F}^{-\intercal} \cdot \nabla_0$, and $J = \varphi_s^0 + \varphi_g + \varphi_l$ to give

$$\Psi_g = \rho_g\mu_g^0 + \Pi_g - \gamma_1\nabla^2\phi_g - \frac{\gamma_3}{2}\nabla^2\phi_l, \tag{A.16a}$$

$$\Psi_l = \rho_l\mu_l^0 + \Pi_l - \gamma_2\nabla^2\phi_l - \frac{\gamma_3}{2}\nabla^2\phi_g, \tag{A.16b}$$

where we have further defined the interaction potentials, Π_α, as the component of the capillary potential resulting from the differentiation of ψ_{mix}. These are given by:

$$\Pi_g = \mathcal{E}_{\text{mix}} \left[\log \phi_g + \phi_s + (1 - \phi_g) \left(\chi_{gl} \phi_l + \chi_{gs} \phi_s \right) + \chi_{gsl} \phi_s \phi_l (1 - 2\phi_g) \right], \quad \text{(A.17a)}$$

$$\Pi_l = \mathcal{E}_{\text{mix}} \left[\log \phi_l + \phi_s + \phi_g \left(\chi_{gl} (1 - \phi_l) - \chi_{gs} \phi_s \right) + \chi_{gsl} \phi_g \phi_s (1 - 2\phi_l) \right]. \quad \text{(A.17b)}$$

For incompressible, immiscible fluids, $\rho_\alpha \mu_\alpha^0$ is constant. In our model, the capillary potential only appears as the argument of a gradient function, and so this constant bulk term has no effect on the overall state of the system and can be ignored. The spatial derivatives in the capillary potentials resist the formation of sharp gradients in volume fraction, and serve to regularise the system by preventing the formation of shocks in the gas fraction and porosity.

A.3 Korteweg Stress

In order to derive an explicit expression for the Korteweg stress, we first consider the free energy of a general interface between two unspecified phases, α and β, using the form given in Equation (2.24),

$$\psi_{\alpha\beta} = \frac{\gamma}{2} \left(\nabla \phi_\alpha \cdot \nabla \phi_\beta \right) J. \quad \text{(A.18)}$$

As derived in §2.1.5, the Korteweg stress has two distinct contributions, which we denote $\mathbb{K}_1$ and $\mathbb{K}_2$, where,

$$\mathbb{K}_1 = \frac{1}{J} \frac{\partial \psi_{\text{interface}}}{\partial \mathbb{F}} \cdot \mathbb{F}^\intercal, \qquad \mathbb{K}_2 = - \left(\nabla_0 \cdot \frac{\partial \psi_{\text{interface}}}{\partial \nabla_0 J} \right) \mathbb{I}. \quad \text{(A.19)}$$

In order to carry out this differentiation, we write $\psi_{\alpha\beta}$ in terms of Lagrangian quantities. Using the conversions $\varphi_\alpha = \phi_\alpha J$ and $\nabla = \mathbb{F}^{-\intercal} \cdot \nabla_0$, we rewrite the

interfacial free energy as,

$$\psi_{\alpha\beta} = \frac{\gamma}{2J^3}\left[J\nabla_0\varphi_\alpha - \varphi_\alpha\nabla_0 J\right]\cdot\mathbb{C}^{-1}\cdot\left[J\nabla_0\varphi_\beta - \varphi_\beta\nabla_0 J\right], \tag{A.20}$$

where $\mathbb{C} = \mathbb{F}^\intercal\mathbb{F}$ is the right Cauchy-Green tensor. We can then differentiate Equation (A.20) to find the Korteweg stress. Note that we carry out the derivative of J with respect to $\mathbb{F}$ using Jacobi's formula, $\frac{\partial J}{\partial \mathbb{F}} = J\mathbb{F}^{-\intercal}$. The result is

$$\mathbb{K}_1 = -\frac{\gamma}{2}\left[\nabla\phi_\alpha\otimes\nabla\phi_\beta + \nabla\phi_\beta\otimes\nabla\phi_\alpha + (\nabla\phi_\alpha\cdot\nabla\phi_\beta)\,\mathbb{I}\right] \tag{A.21}$$

and

$$\mathbb{K}_2 = \frac{\gamma}{2}\left(2\nabla\phi_\alpha\cdot\nabla\phi_\beta + \phi_\alpha\nabla^2\phi_\beta + \phi_\beta\nabla^2\phi_\alpha\right)\mathbb{I}, \tag{A.22}$$

where $\otimes$ is the tensor product, and we have converted back to Eulerian variables. Combining these two expressions gives the total Korteweg stress resulting from an $\alpha-\beta$ interface,

$$\mathbb{K}_{\alpha\beta} = \frac{\gamma}{2}\left(\nabla\phi_\alpha\cdot\nabla\phi_\beta + \phi_\alpha\nabla^2\phi_\beta + \phi_\beta\nabla^2\phi_\alpha\right)\mathbb{I} - \frac{\gamma}{2}\left(\nabla\phi_\alpha\otimes\nabla\phi_\beta + \nabla\phi_\beta\otimes\nabla\phi_\alpha\right). \tag{A.23}$$

The three types of interface in our system are gas–gas, liquid–liquid and gas–liquid. The Korteweg stress is then the sum of the contributions from these interfaces,

$$\begin{aligned}\mathbb{K} = {}& \gamma_1\left(\frac{1}{2}|\nabla\phi_g|^2+\phi_g\nabla^2\phi_g\right)\mathbb{I}-\gamma_1\nabla\phi_g\otimes\nabla\phi_g+\gamma_2\left(\frac{1}{2}|\nabla\phi_l|^2+\phi_l\nabla^2\phi_l\right)\mathbb{I}-\gamma_2\nabla\phi_l\otimes\nabla\phi_l \\ &+\frac{\gamma_3}{2}\left(\nabla\phi_g\cdot\nabla\phi_l+\phi_g\nabla^2\phi_l+\phi_l\nabla^2\phi_g\right)\mathbb{I}-\frac{\gamma_3}{2}\left(\nabla\phi_g\otimes\nabla\phi_l+\nabla\phi_l\otimes\nabla\phi_g\right).\end{aligned} \tag{A.24}$$

In 1D, only the xx-component of $\mathbb{K}$ is relevant, and is given by

$$\begin{aligned}K_{xx} = {}& \gamma_1\left[\phi_g\frac{\partial^2\phi_g}{\partial x^2} - \frac{1}{2}\left(\frac{\partial\phi_g}{\partial x}\right)^2\right] + \gamma_2\left[\phi_l\frac{\partial^2\phi_l}{\partial x^2} - \frac{1}{2}\left(\frac{\partial\phi_l}{\partial x}\right)^2\right] \\ &+ \frac{1}{2}\gamma_3\left[\phi_g\frac{\partial^2\phi_l}{\partial x^2} + \phi_l\frac{\partial^2\phi_g}{\partial x^2} - \frac{\partial\phi_l}{\partial x}\frac{\partial\phi_g}{\partial x}\right].\end{aligned} \tag{A.25}$$

This expression for the Korteweg stress is used in the uniaxial system described in §2.1.6.

A.4 Model Summary

In this appendix we present a summary of the governing equations derived in our model. We note that gas, liquid, and solid volume fractions are related by $\phi_g + \phi_l + \phi_s = 1$. All quantities in this appendix are dimensional. Conservation of mass can be written

$$\frac{\partial \phi_g}{\partial t} + \nabla \cdot (\phi_g \mathbf{q}) + \nabla \cdot \left[(1 - \phi_g) \mathbf{w}_g - \phi_g \mathbf{w}_l \right] = 0, \tag{A.26a}$$

$$\frac{\partial \phi}{\partial t} + \nabla \cdot (\phi \mathbf{q}) + \nabla \cdot \left[(1 - \phi) (\mathbf{w}_g + \mathbf{w}_l) \right] = 0, \tag{A.26b}$$

$$\nabla \cdot \mathbf{q} = 0, \tag{A.26c}$$

where $\phi = \phi_g + \phi_l$ is the porosity. The relative fluid fluxes are given by

$$\mathbf{w}_\alpha = -\phi_\alpha \mathcal{M}_\alpha^0 \nabla \left(p + \Psi_\alpha \right), \tag{A.27}$$

where pressure gradients are balanced by a sum of elastic and Korteweg stresses,

$$\nabla p = \nabla \cdot \left(\boldsymbol{\sigma}' + \mathbb{K} \right). \tag{A.28}$$

For our specific choice of free energy, the capillary potentials are

$$\Psi_g = \rho_g \mu_g^0 + \Pi_g - \gamma_1 \nabla^2 \phi_g - \frac{\gamma_3}{2} \nabla^2 \phi_l, \tag{A.29a}$$

$$\Psi_l = \rho_l \mu_l^0 + \Pi_l - \gamma_2 \nabla^2 \phi_l - \frac{\gamma_3}{2} \nabla^2 \phi_g, \tag{A.29b}$$

where the interaction potentials are

$$\Pi_g = \mathcal{E}_{\text{mix}} \left[\log \phi_g + \phi_s + (1 - \phi_g) \left(\chi_{gl} \phi_l + \chi_{gs} \phi_s \right) + \chi_{gsl} \phi_s \phi_l (1 - 2\phi_g) \right], \tag{A.30a}$$

$$\Pi_l = \mathcal{E}_{\text{mix}} \left[\log \phi_l + \phi_s + \phi_g \left(\chi_{gl}(1-\phi_l) - \chi_{gs}\phi_s \right) + \chi_{gsl}\phi_g\phi_s(1-2\phi_l) \right]. \quad \text{(A.30b)}$$

The effective stress is given by

$$\boldsymbol{\sigma}' = g\left(d\right) \frac{1}{J} \frac{\partial \mathcal{W}^+}{\partial \mathbb{F}} \cdot \mathbb{F}^\intercal + \frac{1}{J} \frac{\partial \mathcal{W}^-}{\partial \mathbb{F}} \cdot \mathbb{F}^\intercal, \quad \text{(A.31)}$$

with $g\left(d\right) = \left[\left(1-\Theta\right)\left(1-d\right)^2 + \Theta \right]$ and where $\frac{\partial \mathcal{W}^\pm}{\partial \mathbb{F}}$ for a neo-Hookean solid skeleton is given in Equations (A.5)–(A.7). The Korteweg stress is given by

$$\begin{aligned} \mathbb{K} = \gamma_1 \left(\frac{1}{2}|\nabla\phi_g|^2 + \phi_g\nabla^2\phi_g \right) \mathbb{I} - \gamma_1 \nabla\phi_g \otimes \nabla\phi_g + \gamma_2 \left(\frac{1}{2}|\nabla\phi_l|^2 + \phi_l\nabla^2\phi_l \right) \mathbb{I} - \gamma_2 \nabla\phi_l \otimes \nabla\phi_l \\ + \frac{\gamma_3}{2} \left(\nabla\phi_g \cdot \nabla\phi_l + \phi_g\nabla^2\phi_l + \phi_l\nabla^2\phi_g \right) \mathbb{I} - \frac{\gamma_3}{2} \left(\nabla\phi_g \otimes \nabla\phi_l + \nabla\phi_l \otimes \nabla\phi_g \right). \quad \text{(A.32)} \end{aligned}$$

The damage parameter, d, evolves according to

$$\left[4 l_d \left(1 - \Theta^{-1} \right) \mathcal{W}^+ + \mathcal{G}_c \right] \left(1-d\right) + 4\mathcal{G}_c l_d^2 \nabla_0^2 d = \mathcal{G}_c, \quad \text{(A.33)}$$

where $\mathcal{W}^\pm$ are defined in Appendix A.1. We link deformation to porosity via $\mathbb{F} = \left(\mathbb{I} - \nabla \mathbf{u}_s\right)^{-1}$ and $J = \det(\mathbb{F}) = \frac{1-\phi_0}{1-\phi}$. Finally, in Eulerian coordinates, the solid velocity is given by $\mathbf{v}_s = \mathbb{F} \cdot \frac{\partial \mathbf{u}_s}{\partial t}$.

Appendix B

Analytical Solution to Sharp-Interface Poroelasticity

To find a steady-state solution to the sharp-interface model described in §2.2.2, we first note that the porosity is described by a piecewise function,

$$\phi(x) = \begin{cases} 1 & x < \delta, \\ f(x) & \delta \leq x \leq 1. \end{cases} \tag{B.1}$$

To find an analytical solution for $f(x)$, we solve Equation (2.50) over the domain $x \in [\delta(t), 1]$, subject to the boundary conditions $\sigma_0'(\delta) = 0$ and $w_l(1) = Q_0$. Following Appendix D of MacMinn et al. [2016], we start by defining two indefinite integrals,

$$\mathcal{I}_1\{\phi\} = \mathcal{D}\int \mathcal{M}(\phi)\frac{\mathrm{d}\sigma_0'}{\mathrm{d}\phi}\mathrm{d}\phi, \tag{B.2}$$

$$\mathcal{I}_2\{\phi\} = \mathcal{D}\int \left(\frac{\phi-\phi_0}{1-\phi}\right)\mathcal{M}(\phi)\frac{\mathrm{d}\sigma_0'}{\mathrm{d}\phi}\mathrm{d}\phi. \tag{B.3}$$

For the mobility law $\mathcal{M} = \phi$ and the elasticity law defined in Equation (2.42), these integrals can be evaluated exactly:

$$\mathcal{I}_1\{\phi\} = \left(\frac{1+\varsigma}{1-\phi_0}\right)\frac{\phi^2}{2} + (1-\phi_0)\left[\frac{\phi}{1-\phi} + \log(1-\phi)\right] - \frac{\varsigma}{4(1-\phi_0)}\left[\phi^2 + 2\phi + 2\log(1-\phi) - 2\phi^2\log\left(\frac{1-\phi}{1-\phi_0}\right)\right], \quad \text{(B.4)}$$

$$\mathcal{I}_2\{\phi\} = -\left(\frac{\phi_0}{1-\phi_0}\right)\mathcal{I}_1\{\phi\} + \left(\frac{1+\varsigma}{(1-\phi_0)^2}\right)\frac{\phi^3}{3} + \left[\phi + \frac{1}{1-\phi} + 2\log(1-\phi)\right] - \frac{\varsigma}{18(1-\phi_0)^2}\left[6\phi + 3\phi^2 + 2\phi^3 + 6\phi^3\log\left(\frac{\phi_0-1}{\phi-1}\right) + 6\log(1-\phi)\right]. \quad \text{(B.5)}$$

Note that the constants of integration to do not contribute to the overall solution, so can be neglected. Using Equation (2.50) and the definitions of $\mathcal{I}_1$ and $\mathcal{I}_2$, it can be shown that

$$\mathcal{I}_2\{\phi(1)\} - \mathcal{I}_1\{\phi(1)\} + \mathcal{I}_1\{\phi(\delta)\} - \mathcal{I}_2\{\phi(\delta)\} = Q_0\mathcal{D}. \quad \text{(B.6)}$$

The boundary condition that the packing is stress-free at the left boundary becomes $\phi(\delta) = \phi_0$, and Equation (B.6) then becomes an implicit expression for $\phi(1)$. It can also be shown that

$$\delta = \frac{1}{Q_0\mathcal{D}}\left[\mathcal{I}_2\{\phi(1)\} - \mathcal{I}_2\{\phi_0\}\right], \quad \text{(B.7)}$$

which gives an explicit expression for δ. Finally,

$$\mathcal{I}_1\{f(x)\} - \mathcal{I}_1\{\phi_0\} = Q_0\mathcal{D}(\delta - x) \quad \text{(B.8)}$$

gives an implicit expression for $f(x)$, which can be solved for numerically.

Appendix C

Linear Stability Coefficients

In §3.2, we introduce the functions $\mathcal{H}_{\alpha\beta}$ and the parameters $\mathcal{N}_{\alpha\beta}$ as coefficients in our linearised evolution equations (Equations 3.4). To find explicit forms for these coefficients, we first define $\mathcal{H}_\alpha$ as the homogeneous part of the chemical potential of fluid α, given by

$$\mathcal{H}_g = \log\phi_g + 1 - \phi + (1-\phi_g)\left[\chi_{gl}\left(\phi-\phi_g\right) + \chi_{gs}\left(1-\phi\right)\right] + \chi_{gsl}\left(\phi-\phi_g\right)\left(1-\phi\right)\left(1-2\phi_g\right) + \sigma'_{xx}, \quad \text{(C.1)}$$

and

$$\mathcal{H}_l = \log\left(\phi-\phi_g\right) + 1 - \phi + \phi_g\left[\chi_{gl}\left(1-\phi+\phi_g\right) - \chi_{gs}\left(1-\phi\right)\right] + \chi_{gsl}\phi_g\left(1-\phi\right)\left[1-2\left(\phi-\phi_g\right)\right] + \sigma'_{xx}. \quad \text{(C.2)}$$

To derive $\mathcal{H}_{\alpha\beta}$, we then differentiate these expressions with respect to ϕ_g and ϕ, and evaluate them at $\phi = \phi'_0$ and $\phi_g = \phi_{g0}$. This gives

$$\mathcal{H}_{gg} = \frac{1}{\phi_{g0}} - \left(1+\phi'_0-2\phi_{g0}\right)\chi_{gl} - \left(1-\phi'_0\right)\chi_{gs} - \left(1-4\phi_{g0}+2\phi'_0\right)\left(1-\phi'_0\right)\chi_{gsl}, \quad \text{(C.3a)}$$

$$\mathcal{H}_{gf} = -1 + (1-\phi_{g0})\left[\chi_{gl} - \chi_{gs}\right] + (1 - 2\phi_0' + \phi_{g0})(1-2\phi_{g0})\chi_{gsl} + \frac{1}{2\mathcal{D}}(2+\varsigma)\left(\frac{1}{1-\phi_0'} + \frac{1}{1-\phi_0}\right), \quad \text{(C.3b)}$$

$$\mathcal{H}_{lg} = -\frac{1}{\phi_0' - \phi_{g0}} + (1 - \phi_0' + 2\phi_{g0})\,\chi_{gl} - (1-\phi_0')\,\chi_{gs} + (1 + 4\phi_{g0} - 2\phi_0')(1-\phi_0')\chi_{gsl}, \quad \text{(C.3c)}$$

$$\mathcal{H}_{lf} = \frac{1}{\phi_0' - \phi_{g0}} - 1 - \phi_{g0}\chi_{gl} + \phi_{g0}\chi_{gs} - \phi_{g0}\chi_{gsl} + \frac{1}{2\mathcal{D}}(2+\varsigma)\left(\frac{1}{1-\phi_0'} + \frac{1}{1-\phi_0}\right). \quad \text{(C.3d)}$$

To find explicit forms for $\mathcal{N}_{\alpha\beta}$, we collect the coefficients of fourth-order derivatives in Equations (3.4) to give

$$\mathcal{N}_{gg} = -(1-\phi_{g0})\,\Gamma_1 - (\phi_0' - \phi_{g0})\,\Gamma_2 - (2\phi_{g0} - \phi_0' - 1)\,\frac{\Gamma_3}{2}, \quad \text{(C.4a)}$$

$$\mathcal{N}_{gf} = -(\phi_{g0} - \phi_0')\,\Gamma_2 - (1-\phi_{g0})\,\frac{\Gamma_3}{2}, \quad \text{(C.4b)}$$

$$\mathcal{N}_{lg} = \phi_{g0}\Gamma_1 - (\phi_0' - \phi_{g0} - 1)\,\Gamma_2 - (2\phi_{g0} - \phi_0' + 1)\,\frac{\Gamma_3}{2}, \quad \text{(C.4c)}$$

$$\mathcal{N}_{lf} = -(\phi_{g0} - \phi_0' + 1)\,\Gamma_2 + \phi_{g0}\frac{\Gamma_3}{2}. \quad \text{(C.4d)}$$

The dispersion relation derived in §3.2 (Equation 3.5) is written compactly in terms of the functions $\zeta_1(k) = a_1 + a_2k^2$ and $\zeta_2(k) = b_1 + b_2k^2 + b_3k^4$, where

$$a_1 = \mathcal{U}_1\mathcal{H}_{gg} + \mathcal{U}_2\mathcal{H}_{lg} + \mathcal{U}_3\mathcal{H}_{gf} + \mathcal{U}_4\mathcal{H}_{lf}, \quad \text{(C.5a)}$$

$$a_2 = -\mathcal{U}_1\mathcal{N}_{gg} - \mathcal{U}_2\mathcal{N}_{lg} - \mathcal{U}_3\mathcal{N}_{gf} - \mathcal{U}_4\mathcal{N}_{lf}, \quad \text{(C.5b)}$$

and

$$b_1 = (\mathcal{U}_1\mathcal{U}_4 - \mathcal{U}_2\mathcal{U}_3)\,(\mathcal{H}_{gg}\mathcal{H}_{lf} - \mathcal{H}_{gf}\mathcal{H}_{lg}), \quad \text{(C.6a)}$$

$$b_2 = (\mathcal{U}_1\mathcal{U}_4 - \mathcal{U}_2\mathcal{U}_3)\,(\mathcal{H}_{lg}\mathcal{N}_{gf} + \mathcal{H}_{gf}\mathcal{N}_{lg} - \mathcal{H}_{gg}\mathcal{N}_{lf} - \mathcal{H}_{lf}\mathcal{N}_{gg})\,, \tag{C.6b}$$

$$b_3 = (\mathcal{U}_1\mathcal{U}_4 - \mathcal{U}_2\mathcal{U}_3)\,(\mathcal{N}_{gg}\mathcal{N}_{lf} - \mathcal{N}_{lg}\mathcal{N}_{gf})\,. \tag{C.6c}$$

We identify $\mathcal{U}_i$,

$$\mathcal{U}_1 = \mathcal{M}_r\,(1 - \phi_{g0})\,\phi_{g0}, \tag{C.7a}$$

$$\mathcal{U}_2 = -\,(\phi_0' - \phi_{g0})\,\phi_{g0}, \tag{C.7b}$$

$$\mathcal{U}_3 = \mathcal{M}_r\,(1 - \phi_0')\,\phi_{g0}, \tag{C.7c}$$

$$\mathcal{U}_4 = (1 - \phi_0')\,(\phi_0' - \phi_{g0})\,, \tag{C.7d}$$

as linearised mobility coefficients.

Appendix D

Experimental Calibration

D.1 Constitutive Response of Packing

We characterise the elastic response of the solid skeleton in the absence of gas cavities, by conducting uniaxial compression tests on a packing of liquid-saturated hydrogel beads. Compression is sufficiently slow such that poroelastic effects resulting from viscous drag can be neglected. The effective solid stress, $\sigma^{'}$, is measured at the piston by a micro-load cell as it advances from $\delta = 0$ to $\delta = \delta^{*}$. Figure D.1 shows the results of compression tests for a bead size $r_b = 0.95\,\mathrm{mm}$. We plot $\sigma^{'}$ as a function of both piston position, δ, and strain, $\mathcal{S}$. We calculate strain by assuming that at $\delta = 0$, the porous medium is relaxed such that $\phi_s = \phi_s^0$. Direct measurement of ϕ_s^0 is very challenging. Instead we assume that a relaxed packing is well approximated by a random close pack of spheres, for which $\phi_s^0 \sim 0.63$. Deviations from this value are likely to result in much smaller errors than those introduced by the measurement of stress by the load cell. As δ increases, the total amount of solid must be conserved, and so $\phi_s = \frac{\phi_s^0}{1-\delta}$. Strain is then calculated from Equation (4.15). We find that the stress-strain relation is well approximated by a linear fit (shown in black in Figure D.1). From the linear fit, we find a p-wave modulus of $M = 7.7\,\mathrm{kPa}$, which is in line with previous results [*e.g.*, MacMinn et al., 2015, Hewitt et al., 2015, 2016].

D.2 Measurement of Bead Size

To investigate the influence of varying the size of solid grains on our results, we first sieve an assortment of dry hydrogel beads into three different sets. Once beads have been fully swollen, we photograph a monolayer of each set of beads, and analyse the resulting images with a custom MATLAB code (courtesy of Christopher MacMinn). An outline of the procedure involved in this code is provided here. First, we use an intensity threshold to binarise each image such that individual beads are resolved. A circular profile is then fitted to each bead, and used to produce a histogram of the bead diameter distribution for each set of beads, as shown in Figure D.2. Each histogram represents data for at least 1500 beads. The mean and standard deviation of each distribution are then calculated. We find mean bead diameters given by:

$$\text{Set 1: } r_b = 0.40 \pm 0.07\,\text{mm},$$

$$\text{Set 2: } r_b = 0.48 \pm 0.06\,\text{mm},$$

$$\text{Set 3: } r_b = 0.63 \pm 0.08\,\text{mm}.$$

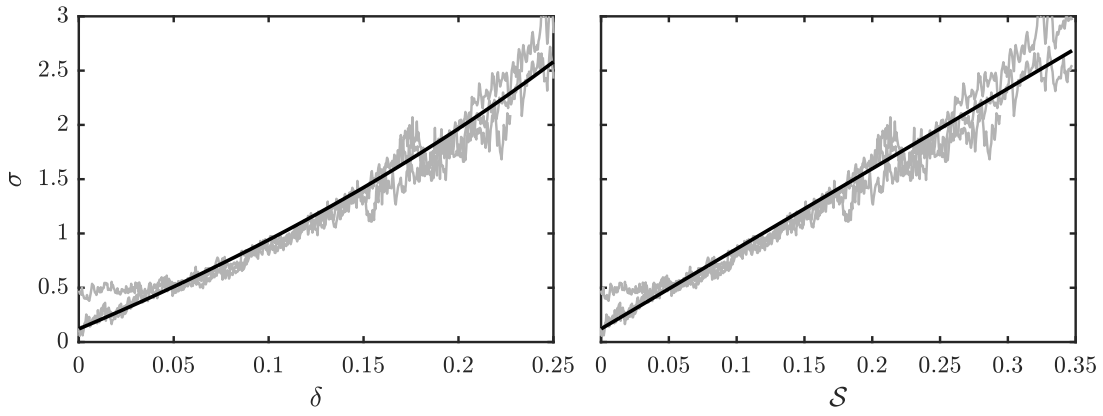

Figure D.1: Constitutive response of a liquid-saturated packing of hydrogel beads with $r_b = 0.95\,\mathrm{mm}$. Grey lines show $\sigma^{'}$ as a function of piston position, δ, and strain, $\mathcal{S}$, for three different tests. Black lines show a linear fit to the stress-strain data.

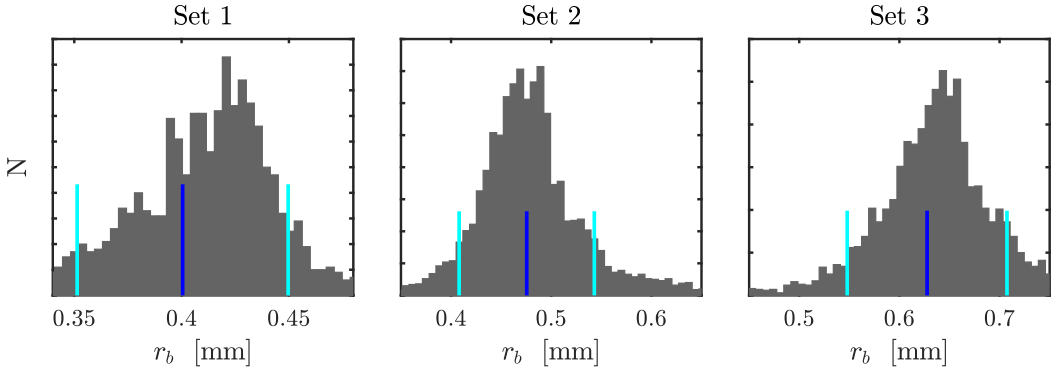

Figure D.2: Histograms showing the distribution of bead diameters for three different sets of hydrogel beads. Left to right, we find mean bead radii (blue lines) of $r_b = 0.40\,\mathrm{mm}$ (1733 beads), $r_b = 0.48\,\mathrm{mm}$ (5249 beads), and $r_b = 0.63\,\mathrm{mm}$ (3965 beads). Cyan lines show one standard deviation either side of the mean.

Appendix E

Image Analysis

We extract cavity size, Δ_g, and the size of the invaded region, $\mathcal{B}$, from experimental images via a custom interface tracking code in MATLAB. We outline the general procedure of this code here for a representative example. Videos are first imported as a series of greyscale image files and cropped appropriately. For each frame, pixel intensity is then averaged across the vertical dimension of the image to produce a one-dimensional intensity profile. Figure E shows the cropped image and the resulting intensity profile for an example frame. Typically, we find that the uninvaded region and the gas cavity have a higher mean intensity than the invaded region, in which light is scattered by the many gas-liquid menisci. We can thus detect the position of the piston, gas invasion front, and cavity by tracking when

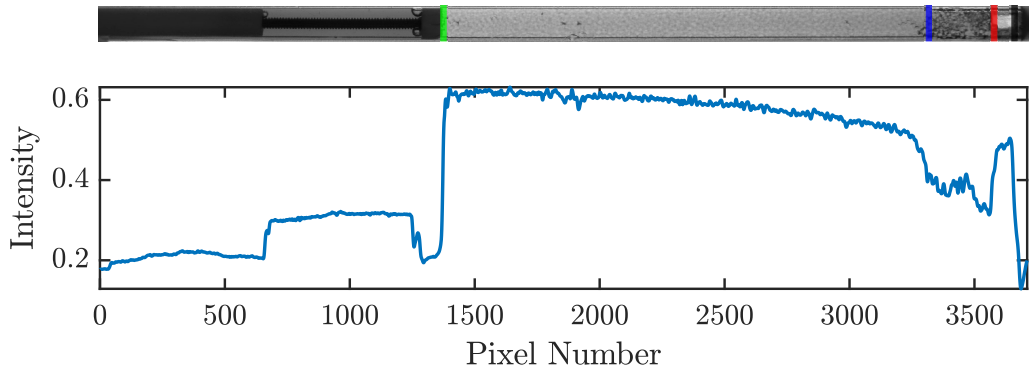

Figure E.1: An example experimental image (top), and its mean intensity profile (bottom). Green, blue, red and black lines show detected interfaces corresponding to the positions of the piston, gas invasion front, cavity and tube end, respectively.

the mean intensity passes through certain threshold values. The specific threshold values used vary slightly between different experiments, owing to variations in lighting conditions, but are typically around 0.5. Repeating this procedure for each frame allows us to then plot Δ_g and $\mathcal{B}$ as functions of δ.

Appendix F

Extension of Toy Model

Motivated by our experimental results, we now develop an extension of the simple toy model presented in §4.3.1. We incorporate compressibility of the gas phase, deformation-dependent entry pressure and friction with the domain walls. We assume that there exists separate 'uninvaded' and 'invaded' regions of the porous medium, separated by a gas–liquid interface, which have non-dimensional size $\mathcal{A}$ and $\mathcal{B}$, respectively. We assume that invaded region is relaxed and completely gas-saturated. The size of the gas cavity is denoted Δ_g. We note that, as before, $\delta + \mathcal{A} + \mathcal{B} + \Delta_g = 1$.

We assume that the pressure in the gas phase obeys Boyle's law, such that $p_g V_g$ is fixed, where V_g is the total volume of gas. Assuming that liquid pressure is fixed at atmospheric pressure, $p_l = p_{\text{atm}}$, and that $p_c = 0$ when $\delta = 0$, conservation of mass for gas gives

$$\Delta_g + \mathcal{B}\phi_0 = \frac{p_{\text{atm}}\Delta_g^0}{p_g}. \tag{F.1}$$

We then use the definition $p_c = p_g - p_l$ to write

$$\Delta_g + \mathcal{B}\phi_0 = \frac{\Delta_g^0}{1 + \mathcal{C}p_c/p_c^{e,0}}, \tag{F.2}$$

where $\mathcal{C} = \frac{p_c^{e,0}}{p_{\text{atm}}}$ is a dimensionless 'compressibility' and $p_c^{e,0} = \frac{2\gamma_{gl}\cos\vartheta_c}{r_p^0}$ is the capillary entry pressure at $\delta = 0$, with r_p^0 the typical radius of a pore throat at

$\delta = 0$. Conservation of solid is unchanged, such that

$$(1 - \phi^u)\mathcal{A} + (1 - \phi_0)\mathcal{B} = (1 - \phi_0)\mathcal{A}_0. \tag{F.3}$$

The elastic stress in the uninvaded region is given by

$$\sigma^u = M\mathcal{S} = M\frac{\phi^u - \phi_0}{1 - \phi_0}, \tag{F.4}$$

where $\mathcal{S}$ is the true strain. Note that σ^u is negative in compression.

Accounting for friction between the beads and the walls, force balance at the gas–liquid interface is given by

$$\sigma^u = \frac{p_c}{\mathcal{A}\mathcal{J}}\left[1 - \exp(\mathcal{J}\mathcal{A})\right], \tag{F.5}$$

where $\mathcal{J}$ is a dimensionless parameter that characterises the strength of friction. A detailed derivation of Equation (F.5), following recent models of frictional flow in confined geometries [Knudsen et al., 2008, Marks et al., 2015, Morrow et al., 2023b], is provided in §F.1 below. Prior to pore invasion, $\mathcal{B} = 0$, and p_c is determined by Equation (F.5). Once p_c reaches the capillary entry pressure, p_c^e, $\mathcal{B}$ is free to vary, and we additionally impose that $p_c = p_c^e$. We allow p_c^e to depend on deformation by assuming r_p to be a linear function of strain,

$$r_p = r_p^0\left(1 + \tau\mathcal{S}\right), \tag{F.6}$$

where τ is a dimensionless constant. The capillary entry pressure is then given by

$$p_c^e = \frac{2\gamma_{gl}\cos\vartheta_c}{r_p}. \tag{F.7}$$

Equations (F.2)–(F.7) give a complete system that can be solved by numerical root-finding for a given value of δ. In the limit $\mathcal{C},\ \mathcal{J},\ \tau \to 0$, we recover the simple toy model derived in §4.3.1.

F.1 Frictional Stress

To characterise the effect of friction, we treat the uninvaded region as a liquid-saturated porous medium within a cylindrical tube and allow variables to depend on both the axial and radial coordinates, x and ϱ, respectively. We follow the approaches of Marks et al. [2015] and Morrow et al. [2023b] to derive a relevant friction law. By Terzaghi's principle, the total stress in the uninvaded region is given by

$$\mathbb{T} = \boldsymbol{\sigma}^{'} - p_l \mathbb{I}, \tag{F.8}$$

where $\boldsymbol{\sigma}^{'}$ is the effective stress and p_l is the liquid pressure. Conservation of momentum requires that

$$\nabla \cdot \mathbb{T} = 0. \tag{F.9}$$

In the axial direction, this gives

$$\frac{\partial \sigma^{'}_{xx}}{\partial x} - \frac{\partial p_l}{\partial x} + \frac{1}{\varrho}\frac{\partial \varrho \sigma^{'}_{x\varrho}}{\partial \varrho} = 0. \tag{F.10}$$

Neglecting variations in p_l in the x-direction (as we are considering a quasi-static process), we can then integrate Equation (F.10) in the ϱ direction from $\varrho = 0$ to $\varrho = r_t$, where r_t is the radius of the tube. We assume that $\frac{\partial \sigma^{'}_{xx}}{\partial x}$ is constant along the ϱ-direction, such that

$$r_t^2 \frac{\partial \sigma^{'}_{xx}}{\partial x} = -\left[\varrho \sigma^{'}_{x\varrho}\right]_0^{r_t}. \tag{F.11}$$

By symmetry, we set $\sigma^{'}_{x\varrho} = 0$ at $\varrho = 0$. To evaluate $\sigma^{'}_{x\varrho}$ at $\varrho = r_t$, we use Coulomb friction,

$$\sigma^{'}_{x\varrho}|_{\varrho = r_t} = C_F \sigma^{'}_{\varrho\varrho}, \tag{F.12}$$

where C_F is the coefficient of friction, and $\sigma^{'}_{\varrho\varrho}$ is the effective normal stress in the radial direction. Due to the Janssen effect [Janssen, 1895],

$$\sigma^{'}_{\varrho\varrho} = K_J \sigma^{'}_{xx}, \tag{F.13}$$

where K_J is the Janssen coefficient. Substituting into Equation (F.11), we then have

$$\frac{\partial \sigma^{'}_{xx}}{\partial x} = -\frac{C_F K_J}{r_t} \sigma^{'}_{xx}. \tag{F.14}$$

We note that we have ignored friction in the invaded region, having taken that region to be relaxed.

Denoting $\mathcal{J} = \frac{C_F K_J}{r_t}$ for conciseness, we then solve Equation (F.14) to find $\sigma^{'}_{xx}(x)$. We integrate from $x = x$ to $x = \mathcal{A}$ (along the length of the uninvaded region), applying the boundary condition $\sigma^{'}_{xx} = -p_c$ at $x = \mathcal{A}$. This boundary condition results from enforcing stress balance at the interface between the invaded and uninvaded regions. Recall that $\sigma^{'}_{xx}$ is negative when in compression. Integrating Equation (F.14) gives

$$\sigma^{'}_{xx} = -p_c \exp\left[\mathcal{J}\left(\mathcal{A} - x\right)\right]. \tag{F.15}$$

To connect this result with the rest of the toy model, we define σ^u as the average effective stress in the uninvaded region,

$$\sigma^u = \frac{1}{\mathcal{A}} \int_0^{\mathcal{A}} \sigma^{'}_{xx} \mathrm{d}x. \tag{F.16}$$

The effective stress is linked to the porosity in the uninvaded region by Equation (F.4), where now

$$\phi^u = \frac{1}{\mathcal{A}} \int_0^{\mathcal{A}} \phi \mathrm{d}x. \tag{F.17}$$

To complete the model, we integrate Equation (F.15) to link p_c to σ^u. The result of this integration is

$$\sigma^u = \frac{p_c}{\mathcal{A}\mathcal{J}} \left[1 - \exp(\mathcal{J}\mathcal{A})\right]. \tag{F.18}$$

Equation (F.18) is then used with Equation (F.4) to determine ϕ^u. Note that the x-dependence of the effective stress is not important for determining p_c. To calculate the confining stress from p_c, Equation (F.15) can be evaluated at the piston, $x = 0$. In the limit $\mathcal{J} \to 0$ (no friction), we reproduce Equation (4.14) from the simple toy model, with $\sigma^u = -p_c$, and ϕ and σ'_{xx} uniform along x.

References

S. M. Allen and J. W. Cahn. A microscopic theory for antiphase boundary motion and its application to antiphase domain coarsening. *Acta Metallurgica*, 27(6): 1085–1095, 1979.

D. M. Anderson, G. B. McFadden, and A. A. Wheeler. Diffuse-interface methods in fluid mechanics. *Annual Review of Fluid Mechanics*, 30(1):139–165, 1998.

L. C. Auton and C. W. MacMinn. From arteries to boreholes: steady-state response of a poroelastic cylinder to fluid injection. *Proceedings of the Royal Society A: Mathematical, Physical and Engineering Sciences*, 473(2201):20160753, 2017.

L. C. Auton and C. W. MacMinn. From arteries to boreholes: transient response of a poroelastic cylinder to fluid injection. *Proceedings of the Royal Society A: Mathematical, Physical and Engineering Sciences*, 474(2216):20180284, 2018.

L. C. Auton and C. W. MacMinn. Large poroelasto-plastic deformations due to radially outward fluid injection. *Journal of the Mechanics and Physics of Solids*, 132:103690, 2019.

M. D. Bartlett and R. W. Style. Introduction to liquid composites. *Soft Matter*, 16:5799–5800, 2020.

T. Bertrand, J. Peixinho, S. Mukhopadhyay, and C. W. MacMinn. Dynamics of swelling and drying in a spherical gel. *Physical Review Applied*, 6(6):64010, 2016.

M. A. Biot. General theory of three-dimensional consolidation. *Journal of Applied Physics*, 12(2):155–164, 1941.

M. A. Biot. Theory of propagation of elastic waves in a fluid-saturated porous solid. I. Low-frequency range. *The Journal of the Acoustical Society of America*, 28 (2):168–178, 1956.

M. A. Biot. Mechanics of deformation and acoustic propagation in porous media. *Journal of Applied Physics*, 33(4):1482–1498, 1962.

M. A. Biot. Theory of finite deformations of porous solids. *Indiana University Mathematics Journal*, 21(7):597–620, 1972.

M. J. Blunt. *Multiphase Flow in Permeable Media: A Pore-Scale Perspective*. Cambridge University Press, 2017.

B. P. Boudreau. The physics of bubbles in surficial, soft, cohesive sediments. *Marine and Petroleum Geology*, 38(1):1–18, 2012.

B. P. Boudreau, C. Algar, B. Johnson, A. Reed, Y. Furukawa, K. Dorgan, P. Jumars, A. Grader, and B. Gardiner. Bubble growth and rise in soft sediments. *Geology*, 33:517–520, 2005.

B. Bourdin, G. A. Francfort, and J.-J. Marigo. The variational approach to fracture. *J Elasticity*, 91:5–148, 2008.

S. Buckley and M. Leverett. Mechanism of fluid displacement in sands. *Transactions of the AIME*, 146(01):107–116, 1942.

G. Caginalp. Stefan and Hele-Shaw type models as asymptotic limits of the phase-field equations. *Physical Review A*, 39(11):5887–5896, 1989.

J. W. Cahn. Free energy of a nonuniform system. II. Thermodynamic basis. *The Journal of Chemical Physics*, 30(5):1121–1124, 1959.

J. W. Cahn. On spinodal decomposition. *Acta Metallurgica*, 9(9):795–801, 1961.

J. W. Cahn and J. E. Hilliard. Free energy of a nonuniform system. I. Interfacial free energy. *The Journal of Chemical Physics*, 28(2):258–267, 1958.

J. W. Cahn and J. E. Hilliard. Free energy of a nonuniform system. III. Nucleation in a two-component incompressible fluid. *The Journal of Chemical Physics*, 31 (3):688–699, 1959.

F. J. Carrillo and I. C. Bourg. A Darcy-Brinkman-Biot approach to modeling the hydrology and mechanics of porous media containing macropores and deformable microporous regions. *Water Resources Research*, 55(10):8096–8121, 2019.

F. J. Carrillo and I. C. Bourg. Capillary and viscous fracturing during drainage in porous media. *Physical Review E*, 103:063106, 2021a.

F. J. Carrillo and I. C. Bourg. Modeling multiphase flow within and around deformable porous materials: a Darcy-Brinkman-Biot approach. *Water Resources Research*, 57(e2020WR028734):1–27, 2021b.

G. L. Celora, M. G. Hennessy, A. Münch, B. Wagner, and S. L. Waters. A kinetic model of a polyelectrolyte gel undergoing phase separation. *Journal of the Mechanics and Physics of Solids*, 160:104771, 2022.

G. L. Celora, M. G. Hennessy, A. Muench, B. Wagner, and S. Waters. The dynamics of a collapsing polyelectrolyte gel. *SIAM Journal on Applied Mathematics*, 83(3):1146–1171, 2023.

X. Chen and L. Slater. Gas bubble transport and emissions for shallow peat from a northern peatland: The role of pressure changes and peat structure. *Water Resources Research*, 51(1):151–168, 2015.

O. Coussy. *Poromechanics*. Wiley, 2004.

N. L. Cuccia, S. Pothineni, B. Wu, J. M. Harper, and J. C. Burton. Pore-size dependence and slow relaxation of hydrogel friction on smooth surfaces. *Proceedings of the National Academy of Sciences*, 117(21):11247–11256, 2020.

L. Cueto-Felgueroso and R. Juanes. Nonlocal interface dynamics and pattern formation in gravity-driven unsaturated flow through porous media. *Physical Review Letters*, 101:24, 2008.

L. Cueto-Felgueroso and R. Juanes. A phase field model of unsaturated flow. *Water Resources Research*, 45(10), 2009.

L. Cueto-Felgueroso and R. Juanes. A phase-field model of two-phase Hele-Shaw flow. *Journal of Fluid Mechanics*, 758:522–552, 2014.

C. Cuttle and C. W. MacMinn. Dynamics of compression-driven gas-liquid displacement in a capillary tube. *Physical Review Letters*, 130:114001, 2023.

C. Cuttle, L. C. Morrow, and C. W. MacMinn. Compression-driven viscous fingering in a radial Hele-Shaw cell. *Physical Review Fluids*, 8:113904, 2023.

H. Dai, S. Xu, Z. Xu, N. Zhao, C.-X. Zhu, and C. Zhu. A phase field model for compressible immiscible fluids with a new equation of state. *International Journal of Multiphase Flow*, 149:103937, 2022.

H. Darcy. *Les fontaines publiques de la ville de Dijon.* Hachette Livre, 1856.

P. S. de Laplace. *Traité De Mécanique Céleste: Supplément au dixième livre du traité de méchanique céleste sur l'action capillaire*, volume 6. Duprat, 1808.

J. A. Dijksman and T. Mullin. Creep control in soft particle packings. *Physical Review Letters*, 128:238002, 2022.

M. Doi. *Soft Matter Physics.* Oxford University Press, 2013.

G. Dumazer, B. B. Sandnes, M. Ayaz, K. J. Måløy, E. G. Flekkøy, K. J. Måløy, and E. G. Flekkøy. Frictional fluid dynamics and plug formation in multiphase millifluidic flow. *Physical Review Letters*, 117(2):28002, 2016.

K. R. Elder, M. Grant, N. Provatas, and J. M. Kosterlitz. Sharp interface limits of phase-field models. *Physical Review E*, 64(2):21604, 2001.

C. Fernández-Rico, S. Schreiber, H. Oudich, C. Lorenz, A. Sicher, T. Sai, V. Bauernfeind, S. Heyden, P. Carrara, L. D. Lorenzis, et al. Elastic microphase separation produces robust bicontinuous materials. *Nature Materials*, pages 1–7, 2023.

C. Fernández-Rico, T. Sai, A. Sicher, R. W. Style, and E. R. Dufresne. Putting the squeeze on phase separation. *JACS Au*, 2(1):66–73, 2022.

M. Fiori, S. Pramanik, and C. W. MacMinn. Flow and deformation due to periodic loading in a soft porous material. *Journal of Fluid Mechanics*, 974:A2, 2023.

P. J. Flory and J. Rehner. Statistical mechanics of cross-linked polymer networks I. Rubberlike elasticity. *The Journal of Chemical Physics*, 11(11):512–520, 1943.

E. Fried and M. E. Gurtin. Continuum theory of thermally induced phase transitions based on an order parameter. *Physica D: Nonlinear Phenomena*, 68: 326–343, 1993.

E. Fried and M. E. Gurtin. Dynamic solid-solid transitions with phase characterized by an order parameter. *Physica D: Nonlinear Phenomena*, 72:287–308, 1994.

X. Fu, L. Cueto-Felgueroso, and R. Juanes. Thermodynamic coarsening arrested by viscous fingering in partially miscible binary mixtures. *Physical Review E*, 94(3):33111, 2016.

X. Fu, L. Cueto-Felgueroso, and R. Juanes. Viscous fingering with partially miscible fluids. *Physical Review Fluids*, 2(10):104001, 2017.

X. Fu, L. Cueto-Felgueroso, and R. Juanes. Nonequilibrium thermodynamics of hydrate growth on a gas-liquid interface. *Physical Review Letters*, 120:144501, 2018.

X. Fu, J. Jimenez-Martinez, T. P. Nguyen, J. W. Carey, H. Viswanathan, L. Cueto-Felgueroso, and R. Juanes. Crustal fingering facilitates free-gas methane migration through the hydrate stability zone. *Proceedings of the National Academy of Sciences*, 117(50):31660–31664, 2020.

J. E. Gardner, F. B. Wadsworth, T. L. Carley, E. W. Llewellin, H. Kusumaatmaja, and D. Sahagian. Bubble formation in magma. *Annual Review of Earth and Planetary Sciences*, 51(1):131–154, 2023.

R. Gonzalez and G. Sills. Consolidation of naturally gassy soft soil. *Geotechnique*, 51:629–639, 2001.

A. A. Griffith. The phenomena of rupture and flow in solids. *Philosophical Transactions of the Royal Society of London. Series A*, 221:163–198, 1921.

M. E. Gurtin. On a nonequilibrium thermodynamics of capillarity and phase. *Quarterly of Applied Mathematics*, XLVII(1):129–145, 1989.

M. E. Gurtin. Generalized Ginzburg-Landau and Cahn-Hilliard equations based on a microforce balance. *Physica D: Nonlinear Phenomena*, 92(3):178–192, 1996.

M. E. Gurtin, D. Polignone, J. Vinals, and J. Viñals. Two-phase binary fluids and immiscible fluids described by an order parameter. *Mathematical Models and Methods in Applied Sciences*, 6(6):815–831, 1995.

A. Guével, Y. Meng, C. Peco, R. Juanes, and J. E. Dolbow. A Darcy–Cahn–Hilliard model of multiphase fluid-driven fracture. *Journal of the Mechanics and Physics of Solids*, 181:105427, 2023.

S. R. Heidemann and D. Wirtz. Towards a regional approach to cell mechanics. *Trends in Cell Biology*, 14(4):160–166, 2004.

M. G. Hennessy, A. Münch, and B. Wagner. Phase separation in swelling and deswelling hydrogels with a free boundary. *Physical Review E*, 101(3):32501, 2020.

D. R. Hewitt, J. A. Neufeld, and N. J. Balmforth. Shallow, gravity-driven flow in a poro-elastic layer. *Journal of Fluid Mechanics*, 778:335–360, 2015.

D. R. Hewitt, J. S. Nijjer, M. G. Worster, and J. A. Neufeld. Flow-induced compaction of a deformable porous medium. *Physical Review E*, 93:023116, 2016.

G. M. Homsy. Viscous fingering in porous media. *Annual Review of Fluid Mechanics*, 19(1):271–311, 1987.

W. Hong and X. Wang. A phase-field model for systems with coupled large deformation and mass transport. *Journal of the Mechanics and Physics of Solids*, 61 (6):1281–1294, 2013.

Y. Hong, L. Wang, C. W. Ng, and B. Yang. Effect of initial pore pressure on undrained shear behaviour of fine-grained gassy soil. *Canadian Geotechnical Journal*, 54(11):1592–1600, 2017.

G. T. Houlsby and A. M. Puzrin. *Principles of Hyperplasticity: An Approach to Plasticity Theory Based on Thermodynamic Principles*. Springer, 2010.

A. A. Hyman, C. A. Weber, and F. Jülicher. Liquid-liquid phase separation in biology. *Annual Review of Cell and Developmental Biology*, 30(1):39–58, 2014.

T. Idema, J. M. Van Leeuwen, and C. Storm. Phase coexistence and line tension in ternary lipid systems. *Physical Review E*, 80(4):1–9, 2009.

H. A. Janssen. Versuche über Getreidedruck in Silozellen. *Z. Ver. Dt. Ing.*, 39: 1045–1049, 1895.

K. Jensen and Y. Forterre. *Soft Matter in Plants: From Biophysics to Biomimetics*. Royal Society of Chemistry, 2022.

R. Juanes, Y. Meng, and B. K. Primkulov. Multiphase flow and granular mechanics. *Physical Review Fluids*, 5(11):110516, 2020.

S. Kam, P. Gauglitz, and W. Rossen. Effective compressibility of a bubbly slurry: II. Fitting numerical results to field data and implications. *Journal of Colloid and Interface Science*, 241(1):260–268, 2001.

P. Kaminski, M. Urlaub, J. Grabe, and C. Berndt. Geomechanical behaviour of gassy soils and implications for submarine slope stability - a literature analysis. *Geological Society, London, Special Publications*, 500:SP500–2019, 2019.

J. Kim and J. Lowengrub. Phase field modeling and simulation of three-phase flows. *Interfaces and Free Boundaries*, 7(4):435–466, 2005.

J. Y. Kim, Z. Liu, B. M. Weon, T. Cohen, C.-Y. Hui, E. R. Dufresne, and R. W. Style. Extreme cavity expansion in soft solids: damage without fracture. *Science Advances*, 6:13, 2020.

H. A. Knudsen, B. Sandnes, E. G. Flekkøy, and K. J. Måløy. Granular labyrinth structures in confined geometries. *Physical Review E*, 77(2):021301, 2008.

M. Kothari and T. Cohen. Effect of elasticity on phase separation in heterogeneous systems. *Journal of the Mechanics and Physics of Solids*, 145:104153, 2020.

M. Kothari and T. Cohen. The crucial role of elasticity in regulating liquid–liquid phase separation in cells. *Biomechanics and Modeling in Mechanobiology*, 22(2): 645–654, 2023.

F. C. Larché and J. W. Cahn. Phase changes in a thin plate with non-local self-stress effects. *Acta Metallurgica et Materialia*, 40(5):947–955, 1992.

S. Lee, J. Lee, R. L. Mestre, F. Xu, and C. W. MacMinn. Migration, trapping, and venting of gas in a soft granular material. *Physical Review Fluids*, 5(8): 84307, 2020.

J. X. Liu, M. P. Haataja, A. Košmrlj, S. S. Datta, C. B. Arnold, and R. D. Priestley. Liquid–liquid phase separation within fibrillar networks. *Nature Communications*, 14(1):6085, 2023.

T. Liu, X. Yang, and Y. Zhang. A review of gassy sediments: mechanical property, disaster simulation and in-situ test. *Frontiers in Earth Science*, 10, 2022.

C. W. MacMinn, E. R. Dufresne, and J. S. Wettlaufer. Fluid-driven deformation of a soft granular material. *Physical Review X*, 5(1):11020, 2015.

C. W. MacMinn, E. R. Dufresne, and J. S. Wettlaufer. Large deformations of a soft porous material. *Physical Review Applied*, 5(4):44020, 2016.

B. Marks, B. Sandnes, G. Dumazer, J. A. Eriksen, and K. J. Måløy. Compaction of granular material inside confined geometries. *Frontiers in Physics*, 3, 2015.

D. McGinnis, J. Greinert, Y. Artemov, S. Beaubien, and A. Wuest. Fate of rising methane bubbles in stratified waters: how much methane reaches the atmosphere? *Journal of Geophysical Research*, 111, 09 2006.

Y. Meng, W. Li, and R. Juanes. Crossover from viscous fingering to fracturing in cohesive wet granular media: a photoporomechanics study. *Soft Matter*, 19: 7136–7148, 2023.

C. R. Meyer and I. J. Hewitt. A continuum model for meltwater flow through compacting snow. *The Cryosphere*, 11(6):2799–2813, 2017.

C. Miehe, M. Hofacker, and F. Welschinger. A phase field model for rate-independent crack propagation: robust algorithmic implementation based on operator splits. *Computer Methods in Applied Mechanics and Engineering*, 199 (45):2765–2778, 2010a.

C. Miehe, F. Welschinger, and M. Hofacker. Thermodynamically consistent phase-field models of fracture: variational principles and multi-field FE implementations. *International Journal for Numerical Methods in Engineering*, 83(10): 1273–1311, 2010b.

L. C. Morrow, C. Cuttle, and C. W. MacMinn. Gas Compression Systematically Delays the Onset of Viscous Fingering. *Physical Review Letters*, 131:224002, 2023a.

L. C. Morrow, M. G. Hennessy, D. R. Hewitt, C. W. MacMinn, M. L. Morgan, O. W. Paulin, and B. Sandnes. A continuum model for the bulldozing of a dense granular material in a confined geometry. In prep, 2023b.

R. Mueller and A. Doostmohammadi. Phase field models of active matter, 2021.

S. Mukhopadhyay and J. Peixinho. Packings of deformable spheres. *Physical Review E*, 84:011302, 2011.

A. Nasto, M. Regli, P.-T. Brun, J. Alvarado, C. Clanet, and A. E. Hosoi. Air entrainment in hairy surfaces. *Physical Review Fluids*, 1:033905, 2016.

P. Nuske, B. Faigle, R. Helmig, J. Niessner, and I. Neuweiler. Modeling gas-water processes in fractures with fracture flow properties obtained through upscaling. *Water Resources Research*, 46(9), 2010.

J. T. Oden, A. Hawkins, and S. Prudhomme. General diffuse-interface theories and an approach to predictive tumour growth modeling. *Mathematical Models and Methods in Applied Sciences*, 20(03):477–517, 2010.

S. H. Ommi, G. Sciarra, and P. Kotronis. A phase field model for partially saturated geomaterials describing fluid–fluid displacements. Part I: the model and one-dimensional analysis. *Advances in Water Resources*, 164:104170, 2022a.

S. H. Ommi, G. Sciarra, and P. Kotronis. A phase field model for partially saturated geomaterials describing fluid–fluid displacements, Part II: stability analysis and two-dimensional simulations. *Advances in Water Resources*, 164:104201, 2022b.

A. Onuki and S. Puri. Spinodal decomposition in gels. *Physical Review E*, 59: R1331–R1334, 1999.

W. Ostwald. Studien über die Bildung und Umwandlung fester Körper. *Zeit. fur Physik Chemie*, 22:289, 1897.

G. Ovarlez and E. Clément. Elastic medium confined in a column versus the Janssen experiment. *The European Physical Journal E*, 16:421–438, 2005.

D. T. Paterson, T. S. Eaves, D. R. Hewitt, N. J. Balmforth, and D. M. Martinez. One-dimensional compression of a saturated elastoviscoplastic medium. *Physical Review Fluids*, 7:054303, 2022.

O. W. Paulin, L. C. Morrow, M. G. Hennessy, and C. W. MacMinn. Fluid–fluid phase separation in a soft porous medium. *Journal of the Mechanics and Physics of Solids*, 164:104892, 2022.

N. Provatas and K. R. Elder. *Phase-Field Methods in Materials Science and Engineering*. John Wiley and Sons, Ltd, 2010.

R. Pugh, C. Hamlett, and D. Fairhurst. A short overview of bubbles in foods and chocolate. *Advances in Colloid and Interface Science*, 314:102835, 2023.

Y. Qiang, C. Luo, and D. Zwicker. Theory of elastic microphase separation, 2023.

P. Ronceray, S. Mao, A. Kosmrlj, and M. P. Haataja. Liquid demixing in elastic networks: cavitation, permeation, or size selection? *Europhysics Letters*, 137 (6):67001, 2022.

K. A. Rosowski, T. Sai, E. Vidal-Henriquez, D. Zwicker, R. W. Style, and E. R. Dufresne. Elastic ripening and inhibition of liquid–liquid phase separation. *Nature Physics*, 16:422–425, 2020a.

K. A. Rosowski, E. Vidal-Henriquez, D. Zwicker, R. W. Style, and E. R. Dufresne. Elastic stresses reverse Ostwald ripening. *Soft Matter*, 16:5892–5897, 2020b.

B. Sandnes, E. G. Flekkøy, H. A. Knudsen, K. J. Måløy, and H. See. Patterns and flow in frictional fluid dynamics. *Nature Communications*, 2:288, 2011.

D. Santillán, R. Juanes, and L. Cueto-Felgueroso. Phase field model of hydraulic fracturing in poroelastic media: fracture propagation, arrest, and branching under fluid injection and extraction. *Journal of Geophysical Research: Solid Earth*, 123(3):2127–2155, 2018.

B. P. Scandella, C. Varadharajan, H. F. Hemond, C. Ruppel, and R. Juanes. A conduit dilation model of methane venting from lake sediments. *Geophysical Research Letters*, 38(6), 2011.

L. Schreyer and Z. Hilliard. Derivation of generalized Cahn-Hilliard equation for two-phase flow in porous media using hybrid mixture theory. *Advances in Water Resources*, 149:103839, 2021.

G. Sciarra. Phase field modeling of partially saturated deformable porous media. *Journal of the Mechanics and Physics of Solids*, 94:230–256, 2016.

G. Sills and S. Wheeler. The significance of gas for offshore operations. *Continental Shelf Research*, 12(10):1239–1250, 1992.

G. C. Sills, S. J. Wheeler, S. D. Thomas, and T. N. Gardner. Behaviour of offshore soils containing gas bubbles. *Géotechnique*, 41(2):227–241, 1991.

A. Skarke, C. Ruppel, M. Kodis, D. Brothers, and E. Lobecker. Widespread methane leakage from the sea floor on the northern US Atlantic Margin. *Nature Geosci*, 7:657–661, 2014.

R. W. Style, R. Boltyanskiy, B. Allen, K. E. Jensen, H. P. Foote, J. S. Wettlaufer, and E. R. Dufresne. Stiffening solids with liquid inclusions. *Nature Physics*, 11 (1):82–87, 2015.

R. W. Style, T. Sai, N. Fanelli, M. Ijavi, K. Smith-Mannschott, Q. Xu, L. A. Wilen, and E. R. Dufresne. Liquid-liquid phase separation in an elastic network. *Physical Review X*, 8(1):11028, 2018.

J. Suckale, T. Keller, K. V. Cashman, and P.-O. Persson. Flow-to-fracture transition in a volcanic mush plug may govern normal eruptions at Stromboli. *Geophysical Research Letters*, 43(23):12,071–12,081, 2016.

X. Sun and M. J. Ward. Dynamics and coarsening of interfaces for the viscous Cahn—Hilliard equation in one spatial dimension. *Studies in Applied Mathematics*, 105(3):203–234, 2000.

B. R. Sutherland and N. J. Balmforth. Damping of surface waves by floating particles. *Physical Review Fluids*, 4:014804, 2019.

S. Tang, G. Zhang, T. F. Guo, X. Guo, and W. K. Liu. Phase field modeling of fracture in nonlinearly elastic solids via energy decomposition. *Computer Methods in Applied Mechanics and Engineering*, 347:477–494, 2019.

M. Terzariol, N. Sultan, R. Apprioual, and S. Garziglia. Pore habit of gas in gassy sediments. *Journal of Geophysical Research: Solid Earth*, 126(5): e2020JB021511, 2021.

E. Vidal-Henriquez and D. Zwicker. Theory of droplet ripening in stiffness gradients. *Soft Matter*, 16:5898–5905, 2020.

E. Vidal-Henriquez and D. Zwicker. Cavitation controls droplet sizes in elastic media. *Proceedings of the National Academy of Sciences*, 118(40):40, 2021.

V. Vilarrasa, D. Bolster, M. Dentz, S. Olivella, and J. Carrera. Effects of CO2 compressibility on CO2 storage in deep saline aquifers. *Transport in Porous Media*, 85(2):619–639, 2010.

K. von Terzaghi. The shearing resistance of saturated soil and the angle between the planes of shear. *Proceedings of the International Conference on Soil Mechanics and Foundation Engineering*, 1:54–56, 1936.

P. W. Voorhees. Ostwald ripening of two-phase mixtures. *Annual Review of Materials Science*, 22(1):197–215, 1992.

C. Walsh. Validation and development of extravascular bubble models for decompression sickness using collagen hydrogel, 2017.

H. F. Wang. *Theory of Linear Poroelasticity with Applications to Geomechanics and Hydrogeology*. Princeton University Press, 2001.

X. Wei, J. Zhou, Y. Wang, and F. Meng. Modeling elastically mediated liquid-liquid phase separation. *Physical Review Letters*, 125(26):268001, 2020.

S. J. Wheeler. The stress-strain behaviour of soils containing gas bubbles, 1986.

S. J. Wheeler. A conceptual model for soils containing large gas bubbles. *Géotechnique*, 38(3):389–397, 1988a.

S. J. Wheeler. The undrained shear strength of soils containing large gas bubbles. *Géotechnique*, 38(3):399–413, 1988b.

S. J. Wheeler. Movement of large gas bubbles in unsaturated fine-grained sediments. *Marine Geotechnology*, 9(2):113–129, 1990.

T. Young. An essay on the cohesion of fluids. *Philosophical Transactions of the Royal Society of London*, 95:65–87, 1805.

Y. Zhang, M. A. Etzold, and A. Lefauve. Growth of gas-filled penny-shaped cracks in decompressed hydrogels. *Soft Matter*, 17(4):815–825, 2021.

J. Zhou, G. Huang, M. Li, and A. K. Soh. Stress evolution in a phase-separating polymeric gel. *Modelling and Simulation in Materials Science and Engineering*, 18(2):025002, 2010.